Modeling Microdomain Evolution on Giant Unilamellar Vesicles using a Phase-Field Approach

by

Anand Embar

Department of Civil and Environmental Engineering
Duke University

Date: _____

Approved:

_____
John Dolbow, Supervisor

_____
Thomas Witelski

_____
Wilkins Aquino

_____
Guglielmo Scovazzi

_____
Xuanhe Zhao

Dissertation submitted in partial fulfillment of the requirements for the degree of Doctor of Philosophy in the Department of Civil and Environmental Engineering in the Graduate School of Duke University
2013

Abstract

Modeling Microdomain Evolution on Giant Unilamellar Vesicles using a Phase-Field Approach

by

Anand Embar

Department of Civil and Environmental Engineering
Duke University

Date: _____

Approved:

_____
John Dolbow, Supervisor

_____
Thomas Witelski

_____
Wilkins Aquino

_____
Guglielmo Scovazzi

_____
Xuanhe Zhao

An abstract of a dissertation submitted in partial fulfillment of the requirements for the degree of Doctor of Philosophy in the Department of Civil and Environmental Engineering
in the Graduate School of Duke University
2013

Copyright © 2013 by Anand Embar
All rights reserved except the rights granted by the
Creative Commons Attribution-Noncommercial Licence

Abstract

The surface of cell membranes can display a high degree of lateral heterogeneity. This non-uniform distribution of constituents is characterized by mobile nanodomain clusters called rafts. Enriched by saturated phospholipids, cholesterol and proteins, rafts are considered to be vital for several important cellular functions such as signalling and trafficking, morphological transformations associated with exocytosis and endocytosis and even as sites for the replication of viruses. Understanding the evolving distribution of these domains can provide significant insight into the regulation of cell function. Giant vesicles are simple prototypes of cell membranes. Microdomains on vesicles can be considered as simple analogues of rafts on cell membranes and offer a means to study various features of cellular processes in isolation.

In this work, we employ a continuum approach to model the evolution of microdomains on the surface of Giant Unilamellar Vesicles (GUVs). The interplay of species transport on the vesicle surface and the mechanics of vesicle shape change is captured using a chemo-mechanical model. Specifically, the approach focuses on the regime of vesicle dynamics where shape change occurs on a much faster time scale in comparison to species transport, as has been observed in several experimental studies on GUVs. In this study, shape changes are assumed to be instantaneous, while species transport, which is modeled by phase separation and domain coarsening, follows a natural time scale described by the Cahn–Hilliard dynamics.

The curvature energy of the vesicle membrane is defined by the classical Canham–

Helfrich–Evans model. Dependence of flexural rigidity and spontaneous curvature on the lipid species is built into the energy functional. The chemical energy is characterized by a Cahn–Hilliard type density function that intrinsically captures the line energy of interfaces between two phases. Both curvature and chemical contributions to the vesicle energetics are consistently non-dimensionalized.

The coupled model is cast in a diffuse-interface form using the phase-field framework. The phase-field form of the governing equations describing shape equilibrium and species transport are both fourth-order and nonlinear. The system of equations is discretized using the finite element method with a uniform cubic-spline basis that satisfies global higher-order continuity. For shape equilibrium, geometric constraints of constant internal volume and constant surface area of the vesicle are imposed weakly using the penalty approach. A time-stepping scheme based on the unconditionally gradient-stable convexity-splitting technique is employed for explicit time integration of nonlocal integrals arising from the geometric constraints.

Numerical examples of axisymmetric stationary shapes of uniform vesicles are presented. Further, two- and three-dimensional numerical examples of domain formation and growth coupled to vesicle shape changes are discussed. Simulations qualitatively depicting curvature-dependent domain sorting and shape changes to minimize line tension are presented. The effect of capturing the difference in time scales is also brought out in a few numerical simulations that predict a starkly different pathway to equilibrium.

To my mother Indira, my father Srinivasan and my wife Vindhya

Contents

List of Tables

List of Figures

List of Abbreviations and Symbols

Symbols

κ	flexural rigidity associated with the mean surface curvature
κ_G	flexural rigidity associated with the Gaussian curvature
H	mean surface curvature
K	Gaussian surface curvature
H_{sp}	spontaneous curvature
L_o	liquid-ordered lipid phase
L_d	liquid-disordered lipid phase
$\mathrm{v_r}$	reduced volume
σ	line tension
T	temperature
T_m	melting temperature
T_c	critical temperature
f	double-well potential associated with the chemical energy density
g	double-well potential associated with the energy density of the phase field
ϕ	order parameter representing vesicle shape
c	order parameter representing species concentration
k_B	Boltzmann constant
λ	line tension parameter associated with the gradient in c

α	line tension parameter associated with the gradient in ϕ
μ	chemical potential
M	species mobility
δ_S	approximate delta function
Ω	computatational domain
Ω_{in}	internal domain of the vesicle
Ω_{out}	external domain of the vesicle
ϵ_ϕ	dimensionless interface length associated with ϕ
ϵ_c	dimensionless interface length associated with c
$\mathbf{n}$	normal pointing out of a surface
H_ϕ	diffuse-interface representation of the mean curvature
E_{c}	chemical free-energy functional
E_{m}	mechanical free-energy functional
E_{gc}	penalty energy functional associated with geometric constraints
E	total free-energy of the membrane
α_v	penalty parameter associated with volume constraint
α_a	penalty parameter associated with surface area constraint
α_m	penalty parameter associated with zero-flux constraint
ν	characteristic measure of chemical energy density
$\boldsymbol{1} - \mathbf{n} \otimes \mathbf{n}$	projection operator
t	time
τ	pseudo-time
Γ	boundary of the domain
Γ_d	Dirichlet boundary
Γ_h	Neumann boundary
γ_1, γ_2	convexity-splitting constants

Ψ	product of smoothed a signum function and an approximate delta function
υ	SUPG stability parameter
S	vesicle surface
d	distance function
h	grid-size

Abbreviations

GUVs	Giant Unilamellar Vesicles
SUPG	Streamline Upwind Petrov Galerkin

Acknowledgements

I thank my advisor, Professor John Dolbow, for letting me be a part of his excellent team and for giving me the opportunity to work on a novel topic for my research. I express my deep sense of gratitude for his support and encouragement, and of course, his patience through all my years at graduate school. I also thank Professor Tod Laursen for mentoring me during the initial years of my graduate studies at Duke.

I am lucky to have worked with excellent collaborators for my research. I deeply thank Professor Isaac Harari for providing great insight into challenging aspects of my initial work. I admire his clarity of thought and his ability to explain difficult topics in simple logical steps. I thank Professor Eliot Fried for collaborating with us for this research and for hosting me during my short visit to McGill University in Montreal. I also thank Professors Elliot Elson and Guy Genin for hosting us at Washington University in St. Louis for interesting discussions on the vesicles project.

I gratefully acknowledge the financial support of the National Institutes of Health through grants GM084200 and HL079165 and the National Science Foundation through grants 0825839 and 0826518, due to which this work was made possible.

I would also like to thank my remaining committee members. Professor Thomas Witelski for his inspirational teaching and his willingness to serve on my committee in spite of his other obligations. Professor Wilkins Aquino for very inspiring and motivational lectures on a subject which can so easily be relegated to an unending series

of theorems and proofs. I also thank him for letting me use his high performance cluster, without which three-dimensional simulations would have just remained as thoughts. Professor Xuanhe Zhao for his wonderful and thought provoking lectures. Professor Guglielmo Scovazzi for introducing us to a very challenging topic in finite elements and to some delightful Italian Panettone!

I would also like to thank many of my previous mentors at school and work, especially Professor Yogesh Desai, Professor R. Jagadish, Professor A. Prabhakar, Dr. Sudhakar Marur and Dr. T.R. Sreeram for their inspiration and encouragement.

I express my gratitude to Mahmood Sayed for the innumerable times he has helped me with a systems issue. Mahmood has a solution to any IT issue you pose for him and amazingly, does it in real-time!

I thank Ruby Nell Carpenter and Yvonne Connelly for being of so much help during my stay at graduate school. They can cheer you up any season of the year!

I thank Alice Dolbow for being such a gracious host to us on so many occasions. We always enjoyed Alice's cheerful company garnished with her trademark wit and of course, tons of food!

Many dear friends have made my experience in graduate school memorable. Abhijit Mahato, the reason for me to join Duke, was one of the most confident and fun-loving young man I have ever come across. We all deeply miss him. Frederick Owusu-Nimo is a tremendous concoction of energy, enthusiasm and mischief who infused so much fun into our graduate school life. I have enjoyed spending time with my dear friends Harishanker Gajendran and Chandrasekhar Annavarapu who have been like extended family to me. I consider myself lucky to have had a chance to interact with exceptional postdoctoral fellows, Martin Hautefeuille and Alex Kelly, with whom discussions are both educational and entertaining! It is indeed a great pleasure to share the same lab with Temesgen Kindo, who I consider is phenomenal in his mastery of topics and who amazes me with his unending thirst for knowledge.

I would also like to thank my friends Justin and Marusa Pogacnick, Tae-Yeon Kim, Wen Jiang and, Kumar and Deepti Reddi, who have been so much fun to spend time with! My friends Narendra Hardikar and Harith Vadari who have both been inspiring and loads of fun to work with. My friends Karthik and Aswatlh for being such wonderful pals and for frequently serving as a reality-check to me!

I thank my dear parents and my uncle for their unconditional love and constant support while things have not been easy on them. My parents-in-law for their understanding and support through all these years of my graduate studies. Finally, I want to thank my dear soulmate Vindhya. I consider myself lucky to be a part of her life. Her unending energy, childlike enthusiasm and unyielding love have guided me through many difficult times and made my experience more wholesome. Life has been so much more enjoyable in her company and I wholeheartedly look forward to our future together.

1

Introduction

Biomembranes form the building blocks of cellular structures. They compartmentalize biological systems by defining a boundary between the internal organelles of the cell and the surrounding medium. Biomembranes are selectively permeable and hence regulate the inflow and outflow of constituents such as ions, nutrients and cellular waste. Biological functions of cells are strongly influenced by the properties and morphology of biomembranes. Membranes are extremely compliant in bending but comparatively rigid under lateral deformation. This unique combination of elastic properties allows migrating cells (such as erythrocytes) to travel long distances through narrow body channels without loss of ions Sackmann (1995). The two-dimensional-fluid character of biomembranes entails a large increase in the efficiency of diffusion controlled processes and the lateral organization of membranes may be controlled externally (e.g., by the adsorption of proteins) Sackmann (1995). In addition, membranes do not resist shear and this fluid nature of the surface is a key factor responsible for a plethora of shape transformations including budding, fission, and adhesion associated with cellular functions such as exocytosis and endocytosis.

1.1 Composition of cell membranes

Cell membranes are generally composed of several kinds of mobile lipids, cholesterol and proteins. Whereas proteins mediate traffic and serve as signaling devices, lipids provide a fluid matrix within which transmembrane proteins are free to migrate and render a membrane largely impermeable to most water-soluble solutes. Cholesterol enhances the packing of the acyl chains of phospholipids in the hydrophobic phase of the bilayer, increases its mechanical stiffness, and reduces its permeability (Bloch, 1983). The cytoskeleton, a polymeric network anchored to the membrane, offers stability to the structure of the membrane. A schematic of a plasma membrane is shown in Figure 1.1. Membranes are typically comprised of phospho-lipid bilayers which

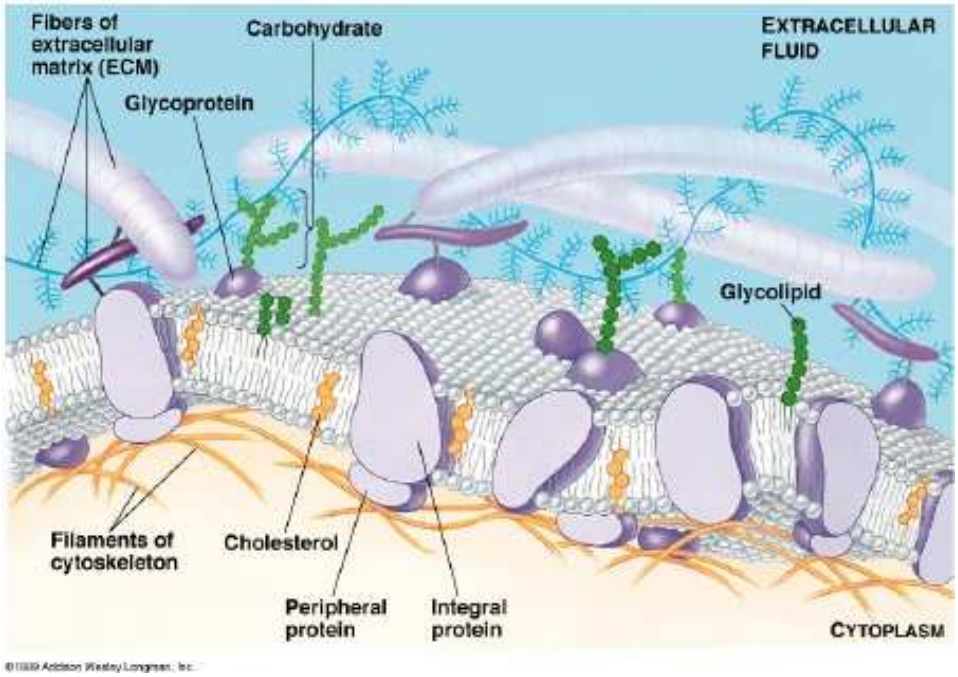

FIGURE 1.1: A schematic representation of plasma membrane. Source: Gallant (2003).

are a few nanometers in thickness. Phospho-lipid molecules are amphiphilic - they are characterized by a hydrophilic polar head containing phospates and hydrophobic non-polar hydrocarbon chains as tails. These features lend a self-organizing property

to phospho-lipid molecules in aqueous solutions. For certain values of temperature and concentration, these lipids organize themselves into bi-layers such that the hydrophilic heads are exposed to the aqueous medium while the hydrophobic tails face each other. A schematic of a phospho-lipid molecule is illustrated in Figure 1.2. Furthermore, bilayers tend to form closed surfaces, as shown in Figure 1.3, to avoid

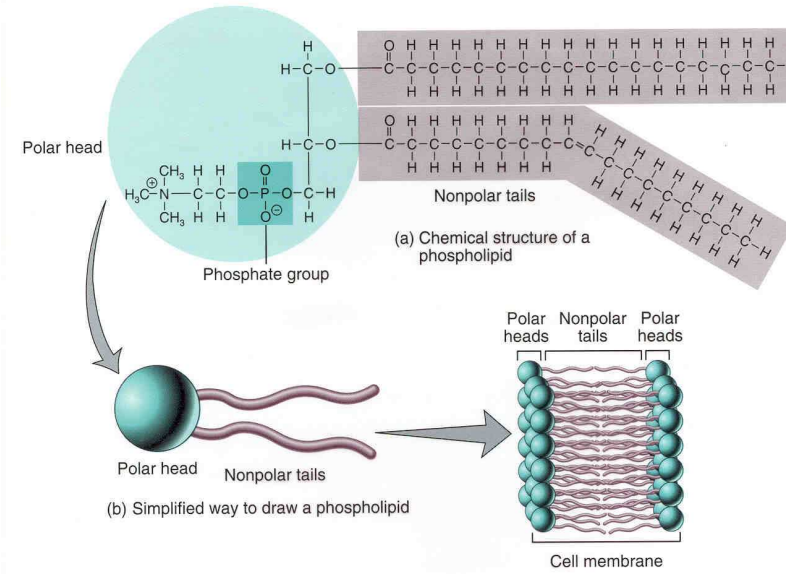

FIGURE 1.2: A schematic section of a phospho-lipid molecule and a corresponding bilayer sheet. Source: Wissmann (2006).

exposure of the bilayer edges to the aqueous medium.

Lipids can be broadly classified into two types: saturated and unsaturated. The names relate to the associated fatty acid tails of the lipids. Saturated fatty acids are saturated with hydrogen atoms and possess a straight structure, as depicted by the perfectly horizontal tail in Figure 1.2*a*. Unsaturated fatty acids are comprised of lesser hydrogen atoms resulting in a double-bond between carbon atoms. This double-bond introduces a kink in the structure of the fatty acid (lower tail in Figure 1.2*a*). An unsaturated lipid has at least one unsaturated fatty acid chain while a saturated lipid has none. On account of kinks in the hydrocarbon tail, unsaturated lipids do not pack into a regular structure in contrast to saturated lipids. The

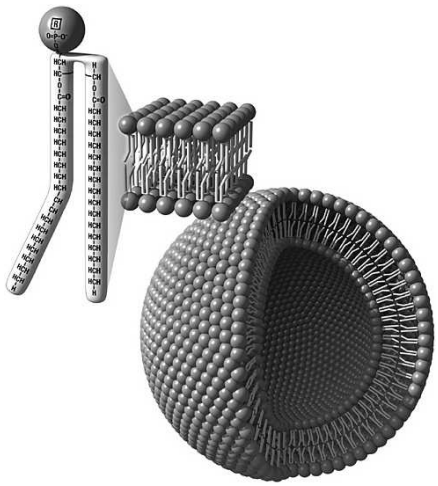

FIGURE 1.3: Schematic of a phospho-lipid bilayer forming a closed surface. Source: Deamer and Hazen (2006).

structure of the hydrocarbon chain leads to unsaturated lipids having lower melting temperatures than saturated lipids. These characteristics have an important consequence on the microstructure of cell membranes as will be discussed in the next Section.

1.2 Microstructure of cell membranes

The spatial distribution of lipids, proteins and cholesterol on the surface of cell membranes is known to be highly heterogeneous. This lateral heterogeneity is thought to result from preferential packing of saturated lipids (sphinogolipids) and cholesterol into clusters floating in a matrix of unsaturated lipids (phosphatidylcholine) (Simons and Ikonen, 1997). Further, proteins are known to associate themselves with these clusters. Such clusters of saturated lipids with cholesterol and associated proteins are referred to as *rafts*. Lateral heterogeneity resulting in the formation of rafts are understood to have important functional relevance in cells (Simons and Ikonen, 1997; Brown and London, 1998).

Rafts are considered to be in the size range of 10–200 nm. They are heterogeneous,

highly dynamic, sterol and sphingolipid-enriched domains that compartmentalize cellular processes. They are thought to be in the liquid ordered phase (Pike, 2006). Rafts are believed to play an important role in regulating protein activity (Hess et al., 2005) that may in turn affect biological processes such as trafficking and signalling (Pike, 2006; Simons and Ikonen, 1997) and are known to be central to the replication of viruses (Ono and Freed, 2001). They are also thought to be responsible for morphological transformations such as budding and fission and also for membrane adhesion and fusion (Takeda et al., 2003). A comprehensive survey of theoretical models describing the physical principles governing raft formation and associated experimental approaches is provided by Elson et al. (2010).

1.3 Vesicle membranes as prototypes of cells membranes

Generally, biological membranes can have highly complicated structures with hundreds of types of lipids and proteins. While it is acknowledged that studying the distribution of species on a cell membrane can provide significant insight into the regulation of cell function, experimental and theoretical investigations of actual cell membranes can be extremely challenging. To probe such regulatory behavior, experiments are performed on simple model bilayer membranes typically comprised of phospho-lipids. Vesicles are simple forms of closed biomembranes. Bilayers that are a few nanometers thick form vesicles that range between 50 nm to tens of micrometers in diameter (Deseri et al., 2008). Larger vesicles are commonly referred to as Giant Unilamellar Vesicles (GUVs). Multi-component vesicles exhibit a rich phase transition and phase separation behavior. Model vesicle membranes consisting of two or more lipid species have been observed with a spectacular array of lateral heterogeneity, as shown in Figure 1.4. As prototypical models for cells, vesicles offer a means to study various features of cellular processes in isolation. Recent experimental studies (Baumgart et al., 2003) strongly suggest that vesicle membranes made of ternary

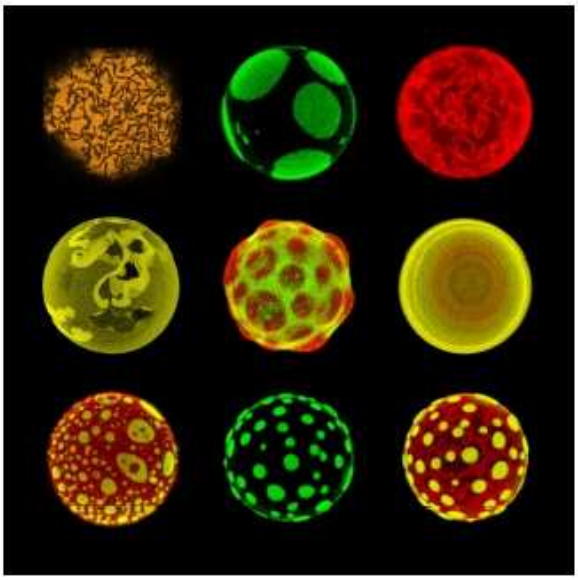

FIGURE 1.4: Fluorescence microscopy images of giant unilamellar vesicles exhibiting lateral heterogeneity. Source: de la Serna (2007).

mixtures of saturated and unsaturated lipids, and cholesterol can quite accurately replicate important properties of biological membranes. Figure 1.5 presents a few images published in this experimental study.

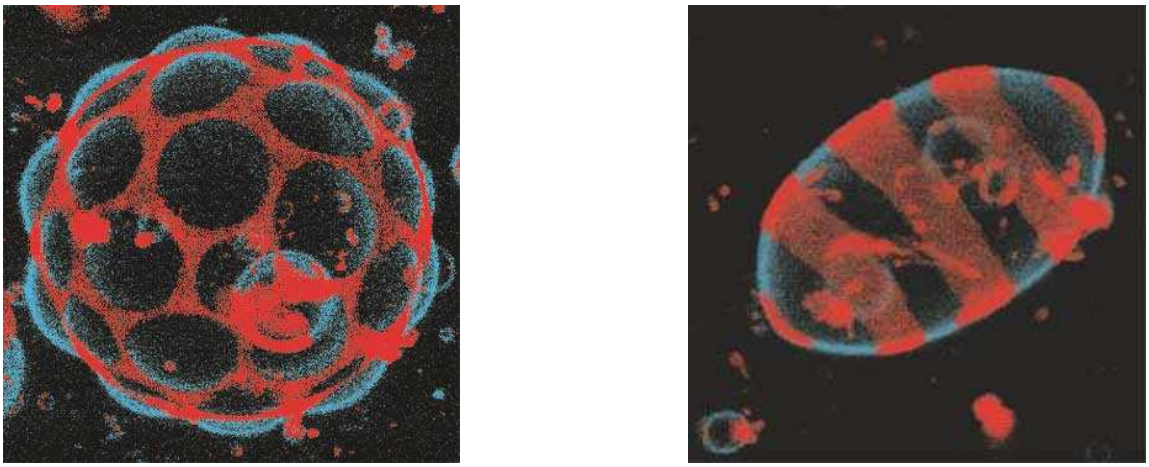

(a) (b)

FIGURE 1.5: Giant Unilamellar Vesicles showing coexistence of lipid phases. The two lipid phases are flouroscently labeled. Source: Baumgart et al. (2003).

1.4 Overview of the thesis

The study of domain formation in GUVs containing ternary lipid-cholesterol mixtures is expected to provide pathways to understand raft formation and raft behavior in cell membranes. The current work follows previous research in this direction.

We employ a continuum approach to describe the coupled process of shape change and domain formation and coarsening. While the generalized Helfrich model (Helfrich, 1973) describes the curvature energy, a Cahn–Hilliard type energy characterizes line tension. Phase separation and domain coarsening on the vesicle surface are modeled by a Cahn–Hilliard-type species evolution equation restricted to the surface. Employing the phase-field approach, the governing equations are formulated in diffuse-interface form and are numerically solved using a spline-based finite-element method.

The present work focuses on a regime of vesicle dynamics where shape change and phase separation are characterized by distinctly different time scales. Strong nonlinearities underpin the coupled phenomenon and a difference in time scales can result in starkly different pathways toward equilibrium. Several experimental studies suggest that such a regime exists. The effect of anchored polymers on vesicle morphology is reported in (Tsafrir et al., 2003). Polymers injected near a suspended vesicle anchor themselves on the vesicle surface, thereby inducing a local spontaneous curvature. Whereas bud formation was observed over a few seconds, diffusion of these polymers over the surface and consequent disappearance of the buds occured over several hundred seconds. A similar inference can be drawn from experiments on GUVs (Yanagisawa et al., 2007), wherein domain formation and coarsening were observed in the context of associated shape changes. Initial domain coarsening was found to follow a power law. When domains reached a particular size, line tension led to the formation of buds on the vesicle surface. A sudden jump was observed in

the time evolution of coarsening and this phenomenon was revealed to coincide with the formation of buds. The presence of a jump implies that the time scale for shape change is shorter than that associated with domain growth. In the present study, this difference in time scales is exaggerated. Shape changes, taken to be a consequence of shape equilibrium, are assumed to be instantaneous, while phase separation and domain coarsening follow a natural time scale dictated by parameters entering the Cahn–Hilliard type equation governing the distribution of phases. It is, however, acknowledged that the above assumption regarding time scales is not strictly valid in systems for which the viscosities of the membrane and the surrounding suspension medium are not negligible.

A comprehensive account of chemo-mechanical models describing pattern formation in biological systems is provided by Murray (2002). Time scales associated with mechanical deformation are prescribed via inertial and/or viscous effects. In the present work, we consider vesicles with negligible membrane viscosity and suspended in an inviscid fluid at rest. In this scenario, shape changes can be considered to be quasi-static. This is similar in spirit to models that couple phase separation and elasticity (Garcke, 2003; Sagui et al., 1994; Akira, 1989; Yeon et al., 2005; Bartkowiak and Pawlow, 2005) and models describing pattern formation on surfaces (Suo and Lu, 2000). The dominant time scale is then determined by the diffusive transport.

In modeling vesicles (Biben et al., 2005; Campelo and Hernández-Machado, 2006; Wang and Du, 2008; Lowengrub et al., 2009), the phase-field method provides an implicit representation of the vesicle surface. A comprehensive account of the kinematic relations and geometric identities occurring in the phase-field framework is provided in Fried and Gurtin (1996).

In the present study, an approximation to the diffuse-interface form of the mean curvature is derived based on the partition of energy associated with the phase field. Similarly, an argument leading to an expression for the approximate delta function

used to transform surface integrals into equivalent volume integrals is presented. A derivation of the diffuse-interface form of the curvature energy is also provided.

In the process of employing a coupled model, researchers in the field (Wang and Du, 2008; Lowengrub et al., 2009) use a dimensionless form of the chemical energy (Cahn–Hilliard-type) while the curvature energy remains dimensional. In the current work, both contributions to the energy are rendered dimensionless. This leads to an appropriate scaling term and a consistent description of energetic contributions.

The thesis is organized as follows. Chapter 2 gives a brief overview of the continuum description of vesicles. Ingredients of the spontaneous curvature model along with the physical origins of the parameters entering the model are described. The evolution of microdomains on membranes analogous to phase separation in binary alloys is briefly explained. Chapter 3 provides an outline of the phase-field framework in the context of vesicles. Dimensionless diffuse-interface expressions for the mean surface curvature, the approximate delta function, the vesicle surface area and the vesicle internal volume are derived. Chapter 4 lays the groundwork for the continuum description of vesicles. The governing equations of the chemo-mechanical model coupling shape change and species transport are presented. The chemo-mechanical model, characterized by fourth-order partial differential equations, is cast within a finite element framework using a B-spline basis. Chapter 5 presents the details of building a finite element basis with uniform splines. The performance of B-spline based finite element method is presented with several benchmark numerical examples of second and fourth-order boundary value problems and a fourth-order intial boundary value problem. Chapter 6 describes the numerical modeling of vesicles with details on spatial and time discretization, and the SUPG method to stabilize the pure advection equation used for data extension normal to the surface. Axisymmetric, two-dimensional and three-dimensional numerical examples are discussed in Chapter 7. A qualitative comparison to experimental observations is provided for

some of the examples. The effect of the distinct difference in time scales between species transport and shape change is studied. Chapter 8 presents a summary of the work and concludes the thesis.

2

Background

2.1 Overview

Many numerical methods have been employed to study domain formation and evolution in synthetic membranes. Molecular dynamics and Monte Carlo simulations have focused on studying the lipid bilayer properties (Hac et al., 2005; Zhang et al., 2007; Niemelä et al., 2007). These methods have been able to study bilayers for several nanoseconds but can be computationally prohibitive in capturing length and time scales observed on entire vesicles and biological membranes. Coarse-grained simulations (Marrink et al., 2005; Shi and Voth, 2005) model collective membrane phenomena beyond the reach of purely atomistic methods by selectively eliminating details. These models have been used to study domain formation in lipid bilayers over comparatively larger scales. Continuum models provide a viable alternative to model bilayer vesicles over much larger spatial and temporal scales. In this study, we use a continuum description to model the chemical and mechanical aspects of microdomain evolution on vesicles.

Continuum models treat the vesicle membrane as an elastic surface. Giant Unil-

amellar Vesicles are generally composed of bilayers that are a few nanometers thick. Vesicles can be several tens of micrometers in size. On account of this large diameter to thickness ratio GUVs can be considered as surfaces embedded in three dimensional Euclidean space. Continuum modeling of vesicles have followed two distinct approaches. In the first approach, equilibrium equations of shape are obtained by minimizing a global energy functional (Canham, 1970; Helfrich, 1973; Seifert et al., 1991). For an incompressible membrane, the associated energy density i.e., the energy per unit membrane area is characterized by the mean surface curvature H and the Gaussian surface curvature K (Seifert, 1997). The second approach is based on the force and moment balance equations described on a local membrane area element (Jenkins, 1977; Evans and Skalak, 1980). In fact, the two approaches have been shown to be equivalent by Powers et al. (2002). Several variants of the first approach exist. In the present work, we employ the spontaneous curvature (SC) model which is a popular variant of the first approach.

2.2 The spontaneous curvature model

Canham (1970), Helfrich (1973) and Evans (1974) first proposed a purely mechanical model for studying the equilibrium shapes of single component vesicles such as red blood cells. In its most general form, the energy functional reads,

$$E = \int_S \frac{1}{2}\kappa \left(H - H_{sp}\right)^2 \, \mathrm{d}a + \int_S \kappa_G K \, \mathrm{d}a \tag{2.1}$$

where, S represents the membrane surface, κ and κ_G are the flexural rigidities corresponding to the mean curvature H and Gaussian curvature K of the membrane. Liquid-ordered (L_o) lipid phases (discussed in Section 2.4) are estimated to have a mean flexural rigidity on the order of 10^{-19} J (Baumgart et al., 2005). The liquid-disordered (L_d) phase is estimated to have a lower flexural rigidity, but of the same

order. Baumgart et al. (2005) also estimate the absolute difference in Gaussian moduli of L_o and L_d phases to be on the order of 10^{-19} J. H_{sp} is a phenomenological term referred to as the *spontaneous curvature*. The spontaneous curvature of a bilayer membrane is taken to represent the curvature of a bilayer in its natural state.

2.2.1 Origins of spontaneous curvature in biomembranes

Membrane curvature is understood to be dynamically modulated as an active means to create membrane domains and to organize centers for membrane trafficking (McMahon and Gallop, 2005). Several reasons are attributed for the existence of spontaneous curvature. In general, it is considered as a measure of the degree of asymmetry in upper and lower monolayers. The asymmetry can occur due to different molecular composition of monolayers or different properties of aqueous solutions on either side of the bilayer (Döbereiner et al., 1999). Further reasons include locally varying headgroup compositions or tail group conformations in lipid molecules, helix insertion, shape of transmembrane proteins, scaffolding by proteins, etc. Figure 2.1 shows a few examples of possible causes inducing a natural curvature in membranes.

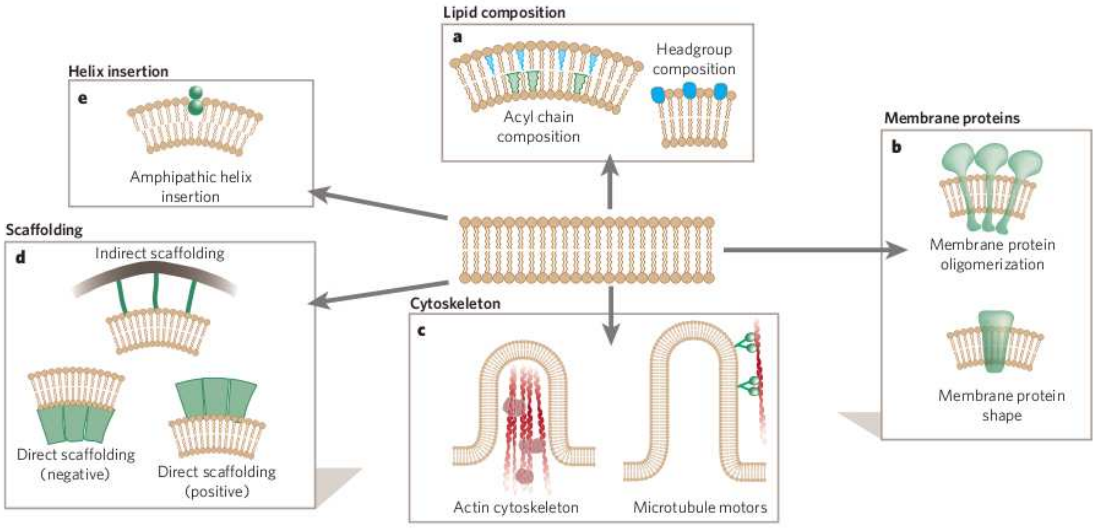

FIGURE 2.1: Possible mechanisms inducing spontaneous curvature in bilayer membranes. Source: McMahon and Gallop (2005).

2.2.2 Guassian curvature energy in uniform bilayers

For uniform bilayers with a constant Gaussian rigidity κ_G, the Helfrich energy given by (2.1) is further simplified. From the Gauss–Bonnet theorem (O' Neill, 2006), the integral of the Gaussian curvature over a closed surface is a constant given by $4\pi(1-g)$, where g is the genus of the surface (i.e., the number of holes in the surface). As a consequence, Gaussian energy does not influence shape changes of bilayer membranes with a uniform composition of lipids when topological changes are absent.

2.2.3 Stationary shapes of uniform bilayers

Minimization of the energy functional (2.1) subject to constraints of constant surface area and internal volume leads to the governing equations for stationary shapes of vesicles. Preliminary results with this hypothesis showed good promise in modeling simple vesicle membranes. Using a simplified version of (2.1), Canham calculated the bending energy associated with different axisymmetric shapes with identical surface area and internal volumes. The biconcave shape, typical of human red blood cells, was found to minimize the curvature energy, as shown in Figure 2.2. A systematic study of stationary shapes of uniform bilayer vesicles was performed by Seifert et al. (1991). The spontaneous curvature H_{sp} and the reduced volume $\mathrm{v_r}$ were identified as the key non-dimensional parameters influencing the stationary shapes of vesicles. The parameter $\mathrm{v_r}$ can be considered as a measure of the volume of a vesicle in comparison to the volume of a sphere with an identical surface area. A complementary approach is to use a measure of the excess surface area of a vesicle as compared to a sphere of equivalent volume. The reduced volume $\mathrm{v_r}$ is given as

$$\mathrm{v_r} = \frac{V}{(4\pi/3){R_0}^3}, \qquad \text{where} \qquad R_0 = \left(\frac{A}{4\pi}\right)^{\frac{1}{2}}. \tag{2.2}$$

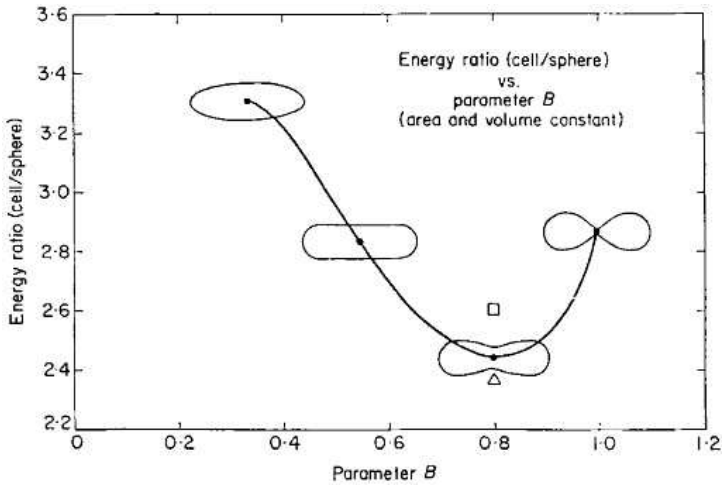

FIGURE 2.2: Bending energy ratio (cell/sphere) as a function of shape. Source: Canham (1970).

It is evident that $0 < \mathrm{v_r} \leqslant 1$. A sphere is characterized by $\mathrm{v_r} = 1$. Phase diagrams showing different branches of stationary shapes as a function of the reduced volume were derived for various values of non-dimensionalized spontaneous curvature. Figure 2.3 shows the phase diagram and shapes for different values of $\mathrm{v_r}$ with $H_{\mathrm{sp}} = 0$. The prolate, oblate and stomatocyte branches of shapes are indicated in the phase diagram.

More recently, Biben and Misbah (2003), have modeled the dynamic behavior of homogeneous vesicles in a small Reynold's number flow by coupling the curvature energy to Navier Stokes' equations of fluid flow. Both kinetics towards equilibrium shapes and dynamic vesicle behaviors such as tank trading and tumbling have been modeled numerically.

2.3 Multi-phase biomembranes

Shape transformations of single component vesicles have been quite comprehensively studied. However, the mathematical modeling of phase transition/phase separation coupled to the shape change of multi-component vesicles can be challenging. Initial

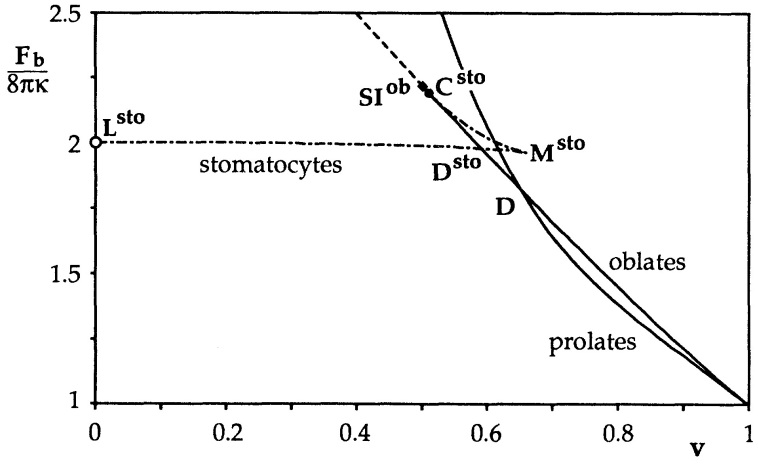

(a)

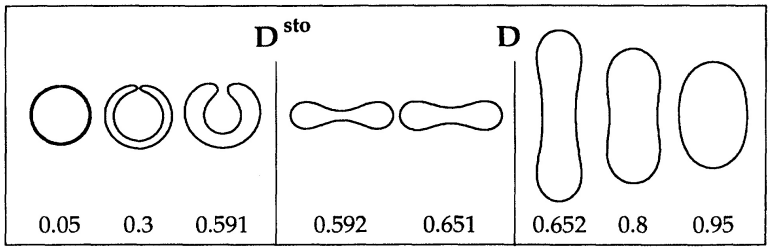

(b)

FIGURE 2.3: (a) Phase diagram and (b)stationary vesicle shapes as a function of reduced volume for '0' spontaneous curvature. Source: Seifert et al. (1991).

studies have focused on modeling stationary shapes of two-phase vesicles in which the phases are completely separated. A *line tension* energy is introduced (Jülicher and Lipowsky, 1996) along the interface of the two phases. Equation (2.1) is then modified to include spatially varying properties and the line tension energy such that

$$E_{net} = E_b^{\alpha} + E_b^{\beta} + E_l^{\alpha\beta} \tag{2.3}$$

where, α and β are the two phases, E_b^{α} and E_b^{α} are the bending energies similar to (2.1) for each phase. $E_l^{\alpha\beta}$ represents the line tension energy of the interface and is given by

$$E_l^{\alpha\beta} = \int_S \sigma \, \mathrm{d}a, \tag{2.4}$$

where σ is the line tension. The resulting energy functional (2.3) is then minimized to obtain experimentally observed patterns of vesicle budding. Detailed analytical studies on these lines can be found in Jülicher and Lipowsky (1996), for axi-symmetric shapes. Recently, Baumgart et al. (2005) extended the above analytical model to include variations in Gaussian curvature for each of the phases so as to model budding and subsequent vesicle fission.

2.3.1 Origins of line tension in multi-phase biomembranes

Lipid phases on biomembranes can be characterized by different thicknesses. It has been experimentally observed that the liquid ordered phase L_0 is thicker in comparison to the liquid-disordered phase L_d resulting in a height mismatch at the interface (Lawrence et al., 2003). This mismatch can cause an exposure of the hydrophobic tails to the aqueous medium. The membrane avoids this configuration by distorting at the interface (Kuzmin et al., 2005). This results in an energetic cost per unit length resulting in line tension at the phase boundaries. Theoretical models (Kuzmin et al., 2005) relate line tension to physical properties of membranes such as phase-height mismatch, lateral tension and spontaneous curvature. These models suggest a quadratic variation of line tension with phase-height mismatch. Baumgart et al. (2005) estimate the line tension at the boundary of coexisting phases in a lipid bilayer to be on the order of 10^{-13} N. Recent studies (García-Sáez et al., 2007) emphasize that while line tension mainly influences the kinetics of domain growth on supported (planar) bilayers, it also causes out-of-plane deformations in GUVs, as shown in Figure 2.4. In the present study a continuum description of line tension is introduced through an energy associated with high gradients in lipid species concentration at phase interfaces.

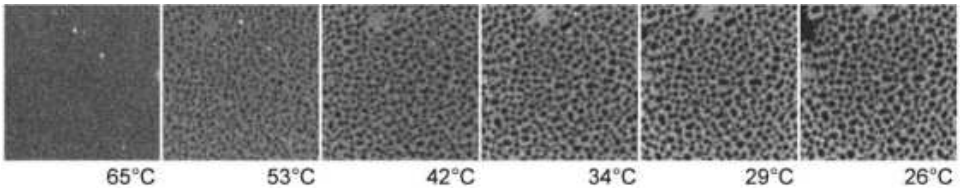

(a)

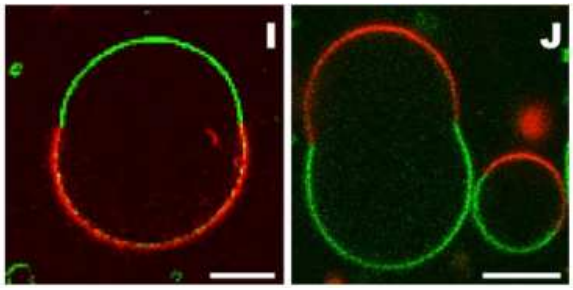

(b)

FIGURE 2.4: Experimental images showing line tension induced (a) domain growth on planar membranes and (b) out-of-plane deformations in closed membranes. Source: García-Sáez et al. (2007).

2.4 Phase separation in GUVs as a model for membrane raft formation

Thermally and chemically induced phase separation have been observed to lead to domain formation on vesicles (Sackmann, 1995). GUVs of specified composition can separate into phases that resemble rafts (Figure 1.5). Such phase behavior depends on the composition of the lipid bilayer membrane as well as temperature and pressure. As discussed in Section 1.1, the melting temperature T_m of lipids with longer saturated hydrocarbon tails is higher than for lipids with shorter unsaturated tails. Single component bilayer membranes exist in a solid ordered S_o gel phase below T_m. For $T > T_m$ the lipid is in a disordered liquid phase (L_d). In a binary membrane composed of higher and lower melting lipids with phase transition temperatures T_{mh} and T_{ml}, the lipids separate into solid and liquid phases ("micro-domains") enriched in the higher and lower melting components, respectively, at a temperature

T_t such that $T_{ml} < T_t < T_{mh}$. Coexisting liquid domains are not observed in binary lipid membranes in the absence of cholesterol (Veatch and Keller, 2005). In ternary systems that contain higher and lower melting lipids as well as cholesterol large liquid phases ($\geqslant 1\mu m$) can coexist over a wide range of compositions and temperatures (Veatch and Keller, 2005). In addition to the L_d phase there is also a liquid ordered (L_o) phase with ordered and extended hydrocarbon chains in which fast lateral and rotational diffusion are observed. The L_o phase in the ternary systems replaces the S_o phase in binary systems that lack cholesterol.

2.4.1 Free energy of a binary mixture

The free energy of a binary mixture of lipids can be treated analogous to the free energy of an immiscible binary alloy. Based on the non-ideal solution theory, the total free energy of a mixture composed of pure species a and b can be written as (Flory, 1942)

$$f = x_a G_a + x_b G_b + k_B T(x_a \ln x_a + x_b \ln x_b) + 2k_B T_c x_a x_b, \tag{2.5}$$

where, x_a and x_b represent the mole fraction of each species, G_a and G_b represent the free energy of each of the pure species, k_B is the Boltzmann constant, T is the absolute temperature and T_c the critical temperature for phase separation. Thus the total free energy in (2.5) is composed of the bulk free energy of the pure species ($x_i G_i$), the entropy of mixing ($k_B T x_i \ln x_i$) and the enthalpy of mixing ($2k_B T_c x_a x_b$). The expression for the total free energy (2.5) can be further simplified by eliminating the bulk free energy of the pure species which remains constant. The dimensionless version of the free energy can then be written as

$$f^* = \frac{f}{k_B T} = c_a \ln c_a + (1 - c_a) \ln(1 - c_a) + \chi c_a (1 - c_a), \tag{2.6}$$

where, c_a is the volume fraction of species a corresponding to x_a and χ is a dimensionless quantity referred to as the interaction parameter $\chi = 2T_c/T$. The plot of

the free energy for the three possible ranges of T relative to T_c is given in Figure 2.5. It is noted that the free energy permits two stable equilibria only when $T < T_c$.

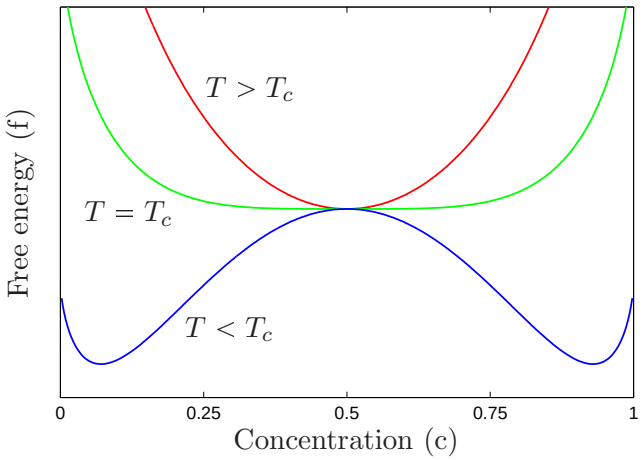

FIGURE 2.5: Schematic representation of the free energy of a binary mixture as a function of temperature.

Following (2.5), the total free energy of a mixture can be obtained by introducing an energy penalty for the interfaces and is given by

$$E_c = \int_\Omega f(c) + \frac{\lambda}{2}|\nabla c|^2 \, \mathrm{d}v \tag{2.7}$$

where λ is a parameter penalizing gradients in the volume fraction c. The functional (2.7) represents the well-known Cahn–Hilliard type energy (Cahn and Hilliard, 1958). The continuity condition derived from (2.7) gives the Cahn-Hilliard equation for phase separation:

$$\begin{aligned} &\frac{\partial c}{\partial t} + \nabla \cdot \mathbf{j} = 0, \\ &\mathbf{j} = -M \nabla \mu, \\ &\mu = \frac{\delta E_c}{\delta c}. \end{aligned} \tag{2.8}$$

where, $\mathbf{j}$ is the flux, μ is the chemical potential and M represents species mobility. Heuristically, the diffusivity D of the species relates to the mobility M as $D \sim k_B T M$. Kahya et al. (2003) report diffusivities for raft-exhibiting membranes on the order of 10^{-8} cm/s.

The Cahn–Hilliard theory of spinodal decomposition was originally proposed to model phase separation in binary metallic alloys (Cahn and Hilliard, 1958). It models continuous phase transformations, where inifinitesimal variations in volume fractions of constituents initiate a spontaneous decomposition from an initial state that is essentially unstable. Typically, such continuous transformations can begin over large regions and the entire volume can transform simultaneously. In the present work, we employ the Cahn–Hilliard theory as a model to study phase separation and domain formation on vesicles.

3

A Phase-Field Framework for Vesicles

In the present work, a phase-field approach is used to cast all governing equations in a diffuse-interface form. This is motivated by the desire to provide an implicit description of the vesicle mid-surface S by a three-dimensional layer of controllable width. An auxiliary quantity, referred to as the phase field ϕ, is introduced. This varies smoothly yet steeply across the layer. The phase-field approach not only eliminates the need to explicitly track sharp surfaces, but also naturally allows for topological changes. As depicted in Figure 3.1(a), ϕ varies between $\phi = -1$ (vesicle interior) and $\phi = 1$ (vesicle exterior) and its zero level-set ($\phi = 0$) represents S. Moreover, as depicted in Figure 3.1(b), ϕ depends smoothly on the signed distance d to S defined for any point $\boldsymbol{x}$ not belonging to S by

$$d(\boldsymbol{x}) = \begin{cases} -r(\boldsymbol{x}) & \text{if } \boldsymbol{x} \in \Omega_{\text{in}}, \\ r(\boldsymbol{x}) & \text{if } \boldsymbol{x} \in \Omega_{\text{out}}, \end{cases}$$

where $r(\boldsymbol{x})$ is the normal distance between $\boldsymbol{x}$ and S.

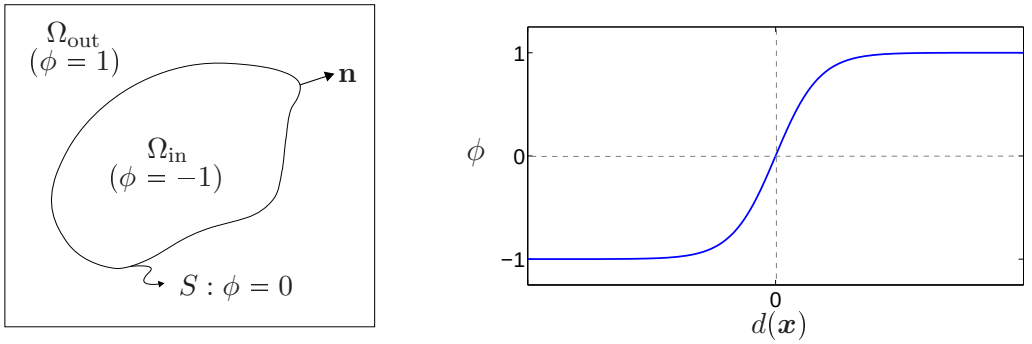

(a) Implicit surface (b) Phase field

FIGURE 3.1: (a) A smooth surface S is represented as the zero level-set of the phase field ϕ. (b) A representative profile of ϕ along the surface normal $\mathbf{n}$; $d(\boldsymbol{x})$ is the signed distance between S and a point $\boldsymbol{x}$ not belonging to S.

3.1 Approximate delta function

The integral over a surface S of a function f defined on S can be represented equivalently as an integral over a volume Ω via (Smereka, 2006)

$$\int_S f_S \mathrm{d}a = \int_\Omega \tilde{f}\delta_S \,\mathrm{d}v, \tag{3.1}$$

where $\tilde{f}$ is defined in a neighborhood of S and the restriction of $\tilde{f}$ to S coincides with f_S. Here, δ_S is an approximate delta function with the property

$$\int_{-\infty}^{\infty} \delta_S \,\mathrm{d}r = 1, \tag{3.2}$$

where r represents the distance along the surface normal. Figure 3.2(a) illustrates the profile of an approximate delta function with the horizontal axis representing the signed distance to the surface S. The support of δ_S is concentrated within a volume that encompasses S, as depicted in Figure 3.2(b). Essentially, δ_S restricts any function defined over Ω to a neighborhood of S.

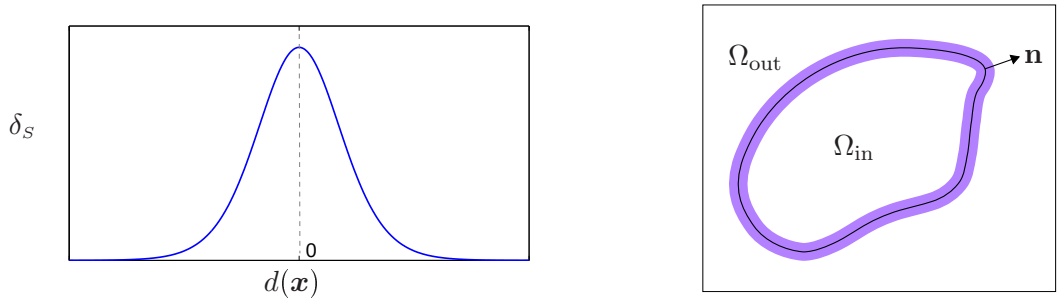

(a) Approximate delta function (b) Approximate support of δ_S

FIGURE 3.2: **(a)** Profile of an approximate delta function in the direction of the surface normal $\mathbf{n}$; $d(\boldsymbol{x}) = 0$ represents a point $\boldsymbol{x}$ on the surface **(b)** Approximate support of δ_S encompassing the surface

3.2 Phase-field description of the vesicle

Following the pioneering works of (Biben et al., 2005; Campelo and Hernández-Machado, 2006; Wang and Du, 2008), the vesicle is, at each time t, modeled by a transition layer

$$\Lambda(t) = \{\boldsymbol{x} : -1 < \phi(\boldsymbol{x}, t) < 1\} \tag{3.3}$$

containing the zero level-surface $S(t) = \{\boldsymbol{x} \in \Omega : \phi(\boldsymbol{x}, t) = 0\}$ of a phase field ϕ with range $[-1, 1]$ as illustrated in Figure 3.1(b). What remains of Ω consists, at each time t, of the regions

$$\Omega_{\text{in}}(t) = \{\boldsymbol{x} : \phi(\boldsymbol{x}, t) = -1\} \tag{3.4}$$

and

$$\Omega_{\text{out}}(t) = \{\boldsymbol{x} : \phi(\boldsymbol{x}, t) = 1\} \tag{3.5}$$

inside and outside the vesicle.

Tacit to the phase-field description is the assumption that $\nabla\phi$ does not vanish in the interior of the transition layer Λ. As a consequence of this assumption, Λ is comprised by level surfaces of ϕ.

Also tacit to the phase-field description is the assumption that the thickness of the transition layer in the direction normal to the level surface of ϕ is small in

comparison to the characteristic linear dimension, say L, of Ω. This assumption is satisfied provided that the component $\nabla\phi \cdot \mathbf{n} = |\nabla\phi|$ of $\nabla\phi$ normal to the level sets of ϕ obeys

$$L|\nabla\phi| \gg 1. \tag{3.6}$$

Until further notice, dependence on time is suppressed (without loss of generality).

We now derive approximations for quantities that are important in describing the shape energetics of the vesicle. In particular, expressions for the mean surface curvature, volume enclosed by the vesicle surface and the surface area of the vesicle are derived. Further, an expression for the approximate delta function is obtained based on the phase-field representation of the vesicle surface area. The concept of equipartition of phase field energy (Fried, 2006) plays a pivotal role in the derivations and is discussed in the following section.

3.2.1 Energy partition for the vesicle

The simplest phase-field theories involve free-energy functionals of the form

$$E_\phi = \int_\Omega \left(g(\phi) + \frac{\alpha}{2}|\nabla\phi|^2 \right) \mathrm{d}v, \tag{3.7}$$

where g is a smooth double-well potential and $\alpha > 0$ is a constant penalizing the interface energy. For the present purposes, suppose that g is even about $\phi = 0$, so that

$$g(-\phi) = g(\phi), \qquad -1 \leqslant \phi \leqslant 1. \tag{3.8}$$

Suppose, further, that g has minima at $\phi = \pm 1$, where it vanishes, so that, by the assumed smoothness of g, both g and its derivative g' must vanish at $\phi = \pm 1$:

$$g(\pm 1) = 0, \qquad g'(\pm 1) = 0. \tag{3.9}$$

Finally, suppose that g has an isolated local maximum at $\phi = 0$. Then, on account of $(3.9)_1$, g must satisfy

$$0 < g(\phi) < g(0), \qquad -1 < \phi < 1. \tag{3.10}$$

To understand the behavior of ϕ within a transition layer separating regions in which $\phi = -1$ and $\phi = 1$, it is convenient to work with a dimensionless version of the free-energy functional (3.7). To achieve this, let

$$\boldsymbol{x}^* = \frac{\boldsymbol{x}}{L} \tag{3.11}$$

denote the dimensionless counterpart of a generic point x in Ω. Further, let ∇^* and $\mathrm{d}v^*$ denote the gradient operator and volume element on the dimensionless counterpart

$$\Omega^* = \{\boldsymbol{x}^* : L\boldsymbol{x}^* \in \Omega\} \tag{3.12}$$

of Ω. Let ϕ^*, defined consistent with

$$\phi^*(\boldsymbol{x}^*) = \phi(\boldsymbol{x}), \tag{3.13}$$

denote the counterpart of ϕ defined on Ω^*. It can be noted that, by (3.11) and (3.13),

$$\nabla\phi(\boldsymbol{x}) = \frac{\nabla^*\phi^*(\boldsymbol{x}^*)}{L}, \tag{3.14}$$

Noting that g has dimensions of energy per unit volume, the free-energy functional in (3.7) can be non-dimensionalized as

$$E^*_{\phi^*} = \frac{E_\phi}{L^3 g(0)} = \int\limits_{\Omega^*} \Big(\frac{g(\phi)}{g(0)} + \frac{1}{2}\frac{\alpha}{L^2 g(0)}|\nabla^*\phi^*|^2\Big)\,\mathrm{d}v^*, \tag{3.15}$$

where it is assumed that

$$g(0) = \mathrm{O}(1) \quad \text{in} \quad \epsilon_\phi. \tag{3.16}$$

We then define dimensionless quantities

$$\epsilon_\phi^2 = \frac{\alpha}{L^2 g(0)} \qquad \text{and} \qquad g^*(\phi^*) = \frac{g(\phi)}{g(0)}. \tag{3.17}$$

Noting that α has dimensions of energy per unit length, ϵ_ϕ in $(3.17)_1$ can be taken to represent the dimensionless interface length. The free-energy functional (3.7) then has the dimensionless form

$$E^*_{\phi^*} = \int_{\Omega^*} \frac{1}{\epsilon_\phi}\Big(g^*(\phi^*) + \frac{\epsilon_\phi^2}{2}|\nabla^*\phi^*|^2\Big)\,\mathrm{d}v^*. \tag{3.18}$$

To ascertain the asymptotic behavior of ϕ^* in a transition layer separating regions in which $\phi^* = -1$ and $\phi^* = 1$, one may perform a coordinate stretching by ϵ_ϕ^{-1} in the direction normal to the level surfaces of ϕ and introduce inner and outer expansions of ϕ. Details of the same are given below.

Inner and outer asymptotic expansion of ϕ and coordinate stretching

In regions away from the interface, ϕ and its derivatives may be approximated by the truncation of a formal power series, referred to as the outer expansion

$$\phi^*(\mathbf{x}) \approx \sum_i \epsilon_\phi^i\, \phi_i^*(\boldsymbol{x}). \tag{3.19}$$

To represent ϕ^* near S, we consider a local orthogonal coordinate system $r(\boldsymbol{x}), \boldsymbol{s}(\boldsymbol{x})$ in a neighborhood of S. Here r denotes the coordinate normal to the level surfaces of ϕ^* and $\boldsymbol{s} = (s_1, s_2)$, with (s_1, s_2) representing the arc lengths on S. A stretched coordinate is introduced such that

$$\rho(\boldsymbol{x}) = \frac{r(\boldsymbol{x})}{\epsilon_\phi}. \tag{3.20}$$

In a neighborhood of S, ϕ^* can be expressed either in terms of $\boldsymbol{x}$ or the $(r, \boldsymbol{s})$ coordinate system. Thus we have

$$\phi^*(\boldsymbol{x}) = \phi^*(r, \boldsymbol{s}) = \varphi^*(\rho, \boldsymbol{s}). \tag{3.21}$$

Here, φ^* is the inner approximation. Both φ^* and its derivatives are assumed to be approximated by the truncation of a formal power series, as given below

$$\varphi^* \approx \sum_i \epsilon_\phi^i \, \varphi_i^*(\rho, \boldsymbol{s}). \tag{3.22}$$

In the local orthogonal coordinate system, the gradient vector can be written in terms of its tangential and normal components as follows

$$\begin{aligned} \nabla(\,) &= (I - \mathbf{n} \otimes \mathbf{n})\nabla(\,) + (\mathbf{n} \otimes \mathbf{n})\nabla(\,) \\ &= \nabla_S(\,) + (\nabla(\,) \cdot \mathbf{n})\,\mathbf{n} \\ &= \nabla_S(\,) + \frac{\partial(\,)}{\partial r}\,\mathbf{n} \;=\; \nabla_S(\,) + \frac{1}{\epsilon_\phi}\frac{\partial(\,)}{\partial \rho}\,\mathbf{n} \end{aligned} \tag{3.23}$$

Using (3.23), the Euler–Lagrange equation arising from (3.18) to most significant order in ϵ_ϕ can be written as

$$g^{*\prime}(\varphi_0^*) - \frac{\partial^2 \varphi_0^*}{\partial \rho^2} = 0. \tag{3.24}$$

Integrating both sides of (3.24) with respect to φ_0^*, we obtain

$$\int g^{*\prime}(\varphi_0^*)\,\mathrm{d}\varphi_0^* = \int \frac{\partial^2 \varphi_0^*}{\partial \rho^2}\,\mathrm{d}\varphi_0^*. \tag{3.25}$$

Noting that $\varphi = \varphi(\rho)$, (3.25) can be recast as

$$\int g^{*\prime}(\varphi_0^*)\,\mathrm{d}\varphi_0^* = \int \frac{\partial^2 \varphi_0^*}{\partial \rho^2}\frac{\partial \varphi_0^*}{\partial \rho}\,\mathrm{d}\rho, \tag{3.26}$$

leading to the relation

$$g^*(\varphi_0^*) = \frac{1}{2}\left|\frac{\partial \varphi_0^*}{\partial \rho}\right|^2. \tag{3.27}$$

In concert with matching conditions and requirements on the outer expansion, φ_0^* must obey the far-field conditions

$$\lim_{\rho \to \pm\infty} \varphi_0^*(\rho, \cdot) = \lim_{r \to 0} \phi_0^*(r, \cdot) = \pm 1. \tag{3.28}$$

The assumed properties of g ensure that the boundary-value problem formed by (3.27) and (3.28) possesses a unique solution that increases monotonically from the value -1 at $\rho = -\infty$ to the value $+1$ at $\rho = +\infty$ and that it must be independent of the tangential coordinate $\boldsymbol{s}$.

In view of these properties, it follows from (3.27) that ϕ_0^* must satisfy

$$g^*(\phi_0^*) - \frac{\epsilon_\phi^2}{2}|\nabla^*\phi_0^*|^2 = \mathrm{O}(\epsilon_\phi). \tag{3.29}$$

Equivalently, by using (3.11)–(3.16), the above relation can be extended to the dimensional version of the energy density

$$g(\phi) - \frac{\alpha}{2}|\nabla\phi|^2 \approx 0. \tag{3.30}$$

Notice that (3.30) is satisfied trivially in regions where $\phi = \pm 1$. Within the layer, where $-1 < \phi < 1$, (3.30) states that the energy is, to most significant order in ϵ_ϕ, partitioned equally between contributions associated with the double-well potential and the gradient energy.

3.3 Diffuse-interface representation of the mean curvature

Within the transition layer Λ of any implicitly defined surface,

$$\mathbf{n} = \frac{\nabla\phi}{|\nabla\phi|} \tag{3.31}$$

represents the unit normal (oriented in the direction of increasing ϕ) and

$$H_\phi = \frac{1}{2}\,\nabla_S \cdot \mathbf{n} \tag{3.32}$$

represents the mean curvature (signed to be positive for a sphere) to the level surfaces of ϕ (Fried and Gurtin, 1996). For a diffuse interface representation of a surface, it

follows from (3.23) that

$$H_\phi = \frac{1}{2}\,\nabla_s \cdot \mathbf{n} = \frac{1}{2}\,\nabla \cdot \mathbf{n}. \tag{3.33}$$

Using (3.31) in (3.33), the mean curvature can be expressed in terms of the phase field ϕ as

$$H_\phi = \frac{1}{2}\,\nabla \cdot \Big(\frac{\nabla\phi}{|\nabla\phi|}\Big) = \frac{1}{2|\nabla\phi|}\Big(\Delta\phi - \frac{1}{2|\nabla\phi|^2}(\nabla\phi \cdot \nabla|\nabla\phi|^2)\Big). \tag{3.34}$$

As will be discussed in Chapter 4, the classical description of equilibrium shapes of vesicles (Canham, 1970; Helfrich, 1973; Evans, 1974) is obtained by minimizing the curvature energy of the vesicle surface. However, an energy functional based on (3.34) places no condition on the structure of the phase field ϕ. The present formulation presumes that the phase field satisfies, at least approximately, a relation of the form (3.30). In doing so, the formulation ensures that the structure of ϕ is retained (to most significant order in ϵ_ϕ) in the process of evolution towards shape equilibrium. On these lines, we derive the diffuse-interface representation for the mean curvature based on the expression for equi-partition of the phase-field energy (3.30).

A minor manipulation of the energy partition equation (3.30) as follows

$$\nabla\phi \cdot \nabla(g(\phi) - \frac{\alpha}{2}|\nabla\phi|^2) \approx 0 \tag{3.35}$$

leads to the relation

$$\frac{g'(\phi)}{\alpha} \approx \frac{1}{2|\nabla\phi|^2}(\nabla\phi \cdot \nabla|\nabla\phi|^2). \tag{3.36}$$

Substituting (3.36) in (3.34) yields the following useful approximation

$$H_\phi \approx \frac{1}{2|\nabla\phi|}\Big(\Delta\phi - \frac{g'(\phi)}{\alpha}\Big), \tag{3.37}$$

for the mean curvature of the level surfaces of ϕ. The rest of this work uses the above form for the mean curvature based on a specific choice for the double-well potential $g(\phi)$.

3.4 Volume enclosed by the vesicle

As illustrated in Figure 3.1, the phase field ϕ varies smoothly from -1 in the vesicle interior to 1 in the vesicle exterior while $\phi = 0$ represents the vesicle surface. Hence,

$$\lim_{\epsilon_\phi \to 0} \int_\Omega \phi \, \mathrm{d}v = V_{\text{out}} - V_{\text{in}} \tag{3.38}$$

where V_{in} is the volume enclosed by the vesicle and $V_{\text{out}} = V_\Omega - V_{\text{in}}$. Following (3.38), the approximate internal volume of the vesicle can be shown to be

$$V_{\text{in}} \approx \frac{1}{2} \int_\Omega (1 - \phi) \, \mathrm{d}v. \tag{3.39}$$

Denoting the dimensionless volume by

$$V_{\text{in}}^* = \frac{V_{\text{in}}}{L^3}, \tag{3.40}$$

the dimensionless version of (3.39) has the form

$$V_{\text{in}}^* \approx \frac{1}{2} \int_{\Omega^*} (1 - \phi^*) \, \mathrm{d}v^*. \tag{3.41}$$

3.5 Surface area of the vesicle

Suppose that Ω is decomposed into subregions Ω_{in} and Ω_{out} separated by a transition layer Λ. Then, in view of the properties of the double-well potential, the energy functional (3.7) obeys

$$\int_\Omega \left(g(\phi) + \frac{\alpha}{2} |\nabla \phi|^2 \right) \mathrm{d}v = \int_\Lambda \left(g(\phi) + \frac{\alpha}{2} |\nabla \phi|^2 \right) \mathrm{d}v. \tag{3.42}$$

On introducing the dimensionless counterpart,

$$\Lambda^* = \{\boldsymbol{x}^* \in \Omega^* : L\boldsymbol{x}^* \in \Lambda\}, \tag{3.43}$$

of Λ, (3.18) implies that the dimensionless form of (3.42) is

$$\int\limits_{\Omega^*} \frac{1}{\epsilon_\phi}\Big(g^*(\phi^*) + \frac{\epsilon_\phi^2}{2}|\nabla^*\phi^*|^2\Big)\,\mathrm{d}v^* = \int\limits_{\Lambda^*} \frac{1}{\epsilon_\phi}\Big(g^*(\phi^*) + \frac{\epsilon_\phi^2}{2}|\nabla^*\phi^*|^2\Big)\,\mathrm{d}v^*. \tag{3.44}$$

Within the transition layer Λ^* we consider the inner expansion φ^* of ϕ^*. Using the equi-partition relation (3.27) for the leading order term φ_0^*, (3.44) can be approximated as

$$\int\limits_{\Lambda^*} \frac{1}{\epsilon_\phi}\Big(g^*(\phi^*) + \frac{\epsilon_\phi^2}{2}|\nabla^*\phi^*|^2\Big)\,\mathrm{d}v^* \approx \int\limits_{S^*}\int\limits_{-\infty}^{+\infty} \left|\frac{\partial\varphi_0^*}{\partial\rho}\right|^2 \mathrm{d}\rho\,\mathrm{d}a^*. \tag{3.45}$$

Employing a change of variables by noting that $\varphi_0^* = \varphi_0^*(\rho)$ and a corresponding change in the limits of integration by noting that $\varphi^* \to \pm 1$ as $\rho \to \pm\infty$, (3.45) can be recast as

$$\int\limits_{\Lambda^*} \frac{1}{\epsilon_\phi}\Big(g^*(\phi^*) + \frac{\epsilon_\phi^2}{2}|\nabla^*\phi^*|^2\Big)\,\mathrm{d}v^* \approx \int\limits_{S^*}\int\limits_{-1}^{+1} \left|\frac{\partial\varphi_0^*}{\partial\rho}\right| \mathrm{d}\varphi_0^*\,\mathrm{d}a^* \tag{3.46}$$

$$= \int\limits_{S^*}\int\limits_{-1}^{+1} \sqrt{2g^*(\varphi_0^*)}\,\mathrm{d}\varphi_0^*\,\mathrm{d}a^*. \tag{3.47}$$

Equations (3.44) and (3.47) imply that the dimensionless surface area is well approximated by

$$A^* = \int\limits_{S^*} \mathrm{d}a^* \approx \frac{1}{\varsigma^*}\int\limits_{\Omega^*} \frac{1}{\epsilon_\phi}\Big(g^*(\phi^*) + \frac{\epsilon_\phi^2}{2}|\nabla^*\phi^*|^2\Big)\,\mathrm{d}v^* \tag{3.48}$$

where

$$\varsigma^* = \int\limits_{-1}^{+1} \sqrt{2g^*(\varphi_0^*)}\,\mathrm{d}\varphi_0^*. \tag{3.49}$$

The surface area of an implicitly defined surface can be obtained from (3.1) by setting $f = 1$ (and consequently $\tilde{f} = 1$) as

$$A = \int_S \mathrm{d}a = \int_\Omega \delta_S \, \mathrm{d}v \tag{3.50}$$

having an equivalent dimensionless form

$$A^* = \int_{S^*} \mathrm{d}a^* = \int_{\Omega^*} \delta_S^* \, \mathrm{d}v^*. \tag{3.51}$$

Comparing (3.51) with (3.48), we note that (3.48) implies an approximate delta function of the form

$$\delta_S^* \approx \frac{1}{\varsigma^*}\Big(\frac{g^*(\phi^*)}{\epsilon_\phi} + \frac{\epsilon_\phi}{2}|\nabla^*\phi^*|^2\Big). \tag{3.52}$$

The form of δ_S^* for a specific choice of the double-well potential is discussed in Chapter 4.

Phase-field models can be obtained either by completely recasting the energy functional in terms of the phase field and subsequently deriving the Euler–Lagrange equations or by directly modifying the surface form of the governing equation (Gonzalez Cinca et al., 2003). In the present work, the former approach is used to derive the diffuse-interface form of the membrane shape equation and the latter approach is used to arrive at the diffuse-interface form of the equation describing species transport on the vesicle surface.

The mechanical and chemical contributions to the vesicle energetics are re-cast using the phase field ϕ. The penalty energy associated with the geometric constraints on internal volume and surface area of the vesicle is similarly obtained. Shape equilibrium is then achieved by requiring the first variation $\delta E/\delta\phi$ of the total energy to vanish.

The equation governing the lateral organization of the phases on the vesicle resembles the Cahn–Hilliard equation for binary mixtures. Details underlying the conversion of this equation from surface form to phase-field form are provided in Section 4.3.1.

4

Continuum Modeling of Vesicles

4.1 Introduction

In this Chapter, we discuss the diffuse-interface form of the energetic contributions describing a bilayer vesicle and arrive at the governing equations of species transport and shape change.

4.2 Energetics

Experimental evidence (Baumgart et al., 2005) suggests that phase separation affects the shape of the vesicle. While the coupling between mechanics and chemistry is captured to a certain extent by considering concentration-dependent mechanical properties such as flexural rigidity and spontaneous curvature, a comprehensive description of the interaction is provided by the energetics. The net energy of the vesicle is taken to be a sum of mechanical and chemical contributions, both of which are discussed in this Section. During shape evolution, coupling manifests itself through the effect of line tension which arises from the chemical contribution to the energy. During species transport, the effect of coupling is seen through mechanical energy

that drives curvature-dependent domain sorting.

4.2.1 Chemical energy

The present work focuses on the evolution of microdomains in GUVs composed of cholesterol and two lipid species. It is assumed that both lipid species dimerize with cholesterol, mainly resulting in a binary mixture of two phases.

The GUV is identified with an oriented surface S bounding a region R. On writing ρ^γ for the density of species $\gamma = \alpha, \beta$,

$$c_S = \frac{\rho^\alpha}{\rho^\alpha + \rho^\beta} \quad \text{and} \quad 1 - c_S = \frac{\rho^\beta}{\rho^\alpha + \rho^\beta} \tag{4.1}$$

represent the area fractions of species α and β on S. We also refer to the area fraction as concentration. The purely chemical free-energy of the GUV is taken to be of Cahn–Hilliard type (Cahn and Hilliard, 1958)

$$E_\mathrm{c} = \int_S \left(f(c_S) + \frac{\lambda}{2} \left| \nabla_S c_S \right|^2 \right) \mathrm{d}a, \tag{4.2}$$

where f is a double-well potential, λ is a constant with dimensions of energy and ∇_s is the gradient operator on S. In the integrand of (4.2), f represents the demixing energy, while the gradient term represents the interfacial energy, which is also referred to as the mixing energy. Any minimizer of the chemical free-energy E_c is thus determined from a balance between the local demixing and the non-local mixing contributions (Gary S. Ayton and Voth, 2005). This balance allows for the existence of a two-phase equilibria, where regions occupied by the two different phases are separated by smooth transition layers.

To non-dimensionalize (4.2), we introduce dimensionless variables

$$\begin{aligned} c_s^*(\boldsymbol{s}^*) &= c_s(\boldsymbol{s}), \qquad & f^*(c_s^*) &= \frac{f(c_s)}{\nu}, \\ \epsilon_c^2 &= \frac{\lambda}{\nu L^2}, & E_{\mathrm{c}}^* &= \frac{E_{\mathrm{c}}}{\nu\, L^2}, \end{aligned} \tag{4.3}$$

where ν is a characteristic measure of energy per unit area and is given by the height of the barrier separating the minima of the double-well potential f entering (4.2). On employing (4.3), the dimensionless form of the free-energy functional (4.2) is given by

$$E_{\mathrm{c}}^* = \int\limits_{S^*} \left(f^*(c_S^*) + \frac{\epsilon_c^2}{2} \left| \nabla_S^* c_S^* \right|^2 \right) \mathrm{d}a^*, \tag{4.4}$$

To obtain a diffuse-interface form of the functional (4.4), we proceed as in the derivation of (3.48) where a surface integral is approximated as an equivalent volume integral. The dimensionless diffuse-interface form of the chemical energy (4.2) can then be written as

$$E_{\mathrm{c}}^* \approx \int\limits_{\Omega^*} \left(f^*(c^*) + \frac{\epsilon_c^2}{2} \left| (\boldsymbol{1} - \mathbf{n} \otimes \mathbf{n}) \nabla^* c^* \right|^2 \right) \delta_S^* \, \mathrm{d}v^*, \tag{4.5}$$

where c^* is defined in a neighborhood of S^* by extending c_S^* off the surface and ϵ_c can be considered as the dimensionless thickness of the interface separating the phases. $\mathbf{n}$ represents the unit normal to the level surfaces of ϕ^* and is given by (3.31). The operator $(\boldsymbol{1} - \mathbf{n} \otimes \mathbf{n})$ projects the Euclidean gradient $\nabla^* c^*$ onto the level surfaces of the phase field ϕ^*. The approximate delta function δ_S^* facilitates casting the surface integral (4.2) as an equivalent volume integral in diffuse-interface form.

Realistic energy-density functions based on the theory of fluid mixtures have been studied for binary mixtures on vesicles (Komura et al., 2004). In the present work, we use a double-well potential based on the Flory–Huggins theory of binary

polymer mixtures (Flory, 1942; Huggins, 1942). A non-dimensional version of the Flory–Huggins potential is given by

$$f^*_{\text{F–H}}(c^*) = c^* \ln c^* + (1 - c^*) \ln(1 - c^*) + \chi c^*(1 - c^*), \tag{4.6}$$

where $\chi > 2$ is the interaction parameter. The first pair of terms of the potential (4.6) is purely entropic and is referred to as the entropy of mixing while the remaining term is enthalpic and is also referred to as the enthalpy of mixing.

4.2.2 Mechanical energy

The mechanical free-energy of the GUV is taken to be characterized by the generalized Canham–Helfrich–Evans curvature energy (Canham, 1970; Helfrich, 1973; Evans, 1974) given by

$$E_{\text{m}} = \frac{1}{2} \int_S \kappa(c_S) \left(H - H_{\text{sp}}(c_S)\right)^2 \, \mathrm{d}a, \tag{4.7}$$

where κ and H_{sp} are the concentration-dependent flexural rigidity and spontaneous curvature. It is commonly acknowledged that the Gaussian curvature energy influences the details near the phase boundaries in heterogeneous vesicles and also during topological changes in the vesicle shape (Jülicher and Lipowsky, 1996; Baumgart et al., 2005). Nevertheless, for simplicity, Gaussian curvature energy is neglected in this study. The role of this energetic contribution will be addressed in future work.

To non-dimensionalize (4.7), we introduce dimensionless variables

$$\begin{aligned} H^* &= LH, \qquad H^*_{\text{sp}} = LH_{\text{sp}}, \\ \kappa^* &= \frac{\kappa}{\lambda}, \qquad E^*_{\text{m}} = \frac{E_{\text{m}}}{\nu L^2}, \end{aligned} \tag{4.8}$$

where λ and ν are defined in equations (4.2) and (4.3) respectively. Noting that

$\nu = \lambda/\epsilon_c^2 L^2$ from (4.3), the dimensionless form of the functional (4.7) is given by

$$E_{\mathrm{m}}^* = \frac{\epsilon_c^2}{2} \int\limits_{S^*} \kappa^*(c_S^*) \left(H^* - H_{\mathrm{sp}}^*(c_S^*)\right)^2 \, \mathrm{d}a^*, \tag{4.9}$$

Notice that the curvature energy (4.9) is scaled by the factor ϵ_c^2. The scaling term arises as a consequence of rendering the energy per unit area dimensionless.

We then introduce the dimensionless diffuse-interface form of the mean curvature based on (3.37) as

$$H_{\phi^*}^* = L H_\phi \approx \frac{1}{2|\nabla^* \phi^*|} \Big(\Delta^* \phi^* - \frac{g^{*\prime}(\phi^*)}{\epsilon_\phi^2} \Big). \tag{4.10}$$

Proceeding as in the derivation of (3.48) where a surface integral is approximated as an equivalent volume integral, the dimensionless diffuse-interface form of the curvature energy (4.9) is obtained as

$$E_{\mathrm{m}}^* \approx \frac{\epsilon_c^2}{2} \int\limits_{\Omega^*} \kappa^*(c^*) \left(H_{\phi^*}^* - H_{\mathrm{sp}}^*(c^*)\right)^2 \delta_S^* \, \mathrm{d}v^*, \tag{4.11}$$

where c^* is now defined in a neighborhood of S^*.

Following (4.5) and (4.11), the diffuse-interface form of the net free-energy of the GUV is given as

$$E_{\mathrm{net}}^* = E_{\mathrm{c}}^* + E_{\mathrm{m}}^* \tag{4.12}$$

4.2.3 Geometric constraints

The number of lipid molecules in a bi-layer is observed to be nearly constant over time scales of experimental relevance (that is, for up to a few hours) (Seifert, 1997). Moreover, even the number of lipid molecules in each monolayer is considered practically constant since the interchange of molecules between the monolayers is very slow (Seifert, 1997). The above observations lead to a local lateral incompressibility

condition for the lipid bi-layer (Evans and Skalak, 1980). Within the phase-field framework and for vesicles under flow, treatment of the local constraint using a Lagrange-multiplier field is discussed by Jamet and Misbah (2007) and Biben et al. (2005). In the present study, however, a global area conservation condition is used as a constraint to model shape equilibrium of isolated vesicles.

Since the bending resistance of vesicles is too weak to sustain osmotic pressure, the volume of a vesicle is determined by the concentration distribution of osmotically active molecules and the requirement that the osmotic pressure vanish (Helfrich, 1973). Furthermore, vesicles are permeable to water but, during the time scales under consideration here, are impermeable to large ions (Seifert, 1997). Hence, the volume enclosed by a vesicle can be considered to be fixed.

The global geometric constraints of fixed enclosed volume and surface area can be represented in equivalent diffuse-interface forms. The dimensionless versions of the enclosed volume and surface area are given by (3.41) and (3.48) respectively.

Denoting the ratio of the enclosed volume V_i to the initial enclosed volume V_0 by

$$V^* = \frac{V_\mathrm{i}}{V_0} \tag{4.13}$$

and the ratio of the surface area A to the initial surface area A_0 by

$$A^* = \frac{A}{A_0}, \tag{4.14}$$

the penalty energy E^*_gc arising from the constraints on internal volume and surface area is given by

$$E^*_\mathrm{gc} = \frac{\alpha_v}{2}\left(V^* - 1\right)^2 + \frac{\alpha_a}{2}\left(A^* - 1\right)^2, \tag{4.15}$$

where α_v and α_a are penalty parameters associated, respectively, with the constraints on volume and surface area. In view of these constraints, the functional of interest

is

$$E^* = E^*_{\text{net}} + E^*_{\text{gc}}. \tag{4.16}$$

4.3 Governing equations

The diffuse-interface form of the governing equations is presented in this section. The equation governing species transport on the vesicle follows from an argument analogous to that leading to the Cahn–Hilliard equation for binary mixtures (Cahn and Hilliard, 1958). The shape equation arises on requiring the first variation of the functional E to vanish.

4.3.1 Species transport

The equation governing species transport on the GUV surface is derived in the manner used to arrive at the Cahn–Hilliard equation for binary mixtures (Cahn and Hilliard, 1958). The net energy of the system is considered to be composed of both mechanical and chemical contributions. Consider a binary mixture of lipid species α and β. The first variation of the net free-energy with respect to c_S, where c_S is the area fraction defined in (4.1), represents the chemical potential of species α with respect to species β. Considering all quantities such as energy, concentration, and chemical potential to be defined on S, the equation of species conservation on S, and the corresponding chemical potential μ_S are

$$\frac{\partial c_S}{\partial t} = \nabla_S \cdot \left(M(c_S)\nabla_S \mu_S\right), \tag{4.17a}$$

$$\mu_S = \frac{\delta E_{\text{c}}}{\delta c_S} + \frac{\delta E_{\text{m}}}{\delta c_S}, \tag{4.17b}$$

where $\nabla_S\cdot$ is the surface divergence and $M(c_S)$ is the concentration dependent species mobility. In the present work, we restrict the study to a constant species mobility M for the sake of simplicity. In (4.17), E_{c} and E_{m} are given by (4.2) and (4.7)

respectively. Introducing a characteristic time scale T and defining

$$c^*(\boldsymbol{s}^*, t^*) = c(\boldsymbol{s}, t), \tag{4.18}$$

we note that

$$\frac{\partial c(\boldsymbol{s}, t)}{\partial t} = \frac{1}{T}\frac{\partial c^*(\boldsymbol{s}^*, t^*)}{\partial t^*}. \tag{4.19}$$

Further, introducing a dimensionless mobility and chemical potential

$$M^* = \frac{\nu M T}{L^2} \qquad \text{and} \qquad \mu_S^* = \frac{\mu_S}{\nu}, \tag{4.20}$$

the dimensionless version of the surface species transport equation (4.17) takes the form

$$\frac{\partial c^*(\boldsymbol{s}^*, t^*)}{\partial t^*} = \nabla_S \cdot^* (M^* \nabla_S \mu_S^*) \tag{4.21a}$$

$$\mu_S^* = \frac{\delta E_{\mathrm{c}}^*}{\delta c_S^*} + \frac{\delta E_{\mathrm{m}}^*}{\delta c_S^*} \tag{4.21b}$$

where E_{c}^* and E_{m}^* are given by (4.4) and (4.9), respectively.

Whereas the variation $\delta E_{\mathrm{c}}^*/\delta c_S^*$ can be recognized as a contribution to the chemical potential that drives phase separation (i.e., spinodal decomposition and coarsening), the variation $\delta E_{\mathrm{m}}^*/\delta c_S^*$ can be recognized as a contribution to the chemical potential that drives curvature-dependent domain sorting.

4.3.2 Shape equilibrium

The equation of shape equilibrium is obtained by requiring the first variation of the functional E to vanish.

$$\frac{\delta E^*}{\delta \phi^*} = \frac{\delta E_{\mathrm{c}}^*}{\delta \phi^*} + \frac{\delta E_{\mathrm{m}}^*}{\delta \phi^*} + \frac{\delta E_{\mathrm{gc}}^*}{\delta \phi^*} = 0 \tag{4.22}$$

The variations $\delta E_{\mathrm{c}}^*/\delta \phi^*$ and $\delta E_{\mathrm{m}}^*/\delta \phi^*$ govern shape changes in response to energetic penalties associated with line tension and curvature, respectively.

A representation of the approximate delta function δ_s (3.52) and a diffuse-interface approximation of the mean curvature H_ϕ (4.10) are now employed to obtain the diffuse-interface form of the curvature energy. Further, specific forms for the governing equations of shape equilibrium (4.22) and species transport (4.21) are provided. All the governing equations are expressed in dimensionless form. However, asterisks depicting dimensionless quantities are omitted for the sake of clarity.

4.4 Expressions for an approximate delta function and mean curvature

To describe the phase-field energy in (3.18), we use a quartic double-well potential of the form $g(\phi) = (1-\phi^2)^2/4$. For this particular choice of $g(\phi)$, the approximate delta function (3.52) simplifies to

$$\delta_s \approx \frac{3\sqrt{2}}{4}\Big(\frac{(1-\phi^2)^2}{4\,\epsilon_\phi} + \frac{\epsilon_\phi}{2}\,|\nabla\phi|^2\Big). \tag{4.23}$$

The similarity of (4.23) to the dimensionless energy density (3.18) associated with the phase field can be noted. Equipartition of the energy (Fried, 2006), as shown in (3.29), results in equivalent expressions for δ_s:

$$\delta_s \approx \frac{3\sqrt{2}}{4}\epsilon_\phi\,|\nabla\phi|^2\,, \tag{4.24a}$$

$$\approx \frac{3\sqrt{2}}{8\epsilon_\phi}(1-\phi^2)^2. \tag{4.24b}$$

Using the same quartic potential in the expression for the dimensionless mean curvature (4.10) yields

$$H_\phi \approx \frac{1}{2\,|\nabla\phi|}\Big(\Delta\phi + \frac{\phi(1-\phi^2)}{\epsilon_\phi^2}\Big). \tag{4.25}$$

4.5 Expressions for line tension energy and curvature energy

The line tension energy is associated with the interfaces separating the phases distributed on the vesicle surface. Employing the expression for the approximate delta function (4.23) in (4.5), the diffuse-interface approximation of the dimensionless line tension energy (4.5) is given by

$$E_{\mathrm{c}} \approx \frac{3\sqrt{2}}{4} \int\limits_{\Omega} \Big(f(c) + \frac{\epsilon_c^2}{2} \left| (\boldsymbol{1} - \mathbf{n} \otimes \mathbf{n}) \nabla c \right|^2 \Big) \Big(\frac{(1-\phi^2)^2}{4\,\epsilon_\phi} + \frac{\epsilon_\phi}{2} \left| \nabla \phi \right|^2 \Big) \, \mathrm{d}v. \tag{4.26}$$

Similarly, using (4.24) and (4.25) in (4.11), the diffuse-interface approximation of the dimensionless curvature energy (4.11) can be expressed as

$$E_{\mathrm{m}} \approx \Big(\frac{3\sqrt{2}}{16} \Big) \frac{\epsilon_c^2\, \epsilon_\phi}{2} \int\limits_{\Omega} \kappa(c) \Big(\Delta\phi + \frac{\phi\,(1-\phi^2)}{\epsilon_\phi^2} - \frac{\sqrt{2}}{\epsilon_\phi} \left(1-\phi^2\right) H_{\mathrm{sp}}(c) \Big)^2 \mathrm{d}v. \tag{4.27}$$

It can be noted that the particular choice (4.24a) for the approximate delta function helps alleviate numerical singularities in E_{m} that can result from the factor of $\left|\nabla\phi\right|^{-1}$ in the diffuse-interface approximation (4.25) of the mean curvature.

4.6 Specialization of the governing equations

The governing equations for species transport and shape equilibrium are obtained using different approaches. As discussed in Section 4.3.1, the chemical potential μ in the governing equation for species transport involves variational derivatives of the associated energy functional with respect to the surface concentration c_s. Hence, it is natural to begin with obtaining the surface form of the equation of species transport. The diffuse-interface form is then approximated from the surface form. In contrast, the equation of shape equilibrium (4.22) is evaluated by requiring the first variation of the associated energy with respect to ϕ (the order parameter representing shape)

to vanish. Hence, a diffuse-interface form of the associated energy functional is employed to arrive at the equation of shape equilibrium.

4.6.1 Equation of species transport

Following (4.21), the equation of species transport on a surface is given by

$$\frac{\partial c_S}{\partial t} = \nabla_S \cdot (M \nabla_S \mu_S), \tag{4.28a}$$

$$\mu_S = \epsilon_c^2 \left(\frac{1}{2} \kappa'(c_S)(H - H_{\rm sp}(c_S))^2 - \kappa(c_S)(H - H_{\rm sp}(c_S)) H'_{\rm sp}(c_S) \right) + f'_{\rm F\text{–}H}(c_S) - \epsilon_c^2 \, \Delta_S c_S, \tag{4.28b}$$

where Δ_S represents the Laplacian operator on a surface.

Noting that the Euclidean counterparts of the surface gradient and surface Laplacian operators are given as (Greer et al., 2006)

$$\nabla_S(\,) = (\boldsymbol{1} - \mathbf{n} \otimes \mathbf{n}) \nabla(\,) \quad \text{and} \quad \Delta_S(\,) = \nabla \cdot ((\boldsymbol{1} - \mathbf{n} \otimes \mathbf{n}) \nabla(\,)), \tag{4.29}$$

the diffuse-interface form of (4.28) can then be approximated as

$$\frac{\partial c}{\partial t} = \nabla \cdot (M(\boldsymbol{1} - \mathbf{n} \otimes \mathbf{n}) \nabla \mu), \tag{4.30a}$$

$$\mu \approx \epsilon_c^2 \left(\frac{1}{2} \kappa'(c)(H_\phi - H_{\rm sp}(c))^2 - \kappa(c)(H_\phi - H_{\rm sp}(c)) H'_{\rm sp}(c) \right) + f'_{\rm F\text{–}H}(c) - \epsilon_c^2 \, \nabla \cdot \big((\boldsymbol{1} - \mathbf{n} \otimes \mathbf{n}) \nabla c \big), \tag{4.30b}$$

where H_ϕ and c represent equivalent diffuse-interface forms of H and c_s and are thus defined in a neighborhood of S.

REMARKS:

(a) Restriction of the species transport equation

It can be noted based on (4.30), that the equation of species transport is also defined far away from S. This can lead to a conflict of the dynamics in regions where

equations extending from opposite sides of the surface S intersect. To avoid this complication, it is recommended to multiply both sides of (4.30a) by δ_S. The function smoothly restricts the equation of species transport to a band encompassing the surface.

(b) Zero-flux constraint in a neighborhood of the surface

Notice that solving (4.30) in a neighborhood of S is equivalent to solving (4.17) on multiple level sets of ϕ. As Greer et al. (Greer et al., 2006; Greer, 2006) remark, to minimize variations in the solution off the zero level-set of ϕ, it is desirable to extend the relevant quantity (i.e., the concentration) in a manner such that the extension is constant normal to S. However, the late-time characteristic of the numerical solution does not necessarily retain this property. To overcome this difficulty, consider a situation where

$$\nabla c \cdot \mathbf{n} = 0 \tag{4.31}$$

holds pointwise in a neighborhood of S, thereby preventing information transfer between level sets. The constraint (4.31) ensures that solving the diffuse-interface version of the species transport equation is equivalent to simultaneously solving it on multiple level sets of ϕ, while the solution on each level set is independent of the solutions on all other level sets at all times.

In the present work, the zero flux constraint is weakly imposed using the penalty method. The corresponding penalty energy is

$$E_{\mathrm{p}} = \frac{\alpha_m}{2} \int_{\Omega} (\nabla c \cdot \mathbf{n})^2 \delta_S \, \mathrm{d}v, \tag{4.32}$$

where α_m is the penalty parameter. The approximate delta function δ_S smoothly restricts the constraint condition to a neighborhood of the surface. The first variation with respect to c of the penalty energy (4.32) is directly added to the evolution

equation (4.30a).

(c) A note on boundary conditions

While evolution equations on a surface do not require boundary conditions to be imposed, equivalent diffuse-interface forms operate on bounded domains defined by a band encompassing the surface. This would necessitate imposing boundary conditions on the boundaries of the band. However, the zero-flux constraint (4.31) ensures that evolution of the solution on each level surface is independent of the solutions on all other level surfaces at any time. Noting that an evolution equation on a closed surface/independent level surface does not require boundary conditions to be imposed, no additional conditions are necessary to augment the evolution equation (4.30) in phase-field form.

4.6.2 Equation of shape equilibrium

On employing (4.27) for E_{m}, and (4.23) for the approximate delta function δ_s, each of the terms in the shape equation (4.22) can be evaluated as

$$\frac{\delta E_{\mathrm{c}}}{\delta\phi} = \frac{3\sqrt{2}}{4}\left(\frac{1}{\epsilon_\phi}\psi(c)g'(\phi) - \epsilon_\phi\Big(\psi(c)\Delta\phi + \nabla\phi\cdot\nabla\psi(c)\Big)\right), \tag{4.33a}$$

$$\frac{\delta E_{\mathrm{m}}}{\delta\phi} = \frac{3\sqrt{2}\epsilon_c^2\epsilon_\phi}{16}\left(\Delta\big(\kappa(c)F(\phi)\big) - \frac{1}{\epsilon_\phi^2}\kappa(c)F(\phi)g''(\phi) + \frac{2\sqrt{2}}{\epsilon_\phi}\kappa(c)H_{\mathrm{sp}}(c)F(\phi)\phi\right), \tag{4.33b}$$

$$\frac{\delta E_{\mathrm{gc}}}{\delta\phi} = -\frac{\alpha_v}{2V_0}\left(V_R - 1\right) + \frac{3\sqrt{2}}{4\epsilon_\phi}\frac{\alpha_a}{A_0}\left(A_R - 1\right)\left(g'(\phi) - {\epsilon_\phi}^2\Delta\phi\right), \tag{4.33c}$$

where

$$g(\phi) = \frac{1}{4}(1-\phi^2)^2,$$

$$F(\phi) = \Delta\phi + \frac{\phi\,(1-\phi^2)}{\epsilon_\phi^2} - \frac{\sqrt{2}}{\epsilon_\phi}\left(1-\phi^2\right) H_{\mathrm{sp}}(c),$$

$$\psi(c) = f_{\text{F–H}}(c) + \frac{{\epsilon_c}^2}{2}\left|(\boldsymbol{1} - \mathbf{n}\otimes\mathbf{n})\nabla c\right|^2.$$

The quantities V_R and A_R represent the dimensionless internal volume and surface area of the vesicle and are given by (4.13) and (4.14), respectively. To obtain (4.33a), the zero-flux condition (4.31) is assumed to hold in a neighborhood of the surface. In view of (4.33), the shape equation turns out to be fourth-order and nonlinear and can be numerically challenging to solve. In the present work, shape equilibrium is achieved by relaxing (4.22) to

$$\frac{\partial\phi}{\partial\tau} = -\frac{\delta E}{\delta\phi} \tag{4.34}$$

and approximating the solution to the steady state of (4.34), i.e. $\partial\phi/\partial\tau \approx 0$. In (4.34), τ represents pseudo (i.e., non-physical) time.

5

Conforming Finite Elements with a B-spline Basis

5.1 Overview

Smooth functions such as B-splines and rational B-splines are becoming increasingly popular for use in finite-element approximations to solutions of partial differential equations. This is due in part to their ability to provide exact geometric representations of curved domains (as with the isogeometric concept (Hughes et al., 2005)) but also to an increasing emphasis on fourth-order systems. The governing equations of shape equilibrium of vesicles and species transport on the vesicle surface are examples of the latter. Construction of conforming finite elements for fourth-order problems requires the solution and weighting spaces to be in H^2. It can be shown (Braess, 2007) that piece-wise smooth functions that are globally C^1 continuous are necessarily functions in H^2. However, classical finite elements employ Lagrangian basis functions that are piece-wise smooth but only possess global C^0 continuity. This drawback is generally overcome by several techniques including the use of mixed methods, Discontinuous Galerkin (DG) and Continuous/Discontinuous Galerkin (CDG) methods. While mixed methods and DG methods increase the de-

grees of freedom for the problem, the CDG method, which uses C^0 basis functions and weakly enforces continuity of the derivatives across element boundaries (Engel et al., 2002), adds DG operators to the system. Recent studies (Gómez et al., 2008) have focused on using the concept of isogeometric analysis to solve the Cahn-Hilliard equation. Essentially, these techniques use a NURBS or spline basis to capture the geometry accurately while employing the same functions as a basis for the solution space. The functions provide higher-order continuity globally and do not introduce additional degrees of freedom to the problem. In this work, a conforming finite element basis for the fourth-order equations resulting from the chemo-mechanical model for vesicles is constructed with B-splines.

5.2 B-spline basis functions

A brief account of the construction of B-Spline basis functions in one dimension is given below. Extension to multiple dimensions is straightforward with the use of tensor product splines. A more detailed treatment of the subject can be found in Piegl and Tiller (1997).

Consider a knot vector Ξ, where,

$$\Xi \;=\; \{\xi_1, \xi_2, \ldots, \xi_{n+p+1}\} \tag{5.1}$$

with n denoting the number of control points and p, the degree of the spline. B-spline basis functions are defined recursively starting with piecewise constants (degree p=0):

$$N_{I,0}\left(\xi\right) \;=\; \begin{cases} 1 & \text{if } \xi_I \leqslant \xi < \xi_{I+1} \\ 0 & \text{otherwise} \end{cases} \tag{5.2}$$

For $p \geqslant 1$:

$$N_{I,p}\left(\xi\right) \;=\; \frac{\xi - \xi_I}{\xi_{I+p} - \xi_I} N_{I,p-1}\left(\xi\right) \;+\; \frac{\xi_{I+p+1} - \xi}{\xi_{I+p+1} - \xi_{I+1}} N_{I+1,p-1}\left(\xi\right) \tag{5.3}$$

Figure 5.1(a) illustrates five cubic B-spline basis functions over a uniform knot vector in one dimension. An example of a bicubic spline is shown in Figure 5.1(b). It is generated using a tensor product of the 1-D spline highlighted in Figure 5.1(a).

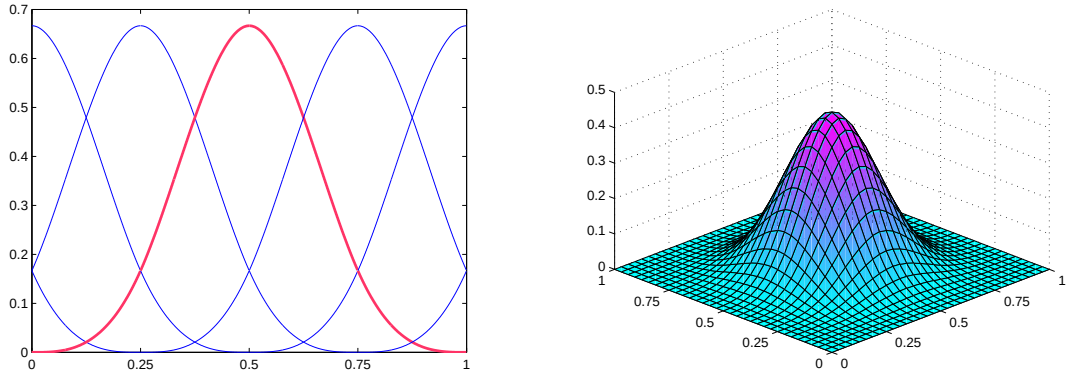

(a) 1D cubic spline basis

(b) Bicubic spline

FIGURE 5.1: C^2 continuous cubic spline basis functions resulting from a uniform knot vector.

5.2.1 Finite element basis with B-splines

Cubic B-spline basis functions constructed on a uniform grid are used as a finite element basis in this study. Each B-spline function is identified by the point having the lowest knot coordinate in its support. In two dimensions, this translates to being the lower left corner of the spline support, as shown in Figure 5.2(a). With this construction, relevant bicubic B-splines for a general physical domain are shown in Figure 5.2(b). The circular markers represent the lower left corner of each bicubic spline whose support extends into the physical domain.

The union of the support of all relevant splines is referred to as the computational domain, depicted by the grey shaded region in Figure 5.2(b). Knot spans subdivide the computational domain into 'elements' with characteristic side-lengths h.

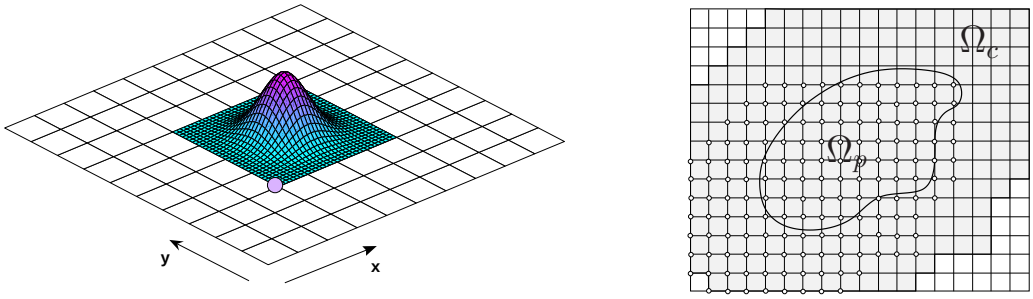

(a) (b)

FIGURE 5.2: (a) Identification node for a bi-cubic spline basis function and (b) Computational domain (in grey) for the given geometry.

5.2.2 Dirichlet boundary conditions

While a finite element framework with a B-spline basis lends itself well for the treatment of higher-order partial differential equations, a number of challenges to working with B-splines remain. They are most easily constructed over rectilinear domains, and their use with arbitrarily-shaped domains often involves either a mapping (as with isogeometrics) or 'fictitious-domain' type of approaches (see Höllig (2012)). Perhaps more importantly, these functions tend to be non-interpolatory, and imposing even simple boundary conditions can be a challenge.

One approach is a result of knot-repetition but is limited in application. A spline basis of order p has $p-1$ continuous derivatives along element edges and is infinitely differentiable within an element (Hughes et al., 2005). The basis can be rendered interpolatory at any knot when the knot multiplicity is p (obtained by repeating the knots at the same knot location) (Hughes et al., 2005). However, on account of splines being constructed on rectilinear domains, this technique does not allow the basis to be made interpolatory at boundaries of arbitrarily shaped domains.

Another approach is to modify the splines in the vicinity of the boundary through a product with a weight function, such that the resulting basis functions and the

appropriate derivatives vanish at the surface (Höllig, 2012). While this approach has proven successful, an unfortunate consequence is that it raises the order of the basis functions, requiring additional quadrature.

Dirichlet-type boundary conditions can be imposed weakly using either a Lagrange multiplier or a penalty approach. An alternative is the use of Nitsche's method (Nitsche, 1971). Nitsche's method has recently emerged as an attractive alternative for weakly imposing Dirichlet boundary conditions in meshfree (Fernández-Méndez and Huerta (2004)) and embedded finite-element methods (Hansbo and Hansbo (2002); Dolbow and Harari (2009)). While the approach is sometimes referred to as a variationally consistent penalty method, it is more constructive to view it as a stabilized method. Indeed, one means to identify the stabilization parameter is to seek the minimum value which guarantees coercivity of the bilinear form. This approach was suggested in the context of meshfree methods and second-order problems by Griebel and Schweitzer (2003), who proposed the solution of an eigenvalue problem to identify the stabilization parameter. This basic idea can be employed for fourth-order problems in which Dirichlet boundary conditions involve both the primary function and its derivative.

It bears emphasis that this approach is designed to work equally well when the grid used to build the splines conforms to the physical boundary of interest as well as the more general case when it does not. Since the B-Splines are not interpolants, there is no overriding need for the grid to conform to the boundary. Formulations that force such conformity do so mostly to facilitate integration over the 'elements' that are the knot-spans associated with the splines (Hughes et al., 2005). Partial elements that result with non-conforming grids can be addressed by simply modifying the quadrature scheme for integration.

5.3 Modeling second- and fourth-order problems with B-spline based finite elements

In this Section, model second- and fourth-order boundary value problems are described. The associated variational formulations are presented with emphasis on the terms stemming from Nitsche's method. A proof of consistency for the Nitsche's form for the fourth-order problem is also provided. Numerical examples demonstrating the performance of splines as finite element basis functions and the efficacy of Nitsche's method in weakly imposing Dirichlet boundary conditions while employing such a non-interpolatory basis are presented. Finally, we also present the Nitsche's variational form for the Cahn–Hilliard equation. Discretizing the variational form with a B-spline basis, several one-dimensional benchmark examples are presented.

Figure 5.3 illustrates the setting for a standard boundary value problem. The domain Ω is bounded by the Γ such that, $\Gamma = \Gamma_d \cup \Gamma_h$, where Γ_d and Γ_h are the Dirichlet and Neumann boundaries, respectively. The vector $\mathbf{n}$ represents the outward normal to the boundary at any point along Γ.

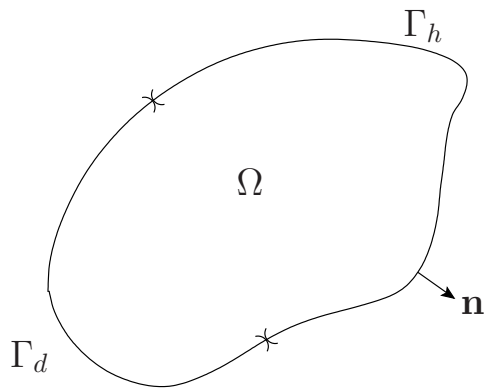

FIGURE 5.3: Domain Ω bounded by Dirichlet (Γ_d) and Neumann (Γ_h) boundaries, with unit outward normal $\mathbf{n}$.

5.3.1 Second-order boundary value problem

A Poisson equation is considered as a representative second-order problem. The Dirichlet or Neumann conditions at any point along the boundary are given by the value of the function or the normal derivative at that point. Typically, this equation models problems such as steady state heat conduction.

The boundary value problem is defined by

$$-\Delta u = f \qquad \text{in } \Omega, \tag{5.4a}$$

$$u = g \qquad \text{on } \Gamma_d, \tag{5.4b}$$

$$\nabla u \cdot \mathbf{n} = h \qquad \text{on } \Gamma_h, \tag{5.4c}$$

where Δ denotes the Laplacian, and ∇ the gradient operator.

There are several different means to derive the variational form for second-order problems with Nitsche's method, and the interested reader is directed to the works of Griebel and Schweitzer (2003) and Fernández-Méndez and Huerta (2004).

Using Nitsche's method, the variational form of the Poisson equation can be stated as:

Find $u \in \mathcal{U}$ such that

$$a(w,u) = l(w) \tag{5.5}$$

where

$$a(w,u) = \int_\Omega \nabla w \cdot \nabla u \,\mathrm{d}v - \int_{\Gamma_d} w\,(\nabla u \cdot \mathbf{n})\,\mathrm{d}a - \int_{\Gamma_d} u\,(\nabla w \cdot \mathbf{n})\,\mathrm{d}a + \alpha \int_{\Gamma_d} wu \,\mathrm{d}a, \tag{5.6a}$$

$$l(w) = \int_\Omega w\, f \,\mathrm{d}v \;+\; \int_{\Gamma_h} wh \,\mathrm{d}a \;-\; \int_{\Gamma_d} g\,(\nabla w \cdot \mathbf{n})\,\mathrm{d}a \;+\; \alpha \int_{\Gamma_d} wg \,\mathrm{d}a, \tag{5.6b}$$

for all $w \in \mathcal{V}$. Here, the solution and weighting spaces are such that both $\mathcal{U} = H^1$

and $\mathcal{V} = H^1$, where H^1 is the Sobolev space of square integrable functions with square integrable first derivatives.

In comparison to a standard penalty method, Nitsche's method involves additional integrals along the Dirichlet boundary. The additional terms give the method variational consistency, in the sense that solutions to the weak form (5.5) can be shown to be solutions to the boundary-value problem (5.4). In fact, this is the case for any choice of the stabilization parameter α. One of the means to determine stability is to examine the conditions under which the coercivity of the bilinear form is guaranteed. This naturally leads to conditions on the stabilization parameter α, as detailed in Appendix A.

Solution of Laplace equation on a square domain

We consider the problem described in Fernández-Méndez and Huerta (2004), a Laplace equation on a unit square with a sinusoidal boundary condition on one edge and homogeneous boundary conditions along the other three edges. The governing equation and boundary conditions are

$$\Delta u = 0, \tag{5.7a}$$

$$u\left(x, 0\right) = \sin\left(\pi x\right), \tag{5.7b}$$

$$u\left(x, 1\right) = u\left(0, y\right) = u\left(1, y\right) = 0, \tag{5.7c}$$

for which the analytical solution is

$$u\left(x, y\right) = \Big(\cosh\left(\pi y\right) - \coth\left(\pi\right)\sinh\left(\pi y\right)\Big)\sin\left(\pi x\right). \tag{5.8}$$

The Nitsche's variational form with $f = 0$ is discretized with uniform cubic B-splines. The stability parameters are evaluated for each element sharing the Dirichlet boundary, by solving local eigenvalue problems as explained in Appendix A. Stability parameters for all elements are identical in this case since the uniform grid conforms with the Dirichlet boundary. Figure 5.4 shows the approximation to the solution for

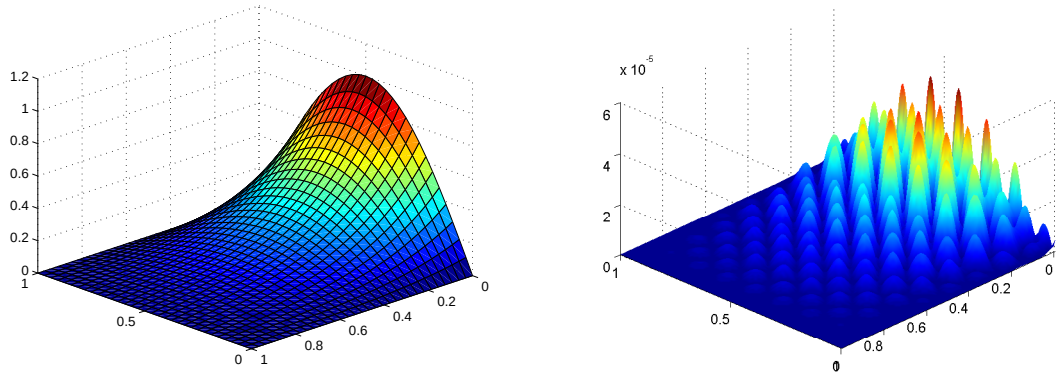

(a) (b)

FIGURE 5.4: (a) Solution to the 2D Laplace problem and (b) absolute error distribution.

a uniform grid with $h = 1/8$. Observed errors at the boundary are consistent with a weak imposition of Dirichlet conditions. Optimal rates of convergence are obtained with a cubic spline basis. A quartic convergence rate in the L_2 norm of the error and a cubic rate of convergence in the energy norm is obtained as shown in Figure 5.5. An obvious question to ask is how sensitive the results are to the choice of stability parameters, and how the parameters obtained from the eigenvalue problem compare

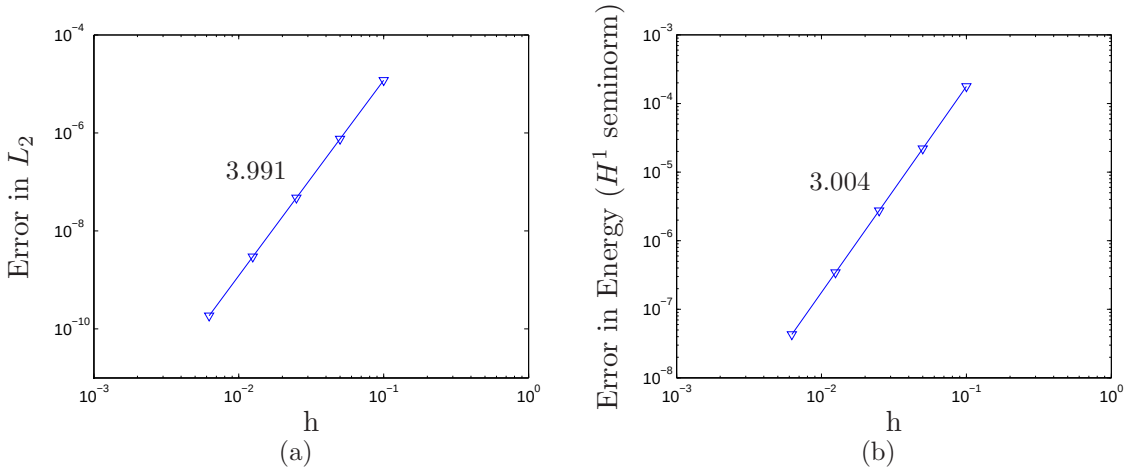

(a) (b)

FIGURE 5.5: Convergence rates for the 2D Laplace problem in (a) L_2 norm and (b) energy norm.

to an optimal choice. Accordingly, we conducted a series of numerical experiments using the same grid for this problem, but with different values for α than what was provided by the eigenvalue problem. The plot of the variation in L_2 error as a function of α is shown in Figure 5.6. It can be seen from the plot that the value provided by the eigenvalue problem yields an error that is very close to optimal.

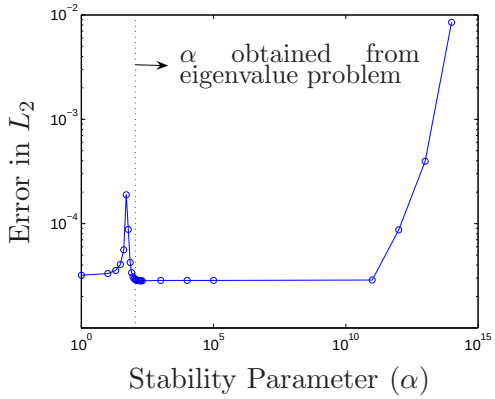

FIGURE 5.6: Variation in L_2 error norm with magnitude of the stability parameter for the Laplace problem.

5.3.2 Fourth-order boundary value problem

A non-homogenous biharmonic equation is considered for a representative fourth order problem. Here, the Dirichlet boundary conditions are specified by values of the function and its normal derivative along the boundary. Neumann boundary conditions are specified in terms of second and third-order derivatives. Beam and plate bending are representative examples of problems modeled by the biharmonic equation.

The fourth-order boundary value problem can be stated as,

$$\Delta^2 u = f \qquad \text{in } \Omega, \tag{5.9a}$$

$$u = g \;\; ; \;\; \nabla u \cdot \mathbf{n} = h \qquad \text{on } \Gamma_d, \tag{5.9b}$$

$$\Delta u = p \;\; ; \;\; \nabla(\Delta u) \cdot \mathbf{n} = q \qquad \text{on } \Gamma_h \tag{5.9c}$$

where Δ^2 denotes the biharmonic operator.

It is worth noting here that other combinations of boundary conditions can exist. A numerical example having a different combination of boundary conditions is also presented.

Nitsche's method leads to the following variational formulation which can be stated as:

Find $u \in \mathcal{U}$ such that

$$a(w,u) = l(w) \tag{5.10}$$

for all $w \in \mathcal{V}$, where

$$\begin{aligned} a(w,u) = &\int_\Omega \Delta w \Delta u \,\mathrm{d}v + \int_{\Gamma_d} w\left(\nabla(\Delta u)\cdot\mathbf{n}\right)\,\mathrm{d}a + \int_{\Gamma_d} u\left(\nabla(\Delta w)\cdot\mathbf{n}\right)\,\mathrm{d}a + \alpha_1 \int_{\Gamma_d} wu\,\mathrm{d}a \\ &- \int_{\Gamma_d} (\nabla w\cdot\mathbf{n})\,\Delta u\,\mathrm{d}a - \int_{\Gamma_d} (\nabla u\cdot\mathbf{n})\,\Delta w\,\mathrm{d}a + \alpha_2 \int_{\Gamma_d} (\nabla w\cdot\mathbf{n})\,(\nabla u\cdot\mathbf{n})\,\mathrm{d}a \end{aligned} \tag{5.11a}$$

$$\begin{aligned} l(w) = &\int_\Omega wf\,\mathrm{d}v - \int_{\Gamma_h} wq\,\mathrm{d}a + \int_{\Gamma_d} g\left(\nabla(\Delta w)\cdot\mathbf{n}\right)\,\mathrm{d}a + \alpha_1 \int_{\Gamma_d} wg\,\mathrm{d}a \\ &+ \int_{\Gamma_h} (\nabla w\cdot\mathbf{n})\,p\,\mathrm{d}a - \int_{\Gamma_d} h\Delta w\,\mathrm{d}a + \alpha_2 \int_{\Gamma_d} (\nabla w\cdot\mathbf{n})\,h\,\mathrm{d}a \end{aligned} \tag{5.11b}$$

Here, the solution and weighting spaces are such that both $\mathcal{U} = H^2$ and $\mathcal{V} = H^2$, where H^2 is the Sobolev space of square integrable functions with square integrable first and second derivatives. The stabilization parameters α_1 and α_2 are chosen to guarantee coercivity of the Nitsche form (5.11a), as described in the Appendix A.

Different terms in equations (5.11) become active depending on the combination of boundary conditions specified for a problem. The α_1 and associated terms (terms

2, 3 and 4 in (5.11a) and terms 3 and 4 in (5.11b)) appear for any boundary on which the function is specified. Similarly, α_2 and associated terms (terms 5, 6 and 7 in (5.11a) and terms 6 and 7 in (5.11b)) appear for boundaries on which the normal derivative is specified.

Proof of Consistency

Using integration by parts on the first term on the right of (5.11a),

$$\int_{\Omega} \Delta w \Delta u \, \mathrm{d}v = \int_{\Omega} \nabla \cdot \left(\left(\nabla w \right) \Delta u \right) \, \mathrm{d}v - \int_{\Omega} \nabla w \cdot \nabla \left(\Delta u \right) \, \mathrm{d}v \tag{5.12}$$

Repeating the integration by parts for the second term on the right of (5.12), we obtain

$$\int_{\Omega} \Delta w \Delta u \, \mathrm{d}v = \int_{\Omega} \nabla \cdot \left(\left(\nabla w \right) \Delta u \right) \, \mathrm{d}v - \int_{\Omega} \nabla \cdot \left(w \nabla \left(\Delta u \right) \right) \, \mathrm{d}v + \int_{\Omega} w \Delta^2 u \, \mathrm{d}v \tag{5.13}$$

Employing the divergence theorem, the above equation can be re-written as

$$\int_{\Omega} \Delta w \Delta u \, \mathrm{d}v = \int_{\Gamma_d + \Gamma_h} \left(\nabla w \cdot \mathbf{n} \right) \Delta u \mathrm{d}a - \int_{\Gamma_d + \Gamma_h} w \left(\nabla \left(\Delta u \right) \cdot \mathbf{n} \right) \, \mathrm{d}a + \int_{\Omega} w \Delta^2 u \, \mathrm{d}v \tag{5.14}$$

Substituting equation (5.14) into (5.11a), it is seen that the variational form $a\left(w,u\right) - l\left(w\right) \;\; = \;\; 0$ reduces to

$$\begin{aligned}
&\int_{\Omega} w \left(\Delta^2 u - f \right) \, \mathrm{d}v \\
&+ \int_{\Gamma_d} \left(\nabla \left(\Delta w \right) \cdot \mathbf{n} + \alpha_1 w \right) \left(u - g \right) \, \mathrm{d}a - \int_{\Gamma_d} \left(\Delta w - \alpha_2 \left(\nabla w \cdot \mathbf{n} \right) \right) \left(\left(\nabla u \cdot \mathbf{n} \right) - h \right) \, \mathrm{d}a \\
&+ \int_{\Gamma_h} \left(\nabla w \cdot \mathbf{n} \right) \;\; \left(\Delta u - p \right) \, \mathrm{d}a - \int_{\Gamma_h} w \left(\left(\nabla \left(\Delta u \right) \cdot \mathbf{n} \right) - q \right) \, \mathrm{d}a = 0
\end{aligned} \tag{5.15}$$

Invoking the arbitrary nature of $w \in \mathcal{V}$ in the above equation, the Euler-Lagrange form of (5.10) is obtained as:

$$\Delta^2 u = f \qquad \text{in } \Omega, \tag{5.16a}$$

$$u = g \;\; ; \;\; \nabla u \cdot \mathbf{n} = h \qquad \text{on } \Gamma_d, \tag{5.16b}$$

$$\Delta u = p \;\; ; \;\; \nabla(\Delta u) \cdot \mathbf{n} = q \qquad \text{on } \Gamma_h \tag{5.16c}$$

which is the non-homogenous biharmonic equation with the Dirichlet and Neumann boundary conditions. This completes the proof of consistency for the Nitsche form of the fourth-order system.

Simply Supported Square Plate

We now examine a *thin* simply supported square plate. Dirichlet boundary conditions are specified only on the primary function along the plate edges. The governing equation and boundary conditions are given as follows:

$$\Delta^2 u = q \tag{5.17a}$$

$$u = 0 \quad \& \quad \Delta u = 0 \qquad \text{at} \qquad x = 0 \quad \& \quad x = a \tag{5.17b}$$

$$u = 0 \quad \& \quad \Delta u = 0 \qquad \text{at} \qquad y = 0 \quad \& \quad y = b \tag{5.17c}$$

A sinusoidal distribution of transverse loading is assumed and is given by:

$$q = \frac{q_0}{D} \sin\left(\frac{\pi x}{a}\right) \sin\left(\frac{\pi y}{b}\right)$$

Here, u represents the transverse plate displacement. D denotes the flexural stiffness of the plate and depends on the plate thickness and material properties. The analytical solution for this problem is given by (Timoshenko et al., 1959)

$$u = \frac{q_0}{\pi^4 D\left(\frac{1}{a^2} + \frac{1}{b^2}\right)^2} \sin\left(\frac{\pi x}{a}\right) \sin\left(\frac{\pi y}{b}\right)$$

The sample problem was solved for a square plate of unit dimensions ($a = 1$ and $b = 1$) with material properties and loading such that q_0/D is unity. Plots of the

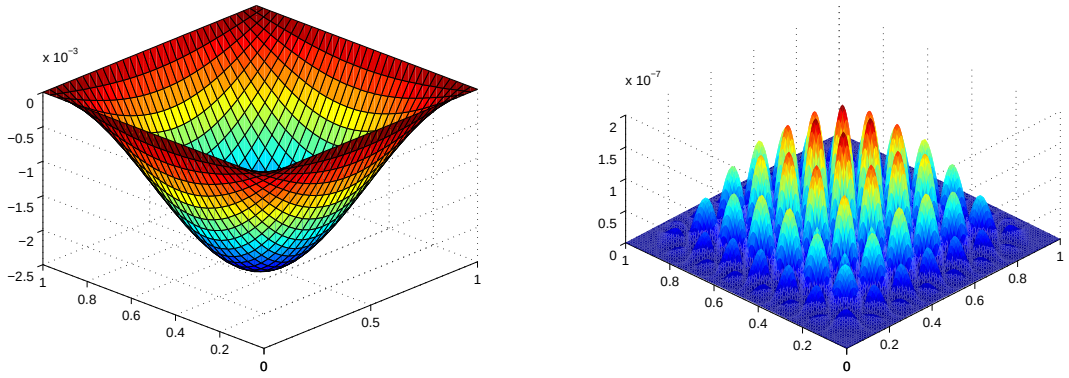

(a) Solution (b) Absolute error

FIGURE 5.7: Solution of a simply supported square plate with a sinusoidal transverse loading

transverse displacement for a uniform grid size $h = 1/8$ are given in Figure 5.7(a), while error contours are plotted in Figure 5.7(b). Figure 5.8 shows optimal convergence rates in both the L_2 and energy norms. While a quartic rate is obtained for the L_2 norm of the error, the energy norm has a quadratic rate of convergence owing to the occurrence of higher order derivatives in the bilinear form. This

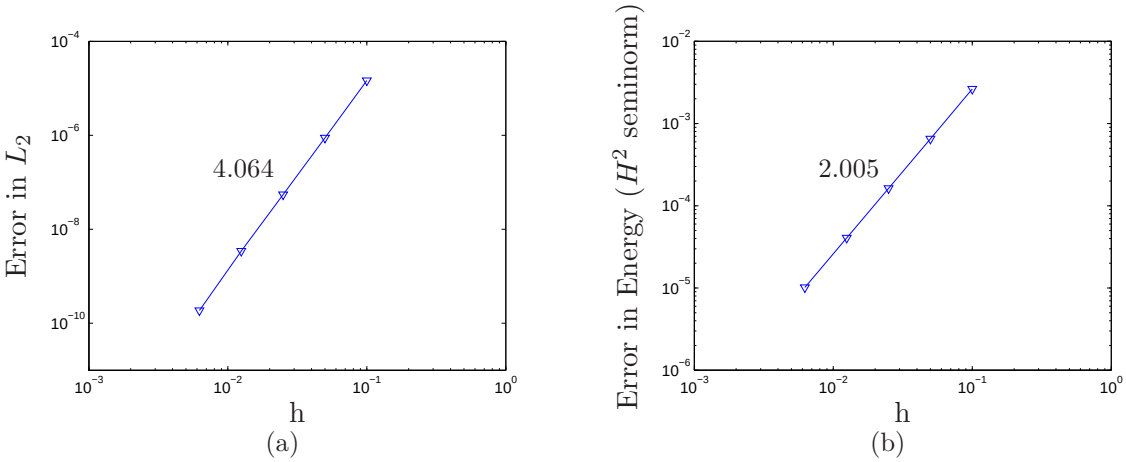

(a) (b)

FIGURE 5.8: Convergence rates for the simply supported square plate in (a) L_2 and (b) energy norms.

problem involves Dirichlet conditions only on the function. Hence, only the stability

parameter α_1 is active. We repeated the study described in the previous section that examined the variation in the error with fixed values of the stability parameter. The results shown in Figure 5.9 once again indicate that the local eigenvalue problem yields a very good estimate for α_1.

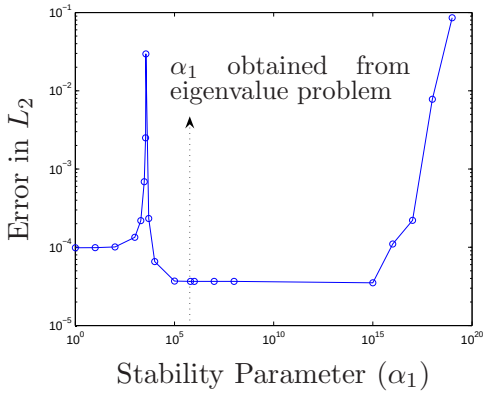

FIGURE 5.9: Variation in L_2 error norm with magnitude of stability parameter for the simply supported square plate.

Fixed Circular Plate

A *thin* unit circular plate clamped along the periphery and with uniform transverse loading is considered next. Here, Dirichlet conditions include both the function and its derivative. The boundary value problem is given by

$$\Delta^2 u = q \tag{5.19a}$$

$$u\,(r = 0.5) = 0 \tag{5.19b}$$

$$\frac{\partial u}{\partial r}\,(r = 0.5) = 0 \tag{5.19c}$$

where, r is the radial distance from the plate center. A uniform distribution of transverse loading is assumed such that,

$$q = \frac{q_0}{D} \tag{5.20}$$

The field u represents the transverse plate displacement while D is the flexural stiffness of the plate. The ratio (q_0/D) is taken to be unity in this example. The analytical solution for this problem is given by Timoshenko et al. (1959):

$$u = \frac{q_0}{64D}\left(1 - r^2\right)^2 \tag{5.21}$$

Figure 5.10(a) shows a sample uniform discretization where the grid does not con-

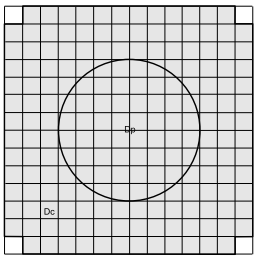

(a) Discretization with a uniform grid

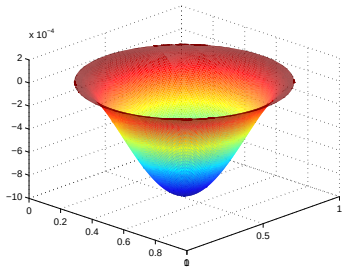

(b) Displacement pattern

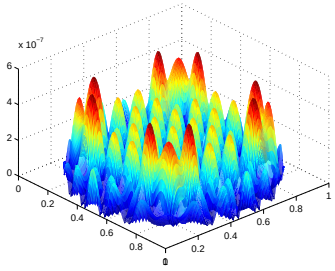

(c) Absolute error distribution

FIGURE 5.10: Discretization and results for the fixed circular plate with uniform loading.

form to the Dirichlet boundary. The corresponding solution and error distribution are shown in Figures 5.10(b) and 5.10(c). Convergence studies give spatial convergence at a near quartic rate and energy convergence at a near quadratic rate as shown in Figure 5.11.

For this numerical example, the stability parameters are associated with both the function and its derivative. Separate eigenvalue problems are set up and solved for each parameter in every boundary element. The effect of variation in magnitude of each stability parameter on the L_2 error norm was numerically studied for a sample grid with $h = 1/8$. In Figure 5.12(a), only the value of α_1 is varied while α_2 for each boundary element is maintained as evaluated from the eigenvalue problem. Similarly, Figure 5.12(b) depicts the case when only the value of α_2 is varied. The L_2 error norm is seen to be more sensitive to variations in the stability parameters as compared to

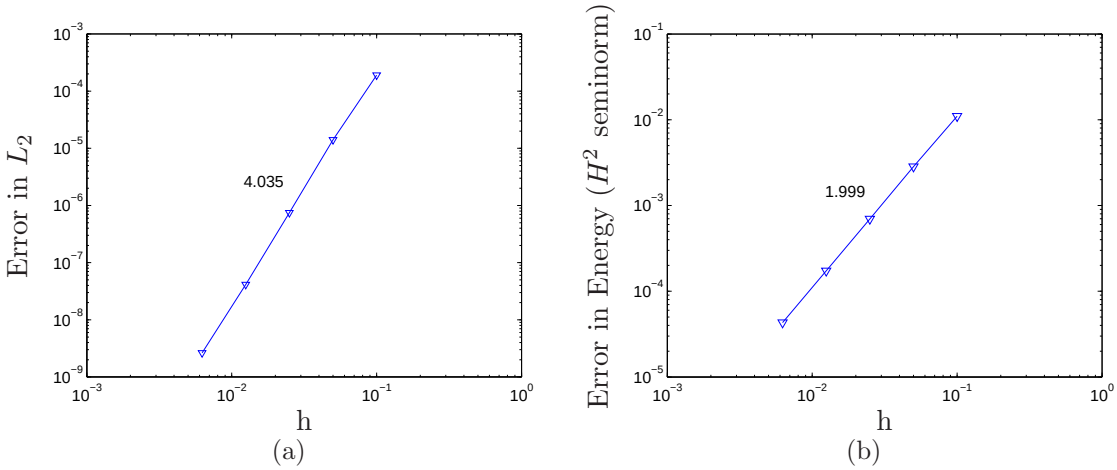

FIGURE 5.11: Convergence rates for the circular plate problem in (a) L_2 norm and (b) Energy norm.

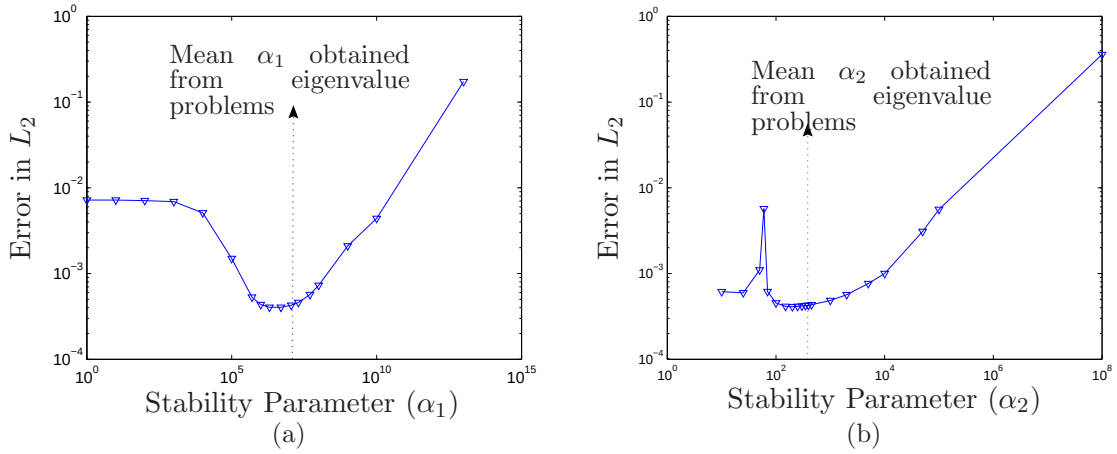

FIGURE 5.12: Variation in L_2 error norm with magnitude of stability parameters for the fixed circular plate.

the numerical examples studied in the previous sections. Nevertheless, solutions with minimal L_2 errors are obtained over a range of about two orders of magnitude for both α_1 and α_2. The local eigenvalue problems provide estimates in the optimal range for both parameters.

Robustness Study

A parametric study was performed in order to evaluate the robustness of the proposed approach. The fixed circular plate problem was chosen since it not only involves grids that do not conform to the Dirichlet boundary, but also includes Dirichlet conditions on both the function and its derivative. The center of the circular plate, having unit

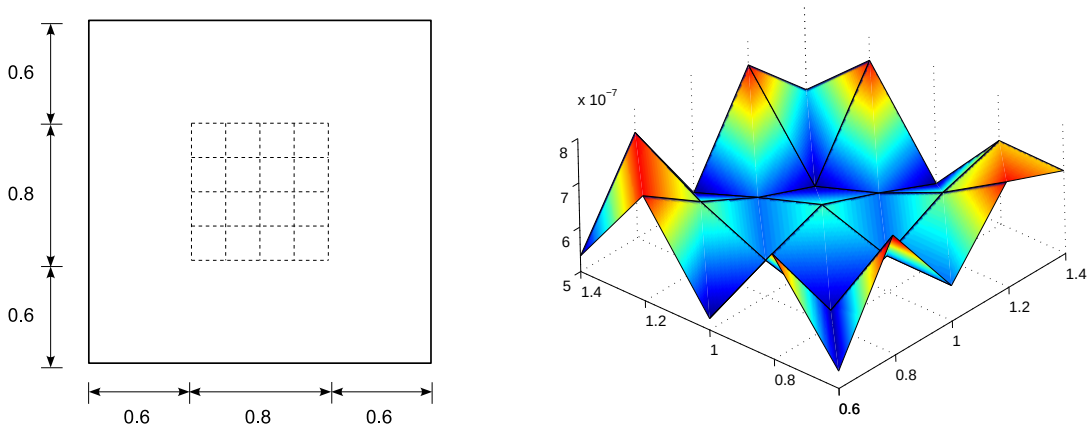

(a) Multiple locations of the circular domain center

(b) Absolute maximum error for each center location

FIGURE 5.13: Robustness study for the circular plate problem.

diameter, was moved in both x and y directions along the parent grid. All other data remain unchanged. The locations used for the center of the circular domain are shown in Figure 5.13(a). Discretization was maintained at a constant level with a grid size of $h = 1/8$. Fairly consistent results were obtained for all different locations of the circular domain. Figure 5.13(b) shows a plot of the absolute maximum error as a function of position of the circular domain center.

5.3.3 Cahn–Hilliard equation

The Cahn–Hilliard energy similar to (4.2), but now in Euclidean form, can be written as:

$$E_{\mathrm{c}} = \int_{\Omega} \left(f(c) + \frac{\lambda}{2} \left| \nabla c \right|^2 \right) \mathrm{d}v. \tag{5.22}$$

The associated continuity equation, also referred to as the Cahn–Hilliard equation is:

$$\frac{\partial c}{\partial t} = \nabla \cdot (M \nabla \mu), \tag{5.23a}$$

$$\mu = \frac{\delta E_{\mathrm{c}}}{\delta c} = f'(c) - \lambda \Delta c, \tag{5.23b}$$

subject to the mass conservation conditions

$$\nabla c \cdot \mathbf{n} = 0 \qquad \text{and} \qquad \nabla \mu \cdot \mathbf{n} = 0 \qquad \text{on} \qquad \Gamma \times (0, T), \tag{5.24}$$

and the initial condition

$$c(\boldsymbol{x}, 0) = c_0(\boldsymbol{x}) \qquad \text{in} \qquad \Omega. \tag{5.25}$$

Accounting for the zero mass flux boundary conditions, the Nitsche weak form can be derived from the Cahn–Hilliard equation (5.23). Assuming a constant mobility M, the weak form can be stated as,

Find $c \in \mathcal{U} \times [0, T]$ such that,

$$\int_{\Omega} w \frac{\partial c}{\partial t} \, \mathrm{d}v + M \int_{\Omega} f''(c) (\nabla w \cdot \nabla c) \, \mathrm{d}v + \gamma M \int_{\Omega} \Delta w \cdot \Delta c \, \mathrm{d}v - \gamma M \int_{\Gamma} \Delta c (\nabla w \cdot \mathbf{n}) \, \mathrm{d}a$$

$$- \gamma M \int_{\Gamma} \Delta w (\nabla c \cdot \mathbf{n}) \, \mathrm{d}a + \alpha \int_{\Gamma} \left(\nabla w \cdot \mathbf{n} \right) \left(\nabla c \cdot \mathbf{n} \right) \, \mathrm{d}a = 0, \tag{5.26a}$$

$$\int_{\Omega} w c(t = 0) \, \mathrm{d}v = \int_{\Omega} w c_0 \, \mathrm{d}v \tag{5.26b}$$

for all $w \in \mathcal{V} \subset H^2(\Omega)$. Here, $H^2(\Omega)$ is the Sobolev space of order 2. $\mathcal{U}$ is the admissible space of concentration fields such that $\mathcal{U} \subset H^2$. Equation (5.26b) is a weak statement of the initial condition.

A note on the Nitsche form: The integrals involving normal derivatives at the boundary lend consistency and symmetry to the system while the integral with parameter α stabilizes the system of equations. To ensure coercivity of the bilinear form, the stability parameter α can be evaluated by solving a local generalized eigenvalue problem at the Dirichlet boundary, similar in spirit to the discussion in Appendix A. However, in the current study, α is maintained constant and is taken sufficiently large so as to enforce coercivity of the bilinear form.

A cubic B-spline basis is employed to obtain a conforming discretization of (5.26). A Backward-Euler method is used for time integration. The discretized system of nonlinear equations is then solved using a full Newton-Raphson scheme.

Numerical results

Several one-dimensional numerical examples are benchmarked against established numerical solutions for the Cahn–Hilliard equation (Elliott and French, 1987). A symmetric quartic double-well potential $f(c)$ of the form

$$f(c) = \frac{c^4}{12} - \frac{c^2}{2} \tag{5.27}$$

is assumed. Of the three stationary points of f, two represent the global minima at $u_a = -\sqrt{3}$ and $u_b = \sqrt{3}$, also referred to as the binodal points. The third is a local maximum and occurs at $c = 0$. Spinodal points are obtained by $\partial^2 f/\partial c^2 = 0$ and are given by ${u_s}^a = -1$ and ${u_s}^b = 1$.

(a) Convergence to a uniform steady state

The mean value of the initial spatial distribution of concentration is set to be well beyond the binodal points. Since this is a stable region, no decomposition of the

binary mixture is expected. The initial condition for the concentration field is set using a ninth degree polynomial

$$p(x) = x^4(x - L)^4(x - r_0) + M_0. \tag{5.28}$$

Here, $r_0 = 2.2$ and 'L' is the domain size. M_0 is chosen so that,

$$\int_0^L p(x)\ \mathrm{d}\Omega = 0 \tag{5.29}$$

T

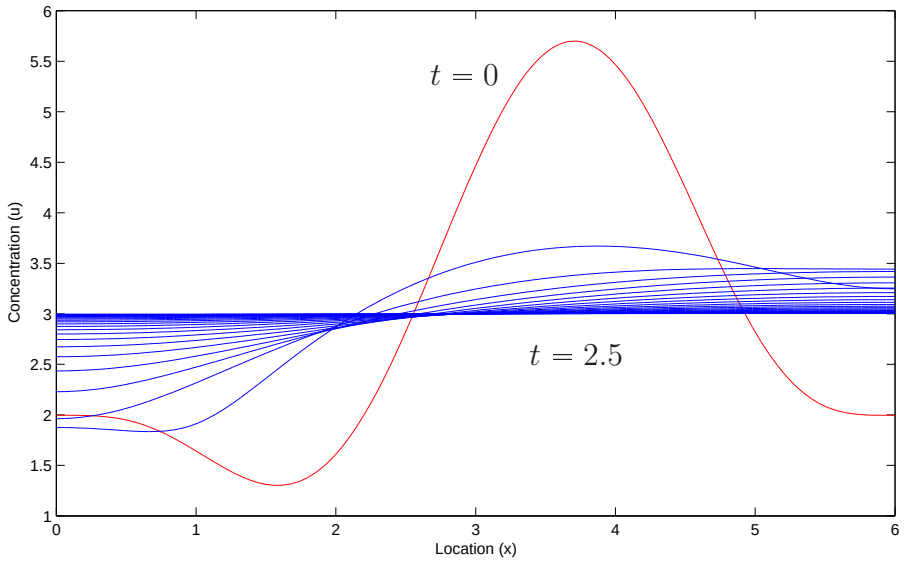

FIGURE 5.14: Convergence to Steady State, $u = 3.0$, with 100 elements. Here, $dt = 0.001$ and $\gamma = 5.0e - 04$.

$$u_0 = Ap(x) + M_u \text{ so that } \int_0^L u_0(x)\ \mathrm{d}\Omega = M_u L \tag{5.30}$$

Here, A is chosen so that $|u_0 - M_u| \cong 2.7$. M_u represents the mean value of the spatial distribution of the initial concentration. Setting $L = 6$ and $M_u = 3.0$ (well beyond the binodal points), the evolution of concentration is plotted in Figure 5.14. As it can be seen, no decomposition of the mixture occurs and the steady state solution

approaches the mean value $M_u = 3$. Steady state is reached at around $t = 2.3s$, while the simulation was continued to $t = 2.5s$.

(b) Spinodal Decomposition

The mean value of the initial spatial distribution of concentration is set to be in the spinodal region. Being inherently unstable, the mixture is expected to evolve into 2 distinct phases, each phase being represented by a global minimum of the free energy function f. An initial concentration distribution given by $c_0(x) = \cos(\pi x/L)$

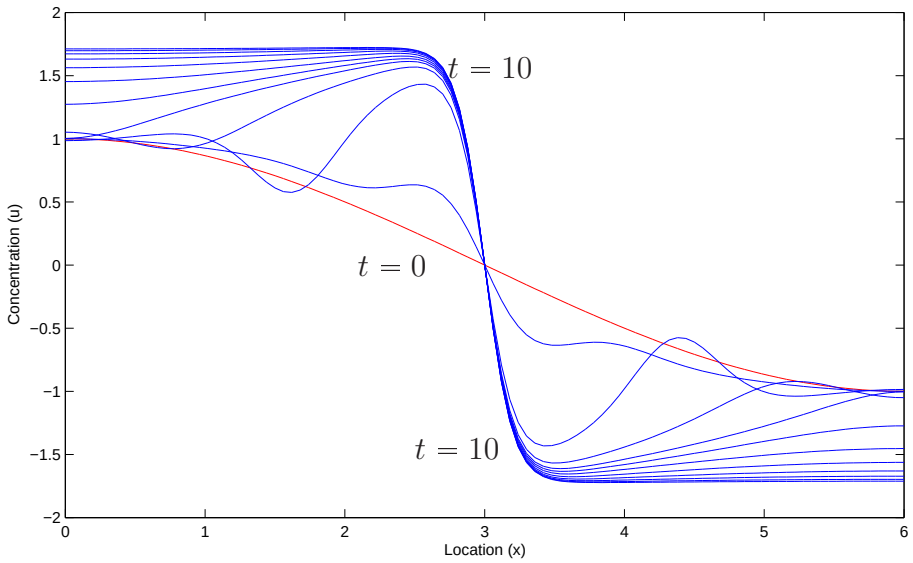

FIGURE 5.15: Spinodal decomposition with 100 elements. $dt = 0.001$, $\gamma = 0.02$ and $L = 6$.

and having a mean concentration of $\overline{c} = 0$ in the spinodal region is used. As shown in Figure 5.15, the mixture clearly separates into 2 phases with the concentration values corresponding to the two global minima.

When the initial concentration is set similar to (5.30) but now with the mean $M_u = 0$ and 'A' chosen such that $|u_0| \cong 0.5$, the spatial distribution of the initial concentration completely falls within the spinodal region. Figure 5.16 shows the distribution at the end of spinodal decomposition as a piece-wise linear solution separated by interfaces. This essentially represents the evolution of the mixture to

its 2 constituents along the domain.

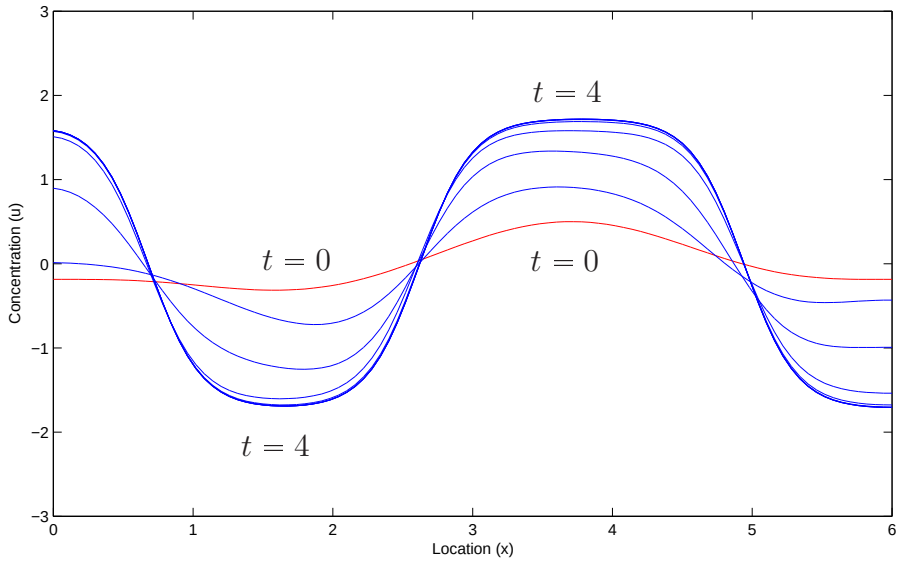

FIGURE 5.16: Spinodal decomposition with 100 elements. $dt = 0.001$ and $\gamma = 0.07$.

5.4 Summary

B-splines are an attractive option as a finite element basis, especially for higher-order problems. This Chapter discusses the details of building uniform cubic spline functions as a conforming finite element basis. A challenging aspect of using splines as a finite element basis is the imposition of Dirichlet boundary conditions. This work presents a robust technique to weakly impose Dirichlet boundary conditions by employing Nitsche's method for stability. Details of numerically evaluating the stabilization parameters by setting up and solving local generalized eigenvalue problems are discussed. Numerical examples demonstrating optimal rates of convergence for second- and fourth-order linear problems are presented. Using the Cahn–Hilliard equation as a representative fourth-order nonlinear evolution equation, several one-dimensional benchmark examples of the numerical solution with a cubic spline basis are also presented. On similar lines, Chapter 6 discusses the aspects of numerical

modeling of the governing equations of vesicle shape change and species transport.

6

Numerical Modeling of Vesicles

6.1 Introduction

The shape and species transport equations are solved within a finite-element framework. Details of the spatial and temporal discretization are discussed. In addition, a data extension technique used to indirectly tie the concentration band to the shape changes of the vesicle is described. The computational scheme accounting for instantaneous shape equilibrium at every stage of species transport is outlined.

6.2 Variational form of the governing equations

Introducing the Euler–Lagrange form of the energy (4.32) associated with the zero-flux constraint (4.31), the variational form for the equation of species transport (4.26) can be stated as:

Find $c \in \mathcal{U}$ such that

$$\int_\Omega w \frac{\partial c}{\partial t}\,\delta_s\,\mathrm{d}v = \int_\Omega M\mu\nabla\cdot((\boldsymbol{1}-\mathbf{n}\otimes\mathbf{n})\nabla w)\,\delta_s\,\mathrm{d}v + \alpha_m\int_\Omega(\nabla w\cdot\mathbf{n})(\nabla c\cdot\mathbf{n})\,\delta_s\,\mathrm{d}v \tag{6.1a}$$

$$\int_\Omega wc(t=0)\,\mathrm{d}v = \int_\Omega wc_0\,\mathrm{d}v \tag{6.1b}$$

for all $w \in \mathcal{V}$. The solution and weighting spaces are such that both $\mathcal{U} = H^2$ and $\mathcal{V} = H^2$, where is H^2 is the Sobolev space of square integrable functions with square integrable first and second derivatives. The chemical potential μ is given by (4.30b) and is second order in c. The variational form (6.1a) is derived by repeated integration by parts of the weighted-residual form of (4.26) and by noting that the species mobility M is taken to be a constant. Equation (6.1b) provides the weak statement of the initial condition for concentration.

The variational form of the gradient-flow augmentation of the shape equation can be stated as:

Find $\phi \in \mathcal{U}$ such that

$$\begin{aligned}\int_\Omega w\frac{\partial\phi}{\partial\tau}\,\mathrm{d}v = &-\frac{3\sqrt{2}}{4}\int_\Omega \psi(c)\left(\frac{wg'(\phi)}{\epsilon_\phi}+\epsilon_\phi(\nabla w\cdot\nabla\phi)\right)\mathrm{d}v\\ &-\frac{3\sqrt{2}\epsilon_c^2\epsilon_\phi}{16}\int_\Omega \kappa(c)F(\phi)\left(\Delta w+\frac{w(1-3\phi^2)}{\epsilon_\phi}\right.\\ &\left.+\frac{2\sqrt{2}}{\epsilon_\phi}w\phi H_{\mathrm{sp}}(c)\right)\mathrm{d}v \qquad (6.2a)\\ &+\frac{\alpha_v}{2V_0}\left(V_R-1\right)\int_\Omega w\,\mathrm{d}v\\ &-\frac{3\sqrt{2}}{4}\frac{\alpha_a}{A_0}\left(A_R-1\right)\int_\Omega\left(\frac{wg'(\phi)}{\epsilon_\phi}+\epsilon_\phi(\nabla w\cdot\nabla\phi)\right)\mathrm{d}v,\end{aligned}$$

$$\int_\Omega w\phi(t=0)\,\mathrm{d}v = \int_\Omega w\phi_0\,\mathrm{d}v \qquad (6.2b)$$

for all $w \in \mathcal{V}$. Again, the solution and weighting spaces are such that both $\mathcal{U} = H^2$ and $\mathcal{V} = H^2$. The functions $g(\phi), F(\phi)$ and $\psi(c)$ are defined following (4.33). Equation (6.2b) is the weak statement of the initial condition for ϕ. Essentially, the zero level surface of ϕ_0 describes the initial shape of the vesicle.

6.3 Spatial discretization

The diffuse-interface forms of the shape change and species transport equations are nonlinear fourth-order partial-differential equations and are re-cast in variational form. A standard finite-element approximation of a fourth-order differential equation requires the solution and weighting spaces to be globally H^2 conforming—i.e., C^1-continuous. As discussed in Chapter 5, a B-spline basis providing global higher-order continuity is used to model the fourth-order governing equations.

6.4 Time discretization

While fully explicit time stepping schemes for fourth-order partial-differential equations suffer from severe restrictions on the time step size, fully implicit schemes, albeit unconditionally stable, can involve certain complications, especially when using a non-standard basis whose support extends well beyond an element. For instance, the geometric constraints required to be imposed during shape equilibrium are nonlocal. Solution of the nonlinear governing equation (4.34) with a fully implicit scheme would require the computation of directional derivatives of the nonlocal terms (V_R and A_R in (4.33c)), resulting in a huge computational cost. To overcome this difficulty, we use a semi-implicit time stepping scheme. Following the work of Eyre (Eyre, 1997), the energy is decomposed into purely convex and concave terms. While the concave terms are treated explicitly, convex terms are treated implicitly. The resulting computational framework ensures that the functional E does not increase along solution paths (Eyre, 1997). In the present work, a splitting of the form

$$E = (1+\gamma_1)E_{\mathrm{m}} + (E_{\mathrm{gc}} - \gamma_1 E_{\mathrm{m}}) + E_{\mathrm{c}}^{\mathrm{ccv}} + E_{\mathrm{c}}^{\mathrm{cvx}} \tag{6.3}$$

is used for the functional E, where γ_1 is a scaling factor used to ensure the concavity of $E_{\mathrm{gc}} - \gamma_1 E_{\mathrm{m}}$ and, $E_{\mathrm{c}}^{\mathrm{ccv}}$ and $E_{\mathrm{c}}^{\mathrm{cvx}}$ are the concave and convex components of the chemical energy E_{c} (4.26). We use a decomposition of E_{c} of the form $E_{\mathrm{c}} = E_{\mathrm{c}}^{\mathrm{ccv}} + E_{\mathrm{c}}^{\mathrm{cvx}}$, with

$$E_{\mathrm{c}}^{\mathrm{ccv}} \approx \frac{3\sqrt{2}}{4} \int_{\Omega} \psi(c) \Big(\frac{(1-\phi^2)^2}{4\,\epsilon_\phi} - \gamma_2\,\phi^2 \Big)\, \mathrm{d}v, \tag{6.4a}$$

$$E_{\mathrm{c}}^{\mathrm{cvx}} \approx \frac{3\sqrt{2}}{4} \int_{\Omega} \psi(c) \left(\gamma_2\,\phi^2 + \frac{\epsilon_\phi}{2}\,|\nabla\phi|^2 \right)\, \mathrm{d}v, \tag{6.4b}$$

in which $\psi(c)$ is defined immediately after (4.33). Choosing the scaling factor γ_2 in (6.4) to ensure concavity of $E_{\mathrm{c}}^{\mathrm{ccv}}$, we obtain

$$\gamma_2 > \frac{3\phi^2 - 1}{2\epsilon_\phi}. \tag{6.5}$$

Further, since $-1 \leqslant \phi \leqslant 1$, $E_{\mathrm{c}}^{\mathrm{ccv}}$ is concave for $\gamma_2 > 1/\epsilon_\phi$. For the numerical examples in the present study, choosing γ_1 and γ_2 such that

$$10 \leqslant \gamma_1 \leqslant 25 \qquad \text{and} \qquad \gamma_2 = \frac{2}{\epsilon_\phi} \tag{6.6}$$

suffices to ensure that the functional E does not increase during relaxation towards shape equilibrium.

The semi-implicit scheme for the gradient-flow augmentation (4.34) of the shape equation is then rewritten as

$$\begin{aligned}\frac{\partial\phi}{\partial\tau} = \left(\frac{\phi^{n+1} - \phi^n}{\Delta\tau}\right) = -(1+\gamma_1)\frac{\delta E_{\mathrm{m}}}{\delta\phi}\bigg|^{n+1} - \frac{\delta E_{\mathrm{c}}^{\mathrm{cvx}}}{\delta\phi}\bigg|^{n+1} \\ - \left(\frac{\delta E_{\mathrm{gc}}}{\delta\phi} - \gamma_1\frac{\delta E_{\mathrm{m}}}{\delta\phi}\right)\bigg|^{n} - \frac{\delta E_{\mathrm{c}}^{\mathrm{ccv}}}{\delta\phi}\bigg|^{n},\end{aligned} \tag{6.7}$$

where the superscripts indicate the pseudo-time step at which the corresponding quantities are evaluated.

A similar scheme can be attempted for the species transport equation. However, the decomposition of the curvature energy into purely convex and concave terms in the order parameter c can be a challenge. Manipulation of the curvature energy with purely convex functions in c was found to affect the dynamics of phase separation in comparison to a purely implicit scheme. To avoid this issue, we employ a fully implicit backward-Euler time-stepping method for species transport. Further, the linearized system of equations for both shape equilibrium and species transport are solved using a full Newton–Raphson method.

6.5 Data extension normal to the surface

As the shape of the vesicle evolves to minimize net energy, the concentration representing the lipid species distribution on the surface should follow the shape changes. Computationally, however, due to the spatial formulation of the governing equations (and, thus, the complete absence of a reference configuration), shape changes can occur independent of the concentration. This is understood by noting that although solving equation (4.34) to steady state achieves shape equilibrium, no explicit constraint requires the band of concentration to move with the surface as steady state is approached. In the present study, the above condition is realized approximately by an extension technique commonly used in the level-set community (Bertalmio et al., 2001; Greer et al., 2006; Adalsteinsson and Sethian, 2003). The concentration on the surface (which is identified with the zero level-set of ϕ) is extended to other level sets of ϕ by solving the following wave equation to steady state:

$$\frac{\partial c}{\partial \tau} + \Psi(\nabla c \cdot \mathbf{n}) = 0, \quad \text{where} \quad \mathbf{n} = \frac{\nabla \phi}{|\nabla \phi|}. \tag{6.8}$$

Here, Ψ is taken to be a smoothed signum function that vanishes on the zero level-set of ϕ. During evolution, data on the zero level-set of ϕ is transmitted in both the positive ($\phi > 0$) and negative ($\phi < 0$) directions along the surface normal while the surface data itself remains unchanged.

The phase field ϕ, as depicted in Figure 3.1(b), is a candidate for the signum function. Employing a signum function for Ψ while solving (6.8) to steady state leads to extending the surface data over the entire computational domain. This would result both in regions where data extensions from different points on the surface intersect and potentially conflict, and in unnecessary computational overhead. Practically, data extension is required only within a narrow band encompassing the surface. If the evolution of equation (6.8) is constrained by forcing $\partial c/\partial \tau = 0$ for

any point outside the band, an unresolved jump in the values of c develops along the boundaries of the band. Numerical noise is observed in these regions. Eventually, the noise infiltrates the band and corrupts the solution.

An alternate approach is used to avoid this issue. Here, Ψ is taken to be the product of the smoothed signum function with the approximate delta function δ_S. A qualitative plot of a smoothed signum function and Ψ are provided in Figure 6.1. It is seen that Ψ provides a smooth cut-off for the band. While data extension is restricted, it also ensures that no jumps exist along the boundaries of the band, thereby minimizing numerical noise.

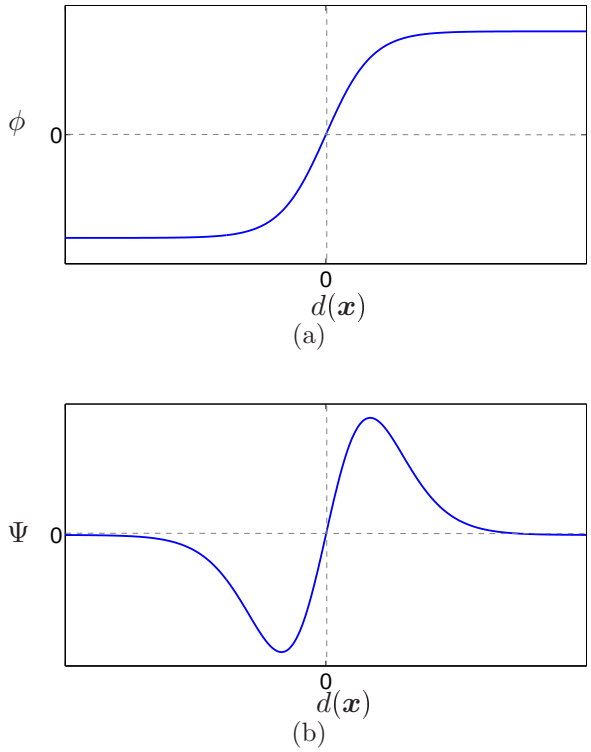

FIGURE 6.1: (a) Smoothed signum function (Greer et al., 2006). (b) Ψ.

6.5.1 Numerical solution of the wave equation

Extension of the concentration data on the surface to a neighborhood is realized through (6.8), which corresponds to a one-dimensional wave equation along the surface normal. Equation (6.8) can be considered to be similar to the advective limit of the standard advection-diffusion equation, the solution of which continues to be a subject of extensive research in stabilized finite element methods. The semi-discrete variational form of (6.8) can be stated as:

Find $c \in H_0^1(\Omega)$ such that for all $w \in H_0^1$,

$$\int_{\Omega} w \frac{\partial c}{\partial t} \mathrm{d}v + \int_{\Omega} w \Psi(\nabla c \cdot \mathbf{n}) \mathrm{d}v = 0. \tag{6.9}$$

Employing a standard Galerkin finite-element approach to approximate (6.9) is known to result in spurious oscillations in the numerical solution. We employ the well established Streamline Upwind Petrov Galerkin (SUPG) stabilization (Brooks and Hughes, 1982) in space. The SUPG method coincides with the Galerkin Least Squares (GLS) finite element method (Hughes et al., 1989) for the pure advection problem. Essentially, the semi-discrete Galerkin form of (6.9) is augmented with a stabilization term, while ensuring consistency of the solution to the variational problem. Since the wave equation simulates data flow in the direction normal to the vesicle mid-surface, the velocity of flow at any point is taken to be given by the unit surface normal at that point. In view of this, the stabilized Galerkin form can be stated as,

Find $c^h \in \mathcal{U}^h$ such that for all $w^h \in \mathcal{V}^h \subset H_0^1$,

$$\int_{\Omega} w^h \frac{\partial c^h}{\partial \tau} \mathrm{d}v + \int_{\Omega} w^h \Psi(\nabla c^h \cdot \mathbf{n}) \mathrm{d}v + \sum_e \int_{\Omega^e} \upsilon (\nabla w^h \cdot \mathbf{n}) \Big(\frac{\partial c^h}{\partial \tau} + \Psi(\nabla c^h \cdot \mathbf{n}) \Big) = 0, \tag{6.10}$$

where υ is a stability parameter, Ω_e represents the element domain and the summa-

tion is performed over all elements in the domain. Essentially,

$$\Omega = \bigcup_{e} \Omega_e. \tag{6.11}$$

The choice of the stability parameter is known to be crucial for accuracy and stability of the SUPG method. Further, the stability parameter is chosen as a function of the element size ($\upsilon \to 0$ as $h \to 0$). This tuning ensures that υ is less pronounced for highly refined grids. Based on error analysis considerations, Franca and Frey (1992) present expressions for the stability parameter. We adopt this approach and for the pure advection equation, the stability parameter has the form

$$\upsilon = \frac{h_n}{2||\mathbf{n}||} \tag{6.12}$$

where h_n is the element length in the direction of flow velocity (surface normal in the present case) and $||\mathbf{n}||$ represents the magnitude of the velocity ($= 1$ for a unit normal). The parameter h_n can be taken as

$$h_n = h_\xi n_\xi + h_\eta n_\eta + h_\zeta n_\zeta \tag{6.13}$$

where, h_ξ, h_η and h_ζ are the characteristic element lengths and n_ξ, n_η and n_ζ are the components of the normal relative to the basis corresponding to the ξ, η and ζ element coordinates.

The stability, continuity and error estimates for the stabilized forms of steady advection-diffusion equations are presented in detail in Franca and Frey (1992) for Lagrangian basis functions and in Bazilevs et al. (2006) for basis functions having a higher regularity, such as B-splines and NURBS. Further, the semi-discrete treatment of the transient advection-diffusion problem with a fully implicit time integrator and with an SUPG spatial stabilization is shown to be stable in time and space (Bochev et al., 2004).

In the present work, we employ a trapezoidal time-integration scheme and the SUPG stabilization in space. Benchmark examples to evaluate the performance of the stabilized advection equation (6.10) are presented here.

EXAMPLE I

We consider a circle of radius $r = 0.6$ units embedded in a square of side 2.2 units. The circle is implicitly represented by the phase field ϕ. We use an initial concentration field given by $c(\mathbf{x}) = 1 + d(\mathbf{x})$ where $d(\mathbf{x})$ is the signed distance function representing the distance from the zero-level set of ϕ. Essentially, this gives $c = 1$ on the circle ($\phi = 0$). Data extension should result in the formation of a band with

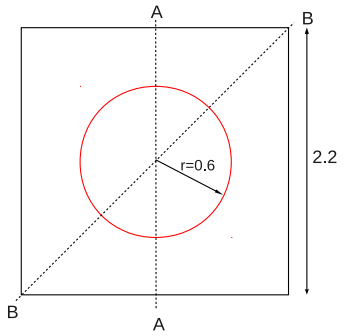

(a) Definition of sections

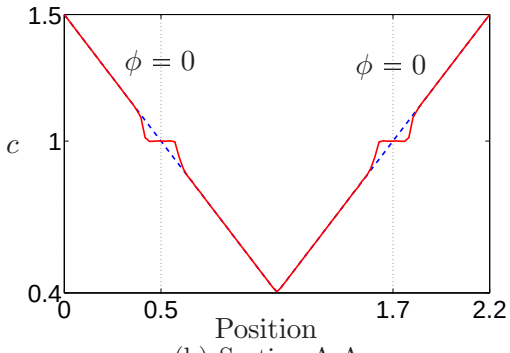

(b) Section A-A

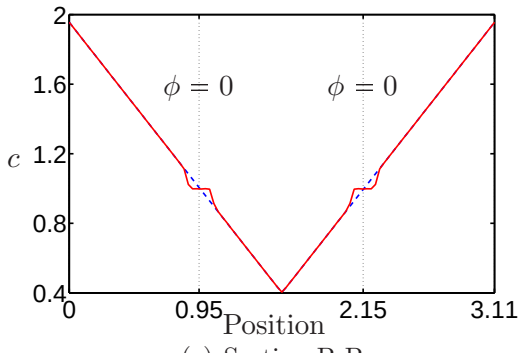

(c) Section B-B

FIGURE 6.2: Concentration profile along different sections. The dashed blue lines and the solid red lines represent the concentration profile before and after data extension, respectively. Dashed vertical lines represent the location of $\phi = 0$.

a uniform value of $c = 1$ so that

$$\int_{\Omega} c\delta_s \, \mathrm{d}v \approx \int_{\Omega} \delta_s \, \mathrm{d}v. \tag{6.14}$$

Thus, the above integral should approximate to the perimeter of the circle. In the present example, comparison of (6.14) with the perimeter of the circle results in a relative error of 0.03%. The cross-section of the concentration field before and after data extension is given in Figure 6.2. In the following two examples, data extension is performed on a concentration field with much steeper variations as compared to the signed distance function.

EXAMPLE II

We consider a geometry as described in Figure 6.2(a). The circle is implicitly represented by the phase field ϕ. A cosine distribution along the y coordinate axis is assumed for the concentration field c as shown in Figure 6.3(a), where the zero level set of ϕ is represented by the embedded circle. The concentration distribution after data extension is shown in Figure 6.3(b). The cross-section of the concentration field

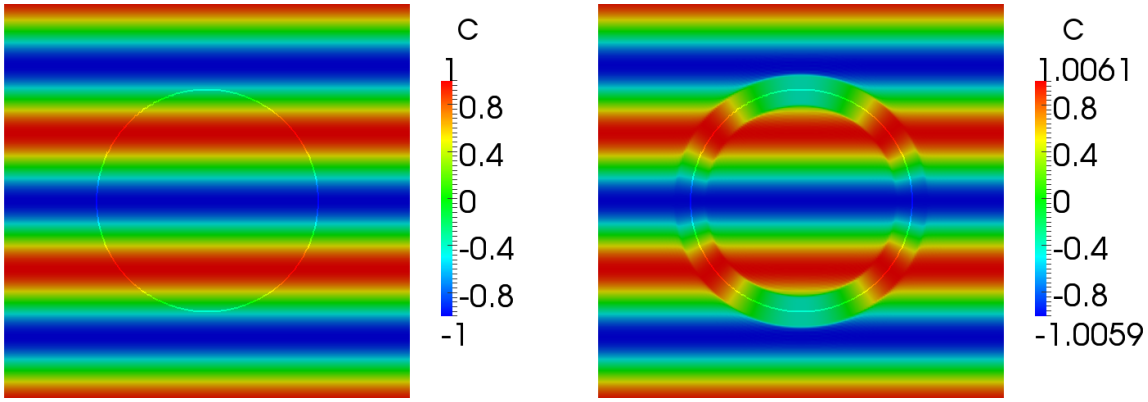

(a) (b)

FIGURE 6.3: Distribution of the concentration field c: (a) initial state, (b) after data extension. The line representing the circle correponds to $\phi = 0$.

before and after data extension is given in Figures 6.4(a) and 6.4(b).

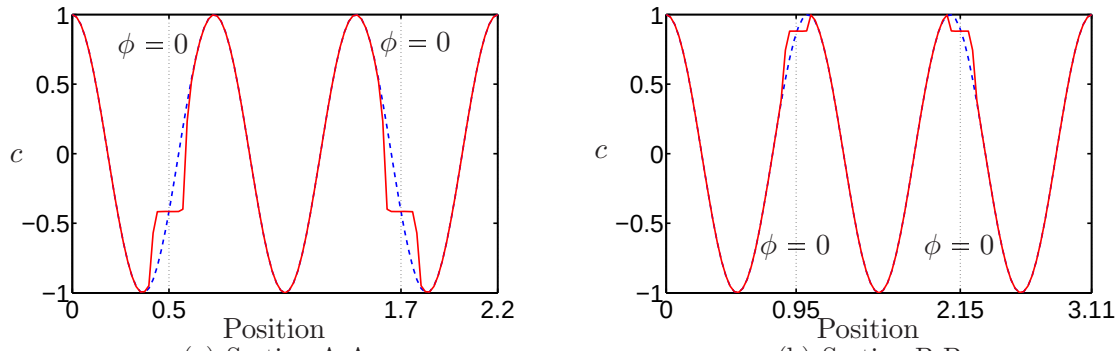

(a) Section A-A (b) Section B-B

FIGURE 6.4: Distribution of the concentration field c: (a) initial state, (b) after data extension. The dashed blue lines and the solid red lines represent the concentration profile before and after data extension, respectively. Dashed vertical lines represent the location of $\phi = 0$.

EXAMPLE III

An ellipse of semi-major axis measuring 0.9 units oriented along the x coordinate axis and a semi-minor axis measuring 0.4 units is embedded in a square of side 2.2 units. The concentration field is again assumed to be a cosine distribution as shown in Figure 6.5(a). Data extension leads to the formation of a band encompassing the ellipse as shown in Figure 6.5(b).

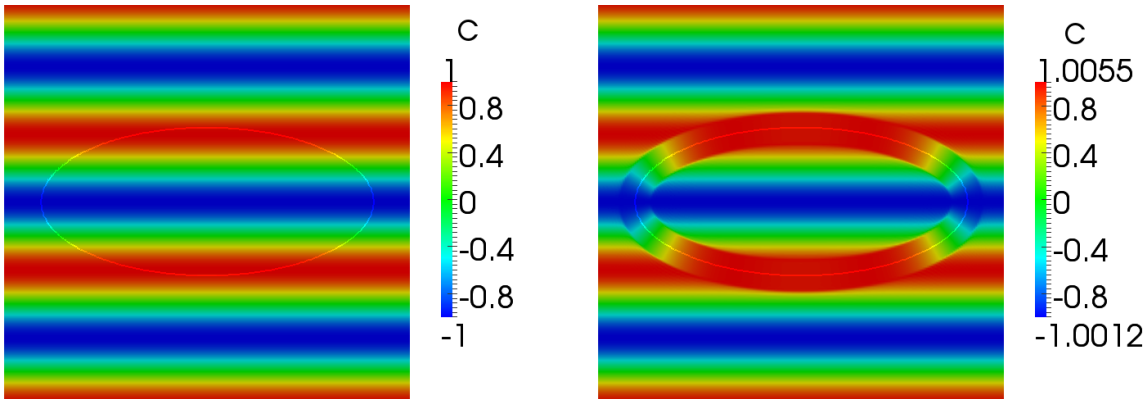

(a) (b)

FIGURE 6.5: (a) Distribution of the concentration field c (a) Initial state, (b) After data extension. The line representing the ellipse correponds to $\phi = 0$.

As demonstrated by the two-dimensional numerical examples, solution of the pure

advection equation (6.8) using a finite element framework stabilized by the SUPG method (6.12) and with a trapezoidal time integration scheme results in a smooth flow of data from the zero level set of the surface. Further, no perceptible noise is observed in the region of data extension. We employ this approach in all numerical examples with binary phases. Data extension is used to set up the initial condition for concentration and also to approximately couple the band of concentration to the deforming vesicle surface. Details of the implementation are given in the following Section.

6.6 Computational Scheme

The model is intended to study a regime where phase separation occurs on a time scale significantly longer than that associated with shape changes. While a natural time scale can be associated with species transport, the vesicle is assumed to instantaneously reach shape equilibrium at all times during the evolution process. This phenomenon is numerically simulated using a scheme in which the vesicle is driven to shape equilibrium at each time step involving coupled species transport and shape evolution.

The initial shape of the vesicle is defined as the zero level-set of a phase field ϕ given by

$$\phi = \tanh\Big(\frac{d(\boldsymbol{x})}{\sqrt{2}\epsilon_\phi}\Big). \tag{6.15}$$

The initial spatial distribution of the concentration c of lipid species is prescribed on the whole computational domain such that $c(S, t = 0) = c_0^s$. The computational framework for the coupled process is outlined below:

1. Prepare initial conditions

a) Project the initial vesicle shape described by the function ϕ and concentra-

tion described by the function c onto a spline basis, using an L_2 projection scheme.

b) Extend the concentration data normal to the surface by solving the hyperbolic equation (6.8) to steady state, with SUPG stabilization.

c) Using a semi-implicit scheme, drive the system to shape equilibrium by solving equation (4.34) to steady state. During this process, the concentration must be coupled to the deforming level sets of ϕ using data extension. This is achieved by performing step 1b frequently during the evolution towards shape equilibrium.

d) At steady-state, (4.34) gives the equilibrated shape of the vesicle for the initial concentration distribution. The initial conditions are now set and ready for the main solve.

2. Main solve (species transport)

Do while $\partial c/\partial t > 0$:

a) Time march one step by solving equations (4.30) for c^{n+1}.

b) Perform step 1c to drive the system to shape equilibrium at t^{n+1}.

Remark

Numerically, steady state is considered to be achieved when

$$\Big(\int_{\Omega}\left(\frac{\partial\phi}{\partial\tau}\right)^2 \mathrm{d}v\Big)^{\frac{1}{2}} < \mathrm{tol}_{\phi}, \quad \text{for shape equilibrium,} \tag{6.16a}$$

$$\Big(\int_{\Omega}\left(\frac{\partial c}{\partial t}\right)^2 \mathrm{d}v\Big)^{\frac{1}{2}} < \mathrm{tol}_{c}, \quad \text{for species transport,} \tag{6.16b}$$

$$\Big(\int_{\Omega}\left(\frac{\partial c}{\partial\tau}\right)^2 \mathrm{d}v\Big)^{\frac{1}{2}} < \mathrm{tol}_{\mathrm{adv}}, \quad \text{for data extension.} \tag{6.16c}$$

For the numerical examples presented in Chapter 7, values of 0.1 for tol_ϕ and 0.01 for tol_c and tol_{adv} were found to provide an adequate representation of steady state.

6.7 Summary

This Chapter presents several aspects of the numerical modeling of vesicles that are described within the continuum framework outlined in Chapter 4. The governing equations are spatially discretized with a uniform cubic B-spline basis. While a semi-implicit scheme based on the convexity splitting technique is used for temporal discretization of the equation of shape equilibrium, the species transport equation is modeled with a fully implicit backward-Euler time stepping scheme. A modified data extension technique is employed to prepare the initial condition for concentration distribution. As both species transport and shape change are described in an Eulerian framework, data extension is also used to approximately tie the band of concentration to the deforming surface of the vesicle. The hyperbolic wave equation used to model data extension is cast in a finite element framework and stabilized using the SUPG method, details of which are also presented. Finally, a computational scheme to enforce shape equilibrium at all stages of species transport is outlined.

7

Numerical Results and Discussion

7.1 Overview

Axisymmetric equilibrium shapes of single component vesicles for different values of the control parameters (reduced volume and spontaneous curvature) are presented in the first Section of this Chapter. The governing equations of shape equilibrium for single component vesicles is dependent only on the curvature energy and the geometric constraints. Vesicles composed of binary phases are studied using several axisymmetric, two-dimensional and three-dimensional numerical examples. The chemo-mechanical model discussed in Chapters 4 and 6 is used to simulate the multi-component vesicles.

The entire finite-element code with a cubic spline basis was developed in Matlab and employs some of the parallel processing capabilities available within Matlab. The sparse linear-algebraic system of equations are unsymmetric and are solved using Matlab's built-in direct solver UMFPACK, which stands for an unsymmetric multi-frontal sparse LU factorization package (Davis, 2004b,a; Davis and Duff, 1999, 1997). For three-dimensional problems, we use an external solver PARDISO version 4.1.2 (Schenk et al., 2008, 2007) to solve the large sparse systems in parallel. The Matlab

interface for PARDISO has been developed by Carbonetto (2009). Post-processing is performed using the open source visualization software Paraview (Henderson, 2007).

Computation of the normal distance of a point from the surface of an ellipse in two dimensions and an ellipsoid in three dimensions is a non-trivial task. We employ a slightly modified verison of the Matlab routine available in the public domain (Oldenhuis, 2010), which is based on an algorithm described in Kim (2006).

7.1.1 Parameters of the chemo-mechanical model

The dimensionless flexural rigidity κ, spontaneous curvature $H_{\rm sp}$ and the parameters ϵ_c and χ, that influence line tension, must be estimated based on experimental measurements. Accurate experimental determination of these parameters can be challenging and is even today a subject of extensive research for vesicles with coexisting phases. As an example, measurements of absolute values of bending stiffness of domains of phase separated lipid membranes do not exist (Tian et al., 2007). While mechanical properties of multi-phase bilayers depend on the composition of the coexisting domains, estimates for the properties are available only for average compositions (Veatch et al., 2004). Further, though estimates of line tension do exist, it is found to be very sensitive to the levels of cholesterol content (Tian et al., 2007).

Our current focus is to qualitatively study the effect of the material parameters on the coupled phenomenon of species transport and shape equilibrium. Accordingly, κ and $H_{\rm sp}$ of each phase are chosen relative to their values in the other phase. The dimensionless interface thickness ϵ_c is chosen to be small relative to the vesicle dimensions.

Numerical examples simulating the coupled model use concentration dependent dimensionless flexural rigidity κ and spontaneous curvature $H_{\rm sp}$. To exaggerate the difference in the flexural rigidities and spontaneous curvatures of the two phases, an

exponential variation with concentration is assumed:

$$\kappa(c) = \exp(a_\kappa\, c + b_\kappa), \tag{7.1a}$$

$$H_{\text{sp}}(c) = \exp(a_H\, c + b_H). \tag{7.1b}$$

The parameters (a_κ, b_κ) and (a_H, b_H) are estimated based on the values of κ and H_{sp} in the phases corresponding to c_a and c_b. A small value of order 1.0×10^{-16} is used to approximate $H_{\text{sp}} = 0$.

Unless mentioned otherwise, all examples employ a Flory–Huggins type double-well potential with the interaction parameter $\chi = 2.25$ and, thus, with minima $c_a \approx 0.2244$ and $c_b \approx 0.7756$ distinguishing the phases. Notice that this potential takes negative values on the interval $(0, 1)$. This is of no physical consequence, and does not affect the solution of the species transport equations. However, it can have an adverse effect during the numerical solution of the governing equations for shape equilibrium (4.33) and (4.34). It can be noted that the chemical energy density, and hence the double-well potential, directly enter the Euler–Lagrange form for shape equilibrium associated with line-tension energy (4.33a). Negative values for $f_{\text{F–H}}$ can result in an indefinite tangent stiffness matrix and lead to numerical difficulties. An additive constant is included in the double-well potential to overcome this issue. The magnitude of the additive constant is chosen so that the minima of a symmetric potential have a value of zero. The shifted potential used in the present study is shown in Figure 7.1.

7.1.2 Monitoring species conservation and the zero-flux constraint

At any stage of species transport, the area occupied by species α on the surface of the vesicle is evaluated as

$$C_\alpha = \int_\Omega c\delta_s \, \mathrm{d}v. \tag{7.2}$$

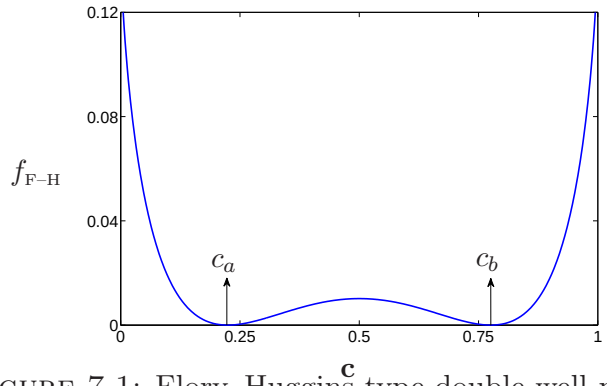

FIGURE 7.1: Flory–Huggins type double well potential

In numerical studies involving two species, the value of C_α is tracked and used to quantify the extent to which the lipid species are conserved. Further, satisfaction of the zero-flux constraint (4.31) in a neighborhood of the surface is monitored by the L_2 norm via

$$e_{\text{f}} = \Big(\int_{\Omega} (\nabla c \cdot \mathbf{n})^2 \, \delta_S \, \mathrm{d}v \Big)^{\frac{1}{2}}. \tag{7.3}$$

7.1.3 Dimensionless interface thickness and penalty parameters

Unless mentioned otherwise, all examples use $\epsilon_\phi = 0.04$ and $\epsilon_c = 0.04$ while the vesicle dimensions are of $O(1)$. The following values for penalty parameters are found to enforce the geometric constraints quite accurately: $\alpha_v = 10^4$ and $\alpha_a = 10^3$. The zero-flux constraint (4.32) is imposed with $\alpha_m = 10^4$.

7.1.4 Grid size

It is acknowledged that numerical solutions of embedded interface problems, such as those studied in this work, are computationally more accessible by using a non-uniform grid having a sufficiently higher refinement as the interface is approached. A spline basis in multiple dimensions is obtained as a tensor product of the one-dimensional basis. This necessitates a purely rectangular grid that cannot be refined

locally in regions of embedded interfaces modeling a closed surface. Although hierarchical adaptive schemes provide the opportunity to locally refine a spline basis, this is still an active area of research. In the present work, a uniform cubic spline basis is employed. The grid size for the basis is chosen so as to obtain a sufficiently accurate representation of the phase field ϕ and the approximate delta function δ_S. For the sake of comparison, the L_2 error norms for the phase field ϕ and δ_S for different grid-widths are given in Table 7.1.

Table 7.1: Grid refinement study.

Grid size h	L_2 error norm ϕ	δ_S
ϵ_ϕ	5.64×10^{-6}	1.19×10^{-4}
$\epsilon_\phi/2$	6.57×10^{-8}	4.14×10^{-6}
$\epsilon_\phi/3$	5.99×10^{-9}	6.29×10^{-7}

Further, the resolution obtained for δ_S can be indirectly verified by computing the surface area of a closed surface in 3D or the perimeter of a closed curve in 2D using (3.51). As an example, a circle of radius 0.8 units is represented with a phase field ϕ and $\epsilon_\phi = 0.04$. The relative errors in computed values of the circumference for different grid sizes are provided in Table 7.2.

Table 7.2: Relative errors in computed perimeter of an embedded circle.

Grid size h	Absolute Relative error %
ϵ_ϕ	6.85×10^{-5}
$\epsilon_\phi/2$	4.54×10^{-5}
$\epsilon_\phi/3$	4.20×10^{-6}

To achieve a reasonable balance between accuracy and computational expense, we employ a uniform cubic spline basis with a grid size chosen to be the smaller of $\epsilon_\phi/2$ and $\epsilon_c/2$, for all numerical examples.

7.1.5 Time increments and time stepping

While solving the gradient-flow augmentation (4.34) of the shape equilibrium equation, pseudo-time increments are taken to be in the interval $[10^{-7}, 10^{-3}]$ for two- and three-dimensional numerical examples with multiple phases. Axisymmetric examples simulating single component vesicles are modeled with a uniform pseudo-time increment of 10^{-4} while the example with dominant line tension is modeled with a uniform time increment of 10^-5. Data extension is performed with a uniform pseudo-time step of 10^{-2}. Dimensionless time increments for species transport are taken to be in the range $[10^{-8}, 10^{-1}]$ except for the numerical example discussed in Section 7.4.3, where time steps of the order of 10^4 are used to model the extremely slow coarsening stage.

All numerical examples employ an adaptive time stepping scheme while solving the nonlinear equations of shape equilibrium (4.34) and species transport (4.30). The adaptivity is heuristically controlled such that fast convergence (< 3 iterations) leads to a 50% increase in the time-step size while divergence is treated with an equivalent reduction in the time increment. Slow convergence (> 5 iterations) does not alter the time-step size. Further, a maximum permissible time increment is used to prevent frequent divergence of the Newton–Raphson method.

7.2 Stationary shapes of single component vesicles

In this section, we verify the model against established equilibrium shapes of axisymmetric single component vesicles which have been studied extensively by Seifert et al. (1991). Stationary shapes for a range of reduced volume $\mathrm{v_r}$ are depicted in

Figure 7.2 for $H_{\rm sp} = 0$ and $H_{\rm sp} = 3$, respectively.

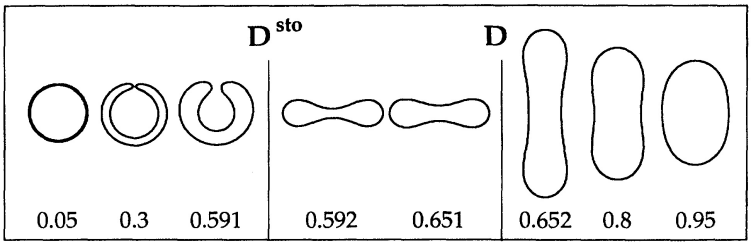

(a)

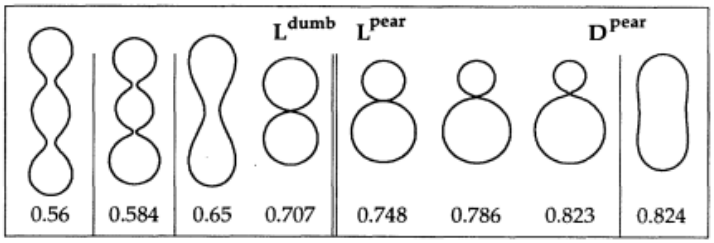

(b)

FIGURE 7.2: Stationary shapes of single component vesicles for various values of the reduced volume v_r for (a) $H_{\rm sp} = 0$ and (b) $H_{\rm sp} = 3$ (Seifert et al., 1991).

7.2.1 Axisymmetric vesicles with zero spontaneous curvature ($H_{sp} = 0$)

For all examples in this section, κ is set equal to unity and $H_{\rm sp} = 10^{-16}$.

CASE I ($v_r = 0.60$): The initial shape of the vesicle is taken to be an oblate spheroid, a sectional view of which is shown in Figure 7.3(a). The spheroid has a semi-major and semi-minor axes of dimensionless lengths 1.0 and 0.26, resulting in a reduced volume of approximately 0.60. For the given reduced volume, the equilibrium configuration should resemble a bi-concave disc (Seifert et al., 1991). Figure 7.3(b) shows a sectional view of the corresponding vesicle configuration at equilibrium. Typically, red blood cells have a reduced volume in this range and display the shape of a bi-concave disc as shown in Figure 7.3(c).

CASE II ($v_r = 0.71$): The initial shape of the vesicle is taken to be a prolate spheroid shown as a sectional view in Figure 7.4(a). The spheroid has a semi-major and

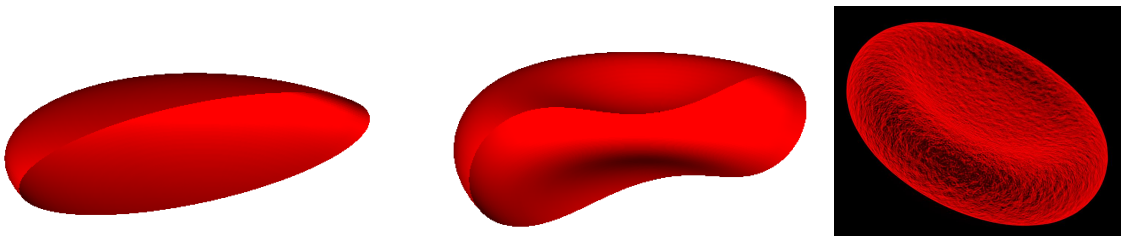

(a) (b) (c)

FIGURE 7.3: Sectional view of (a) initial and (b) equilibrium shapes of a vesicle with a reduced volume of approximately 0.6, $\kappa = 1.0$, and $H_{\text{sp}} = 1.0 \times 10^{-16}$. (c) Image of a human red blood cell (Ivanyik, 2007)

semi-minor axes of dimensionless lengths 2.0 and 0.5, resulting in a reduced volume of approximately 0.71. The equilibrium configuration of such a vesicle is known to resemble the shape of a peanut. A sectional view of the corresponding vesicle configuration at equilibrium is shown in Figure 7.4(b). Experimentally observed prolate bilayer vesicles (Yanagisawa et al., 2008) are shown in Figure 7.4(c).

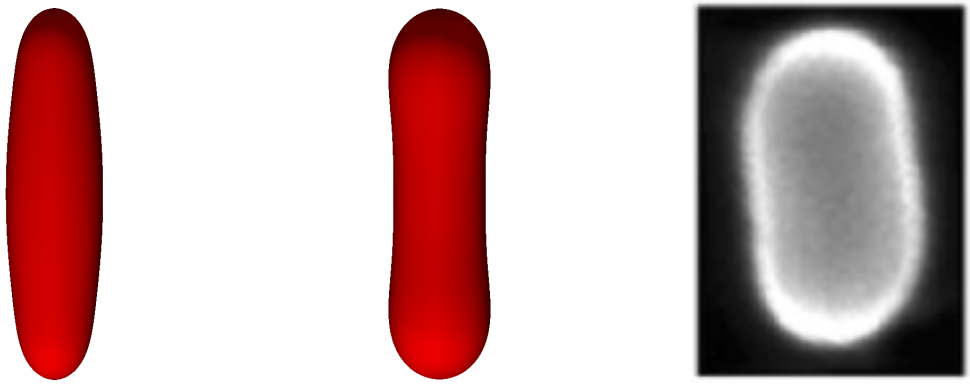

(a) (b) (c)

FIGURE 7.4: Sectional view of (a) initial and (b) equilibrium shapes of a vesicle with $\text{v}_\text{r} = 0.71$, $\kappa = 1.0$, and $H_{\text{sp}} = 1.0 \times 10^{-16}$. (c) Experimentally observed prolate vesicle (Yanagisawa et al., 2008).

CASE III ($\text{v}_\text{r} = 0.45$): The initial shape of the vesicle is built from sectors of concentric circles with a cap at away from the axisymmetric end. The sectional view of the surface of revolution of such a shape is shown in Figure 7.5(a). The closed

surface of revolution has a reduced volume of approximately 0.45. The equilibrium configuration of such a vesicle is known to resemble the shape of a stomatocyte. A sectional view of the corresponding vesicle configuration at equilibrium is shown in Figure 7.5(b). Stomatocyte shapes are found in diseased red blood cells and have also been observed in experimental bilayer vesicles (Yanagisawa et al., 2008) as shown in Figure 7.5(c).

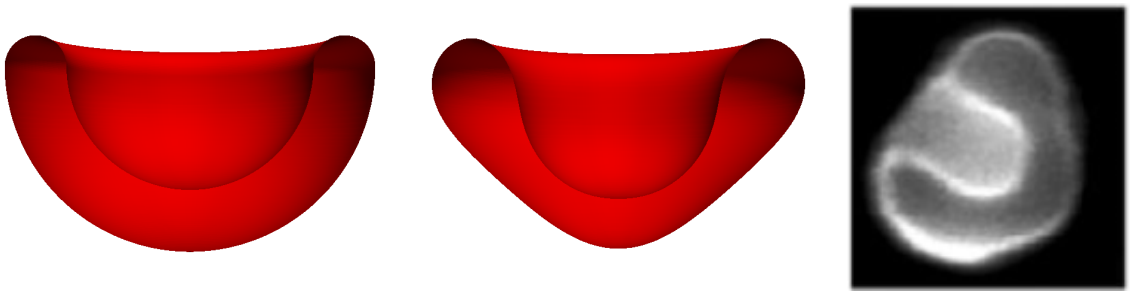

(a) (b) (c)

FIGURE 7.5: Sectional view of (a) initial and (b) equilibrium shapes of a vesicle with $v_r = 0.45$, $\kappa = 1.0$, and $H_{sp} = 1.0 \times 10^{-16}$. (c) Experimentally observed stomatocyte vesicle (Yanagisawa et al., 2008).

7.2.2 Axisymmetric vesicles with a non-zero spontaneous curvature ($H_{sp} = 3$)

The examples in this section are set with $\kappa = 1$ and $H_{sp} = 3.0$. The initial configurations of the surface is built with an asymmetry about the horizontal axis to allow for possible asymmetries in the equilibrium shapes.

CASE I ($v_r = 0.78$): The initial shape of the vesicle is built from part ellipse and part cylindrical section. The bottom half is constructed with a cylindrical section of radius 0.5 and height 1.5. The top half consists of a half-ellipse with semi-minor axis 0.5 and semi-major axis 1.5 and connects smoothly to the bottom half. The sectional view of the surface of revolution of such a shape is shown in Figure 7.6(a). The resulting reduced volume of this surface of revolution is approximately 0.78. The equilibrium configuration for the given values of H_{sp} and v_r is asymmetric with two spherical

sections joined by a narrow neck as shown in Figure 7.6(b). This configuration is seen to closely resemble the corresponding shape predicted in (Seifert et al., 1991).

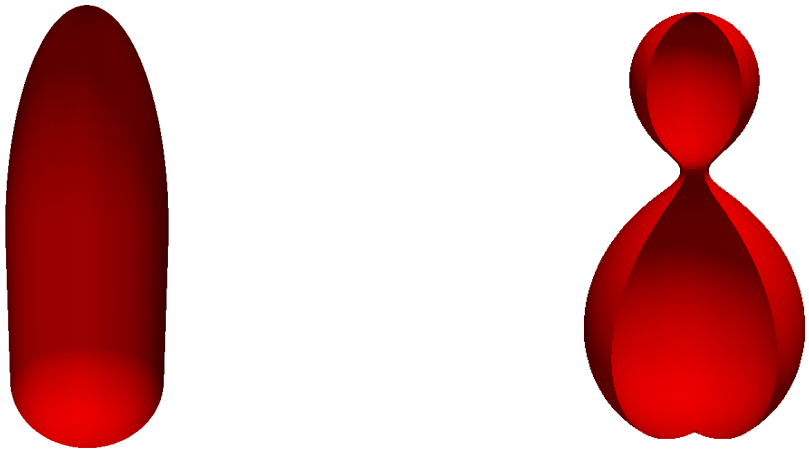

(a) (b)

FIGURE 7.6: Sectional view of (a) initial and (b) equilibrium shapes of a vesicle with a reduced volume of approximately 0.6, $\kappa = 1.0$, and $H_{sp} = 1.0 \times 10^{-16}$.

CASE II ($v_r = 0.578$): Similar to CASE I, the initial shape of the vesicle is built from part ellipse and part cylindrical section. The radius of the cylindrical section, which is the same as the semi-minor axis of the half-ellipse is taken to be 0.5. The height of the cylindrical section, which is equal to the semi-major axis of the half-ellipse is taken to be 5.0. The surface of revolution resulting from this shape is shown in Figure 7.7(a) and has a reduced volume of 0.578. The equilibrium configuration consists of three distinct regions connected by necks, as shown in Figure 7.7(b). Again, this configuration is seen to closely resemble the corresponding shape predicted in (Seifert et al., 1991).

In all the above simulations, the numerical solution is found to have relative errors in the internal volume and surface area between 0.5% and 1.0% at equilibrium. These errors can be further reduced by using a smaller time increment or by employing a higher-order time-stepping scheme.

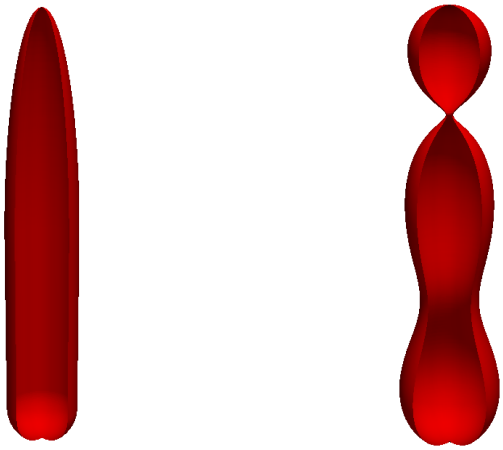

(a) (b)

FIGURE 7.7: Sectional view of (a) initial and (b) equilibrium shapes of a vesicle with $v_r = 0.71$, $\kappa = 1.0$, and $H_{sp} = 1.0 \times 10^{-16}$.

7.3 Axisymmetric vesicle: shape change dominated by line tension

The initial shape of the vesicle is taken to be a prolate spheroid with a semi-major and semi-minor axes of dimensionless lengths 1.0 and 0.7. To ensure the dominance

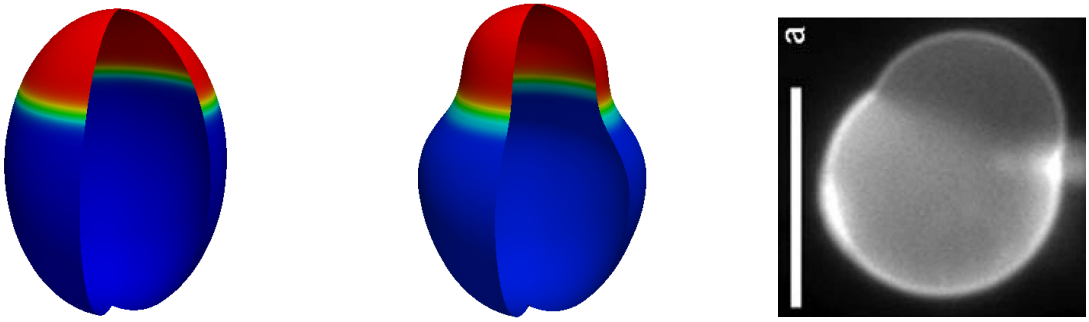

(a) (b) (c)

FIGURE 7.8: Sectional view of (a) initial and (b) equilibrium shapes of a phase separated vesicle with $\kappa = 1.0$ and $H_{sp} = 1.0 \times 10^{-16}$. Regions in blue and red correspond to phases a and b respectively. (c) Experimentally observed budding induced by line tension (Veatch and Keller, 2003).

of line tension, the interaction parameter in the double-well potential is here taken to be $\chi = 4.0$. This raises the energy barrier between the phases and moves the

wells of the potential to $c \approx 0.0212$ and $c \approx 0.9788$. An asymmetric phase-separated state is used for the initial concentration distribution, as depicted in Figure 7.8(a). The dimensionless flexural rigidity κ is set equal to unity and the dimensionless spontaneous curvature is set to vanish. Shape change is thus driven mainly by line tension. Figure 7.8(b) shows the equilibrium shape of the vesicle, which is suggestive of budding. Similar budding transformations in experimental vesicles with binary phases have been observed (Veatch and Keller, 2003) as shown in Figure 7.8(c). For the current numerical example, relative errors in internal volume, surface area, and C_α are between 1% and 5% at equilibrium.

7.4 Stationary shapes and chemo-mechanical coupling in two-dimensional examples with a binary mixture

The surface of the vesicle is represented by a closed curve for two-dimensional numerical examples. As only a single curvature is defined at any point on a closed curve, the approximation for the dimensionless mean curvature becomes

$$H_\phi \approx \frac{1}{|\nabla\phi|}\left(\Delta\phi + \frac{\phi(1-\phi^2)}{\epsilon_\phi^2}\right), \tag{7.4}$$

which is twice that of the mean curvature of a surface given by (4.25).

7.4.1 Phase separated vesicle in 2D

In this example, the vesicle is taken to be elliptical with semi-major and semi-minor axes of dimensionless lengths 1.5 and 0.4. The lipid species on the surface are taken to be in a phase separated state. Each phase is assumed to cover 50% of the vesicle. The dimensionless flexural rigidities of the two phases are taken to be $\kappa(c_a) = 1.0$ and $\kappa(c_b) = 10.0$. The dimensionless spontaneous curvature is assumed constant, with $H_{sp} = 1.75$. Figure 7.9 shows the progress of shape change towards equilibrium. Phase b, with a larger flexural rigidity, controls the vesicle shape. Close to the

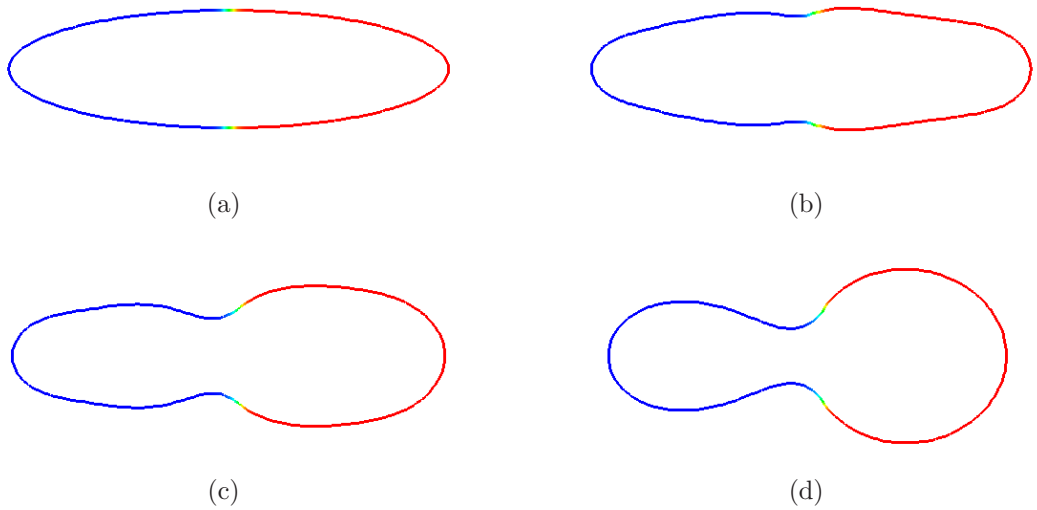

FIGURE 7.9: (a) is the initial phase separated state with phase a depicted in blue and phase b in red. (b) and (c) are intermediate stages of evolution and (d) is the final equilibrium state; $\kappa(c_a) = 1.0$, $\kappa(c_b) = 10.0$ and $H_{\text{sp}} = 1.75$.

interface separating the phases, phase a conforms to the curvature of phase b. As a result, the neck forms slightly away from the interface. An asymmetric configuration develops as a result of the asymmetric distribution of flexural rigidities. At equilibrium, the relative errors in internal volume, surface area, and C_α are 0.05%, 0.34%, and 0.02% respectively.

7.4.2 Spinodal decomposition and coarsening in 2D

The elliptical vesicle, with semi-major and semi-minor axes of dimensionless lengths 1.0 and 0.40, starts with a random initial distribution of concentration about a mean value $\bar{c} = 0.50$, which lies in the spinodal region of the double-well potential. While the dimensionless flexural rigidity is assumed constant and equal to unity, the dimensionless spontaneous curvatures are taken to be $H_{\text{sp}}(c_a) = 1.0$ and $H_{\text{sp}}(c_b) = 3.0$. The dimensionless species mobility is also assumed to be constant and equal to unity. Each configuration in Figure 7.10 shows the vesicle in shape equilibrium for the particular spatial distribution of concentration. An interesting feature of

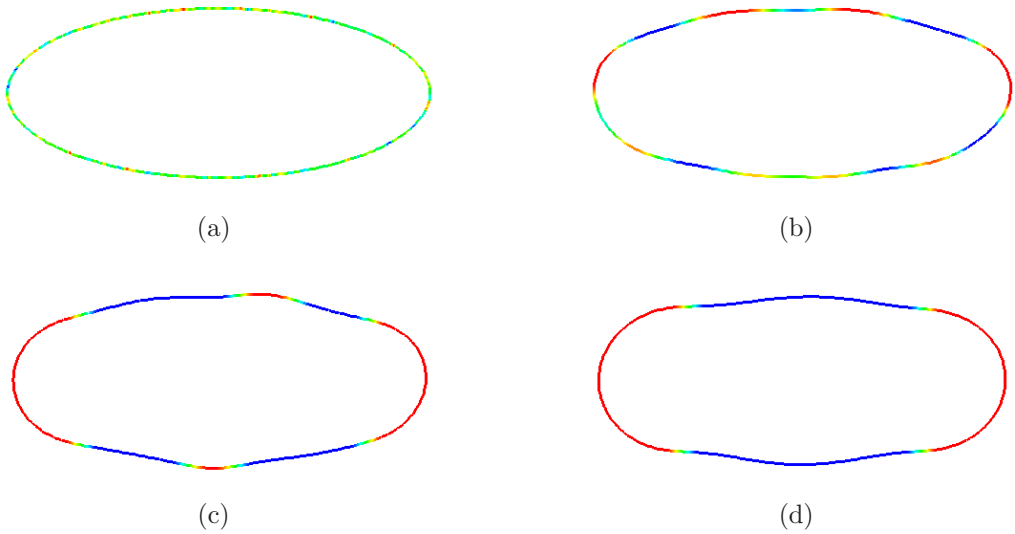

FIGURE 7.10: (a) is the initial random state with a mean value $\bar{c} = 0.5$ of concentration in the spinodal region, (b) and (c) are intermediate stages of evolution and (d) is the final equilibrium state. In this example, $\kappa = 1.0$, $H_{\text{sp}}(c_a) = 1.0$ and $H_{\text{sp}}(c_b) = 3.0$. Regions in blue and red correspond to phases a and b respectively.

the evolution is the curvature-dependent domain sorting. Species reorganize on the surface in such a way that phase b moves towards the higher curvature regions of the geometry while phase a accumulates in regions with relatively low curvature. The final configuration, as depicted in Figure 7.10(d), shows a state of shape and chemical equilibrium. It is noted that species transport uncoupled to curvature elasticity would have resulted in a continuous distribution of each phase with only two phase boundaries instead of four as shown in Figure 7.10(d). While the relative error in the internal volume and surface area of the vesicle are 0.01% and 0.22%, the relative error in C_α is 0.29%. Figure 7.11 shows the concentration distribution over the entire computational domain during different stages of evolution, corresponding to Figures 7.10. The evolving curve along the band represents the vesicle and is the zero level-set of the phase-field ϕ. At all stages of evolution, species transport is primarily tangent to the surface. The pointwise constraint (4.31) enforces the distribution of concentration to remain constant along the surface normal. The magnitude of e_{f} is

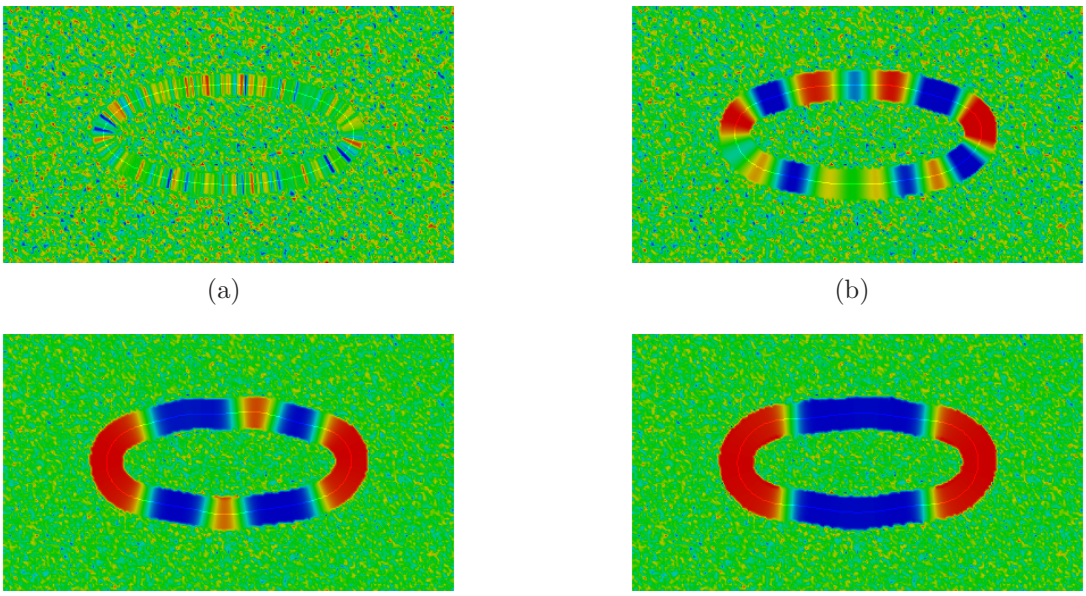

(a) (b)

(c) (d)

FIGURE 7.11: Concentration distribution shown over the entire computational domain at different stages of evolution. The parameter values are the same as those appearing in the caption of Figure 7.10.

found to decrease from 3.8×10^{-4} at the initial state to 4.6×10^{-6} at equilibrium. Approximation of the zero-flux condition is thus found to be satisfactory throughout the evolution process. Figure 7.12 depicts the variation of the curvature energy, line tension energy, and net energy (i.e., the sum of the curvature and line tension energies) with dimensionless time. All points during the evolution represent states of shape equilibrium. Line tension energy dominates the evolution to equilibrium. In contrast, the curvature energy remains almost constant. As expected, the net energy decreases monotonically.

7.4.3 Evolution from a partially phase separated stage

An elliptical vesicle with the same initial dimensions as discussed in Section 7.4.2 is used in the present example. The dimensionless mobility is assumed equal to unity. The initial distribution of phases is depicted in Figure 7.13(a). The dimensionless flexural rigidities are taken to be $\kappa(c_a) = 0.1$ and $\kappa(c_b) = 1.0$, while the dimensionless

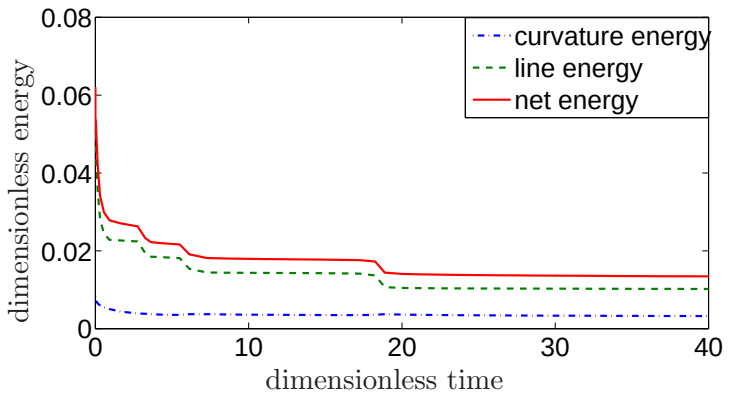

FIGURE 7.12: Evolution of the energetic components for the coupled problem discussed in Section 7.4.2.

spontaneous curvatures are taken to be $H_{\rm sp}(c_a) = 1.0 \times 10^{-16}$ and $H_{\rm sp}(c_b) = 4.2$. The initial distribution of the phases and the dimensionless parameters are selected to render budding energetically favorable. The present example is intended to illustrate the effect of the difference in time scales during the nonlinear evolution.

Numerical results for the coupled shape and species transport are given in Figure 7.13. Instantaneous shape equilibrium results in a configuration with asymmetric budding as shown in Figure 7.13(b). A large negative curvature at the neck can energetically penalize further coarsening associated with phase b in the bud. Species transport following budding is mainly restricted to the remaining portion of the vesicle, and is not significantly affected by the bud. In contrast, if shape change occurs on a time scale comparable to species transport, bud formation does not precede species transport and, consequently, coarsening need not be restricted to regions of the vesicle as observed here. Further, the time required to reach chemical equilibrium and the resulting equilibrium configuration can be markedly different.

Additionally, as shown in Figure 7.13(b), phase b forms smaller buds that appear as slight bulges on the remaining portions of the vesicle. Since the transition layers between the buds and the surrounding regions of phase a involve large curva-

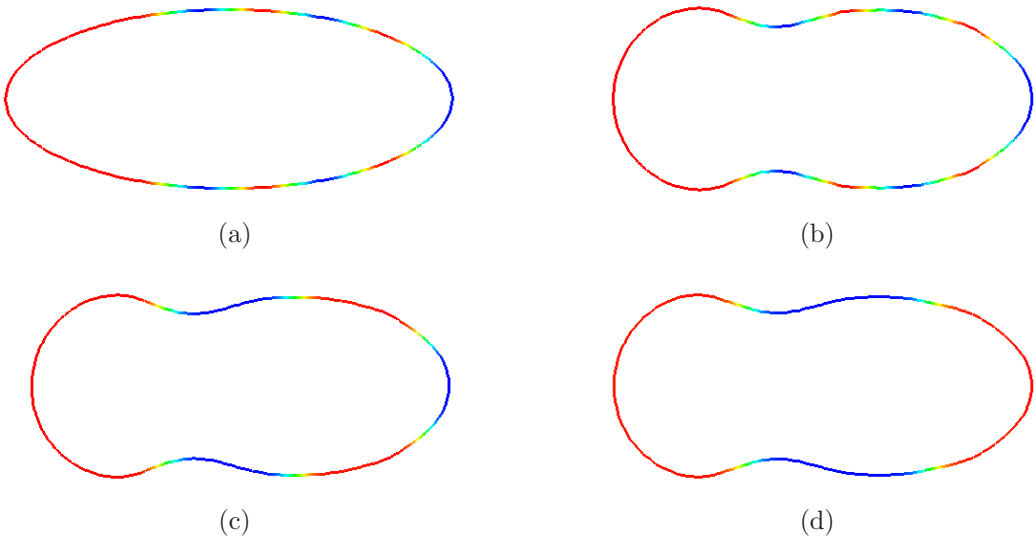

FIGURE 7.13: (a) Initial configuration of the vesicle. (b) Initial configuration driven to shape equilibrium; this state corresponds to a dimensionless time $t = 0$ in Figure 7.14. (c) Intermediate stage of evolution that corresponds to a dimensionless time of $t \approx 10^2$ in Figure 7.14. (d) Final equilibrium state corresponding to a dimensionless time of $t \approx 10^6$ in Figure 7.14. For this example, $\kappa(c_a) = 0.1$, $\kappa(c_b) = 1.0$, $H_{\text{sp}}(c_a) = 1.0 \times 10^{-16}$ and $H_{\text{sp}}(c_b) = 4.2$. Regions in blue and red represent phases a and b, respectively.

ture changes, eventual coarsening of the phases can proceed slowly. The coarsened stage in Figure 7.13(d) corresponds to a dimensionless time of $t \approx 10^6$. In contrast, numerical simulations of species transport from the same initial condition, as depicted in Figure 7.13(a), but with no associated shape change, reveal that chemical equilibrium is reached by $t \approx 10^2$. A comparison of the time required to reach chemical equilibrium in both cases suggests a delayed coarsening due to curvature effects. Qualitatively similar observations have been recorded by Yanagisawa et al. (2007), where the authors refer to '*trapped coarsening*' due to the formation of buds. However, in that study, budding is caused mainly by line tension.

The energy evolution plot in Figure 7.14 depicts major coarsening stages by drops in the line energy. Each decrease in the line energy occurs over several time increments. The first major decrease in energy corresponds to the merging of the

smaller pairs of regions associated with phase b, as depicted by the evolution from Figure 7.13(b) to Figure 7.13(c). Similarly, the next major decrease in energy corresponds to the coarsening stage illustrated by the evolution from Figure 7.13(c) to Figure 7.13(d).

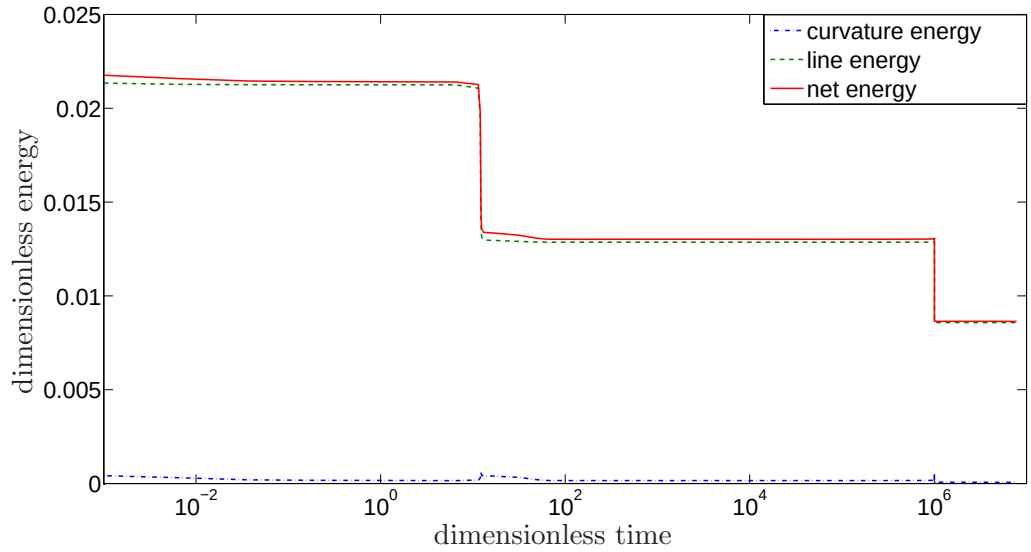

FIGURE 7.14: Evolution of the energetic components for the example discussed in Section 7.4.3. The dimensionless time is plotted on a logarithmic scale.

For the present numerical example, at equilibrium, the relative errors in internal volume, surface area, and C_α are 0.01%, 0.05%, and 0.04%, respectively. Further, e_{f} is found to decrease from 8.7×10^{-4} at the initial state to 7.5×10^{-6} at equilibrium, thus ensuring satisfactory approximation of the zero-flux condition (4.31) throughout the evolution process.

In stages where the energy evolution profile is almost flat, dimensionless time increments of up to 10^4 are used for species transport. Such large time increments during the coarsening stage are found not to adversely affect the quality of the numerical solution. This was verified by comparing the numerical solution at a particular non-dimensional time during the coarsening stage using uniform time increments that differ by orders of magnitude.

7.5 Stationary shapes and chemo-mechanical coupling in three-dimensional examples with a binary mixture

Both the examples in this section use an interaction parameter in the double-well potential to be $\chi = 4.0$ with the corresponding double-well minima at $c \approx 0.0212$ and $c \approx 0.9788$.

7.5.1 Spherical vesicle with circular domains on the surface

The initial shape of the vesicle is taken to be a sphere of radius 0.8 units. Circular domains of phase b with an approximate radius of 0.27 units are assumed to be distributed in a matrix of phase a. The distribution of the circular domains of phase b are taken to be identical in each octant of the sphere. Curvature-driven and line tension driven motions occur along the surface normal and thus, for the assumed initial distribution, shape changes can be considered to be identical in each octant of the sphere. Only one octant of the sphere is modeled to save on computational costs. Symmetry boundary conditions $\nabla\phi \cdot \mathbf{n}_{\text{face}} = 0$ are imposed using a penalty approach on the three inner faces of the octant. Here $\mathbf{n}_{\text{face}}$ is the normal to the corresponding faces. The first octant of the sphere is a cubic domain with each side measuring 1.3 units. With $\epsilon_\phi = 0.04$ and a uniform grid size of $h = 0.0217$, the system consists of $216,000$ cubic B-spline elements resulting in $250,047$ degrees of freedom.

The initial configuration with circular domains of one phase distributed in a matrix of another phase is commonly observed in experiments with giant unilamellar vesicles (Baumgart et al., 2003; Yanagisawa et al., 2007), though the vesicles are known to deviate from being perfectly spherical. The distribution is realized experimentally by forming vesicles with a ternary mixture of lipids and cholesterol, and inducing spinodal decomposition by reducing the temperature below the transition temperature. Shape changes associated with such a distribution of phases is simulated in this example. The flexural rigidity of phase a and phase b are taken to be in

the ratio 1 : 4. The spontaneous curvature of phase a is taken to match the curvature of the sphere $H_{\rm sp}(c_a) = 1.25$, while phase b is assumed to have $H_{\rm sp}(c_b) = 5$.

A sphere represents a minimum in terms of the surface area enclosing a prescribed volume. Thus, a perfectly spherical vesicle with constraints on volume and surface area cannot undergo any shape change. In this example, no geometric constraints are imposed, so as to allow for shape changes. This approximates experiments where the shape of the vesicle is a slight deviation from a sphere (for a given volume, the vesicle has excess surface area in comparison to a perfect sphere of the same volume).

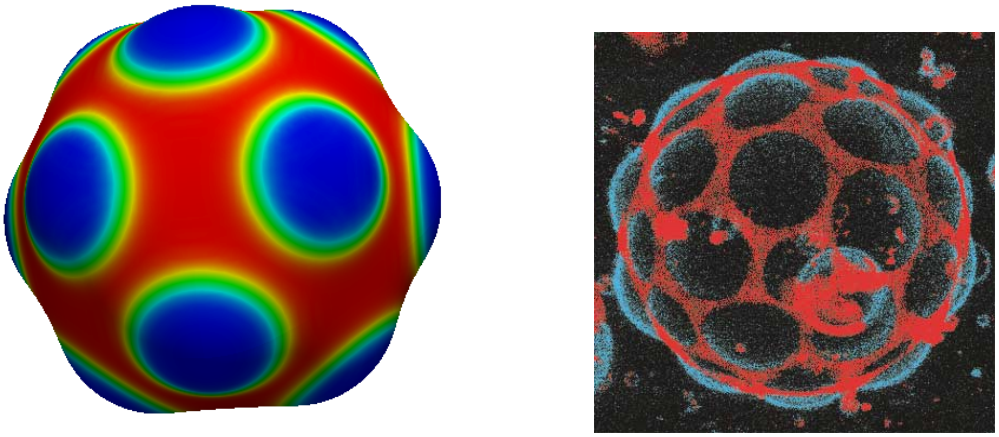

(a) (b)

FIGURE 7.15: (a) Equilibrium shape of a partially phase-separated spherical vesicle. For this example, $\kappa(c_a) = 1.0$, $\kappa(c_b) = 4.0$, $H_{\rm sp}(c_a) = 1.25$ and $H_{\rm sp}(c_b) = 5.0$. Regions in red and blue correspond to phases a and b respectively. (b) Experimentally observed bud formation in a nearly spherical binary vesicle (Baumgart et al., 2003).

Driving the system to shape equilibrium results in the formation of buds of phase b as shown in Figure 7.15(a). Results on the complete sphere have been obtained by reflecting the results in the octant along the three coordinate planes. A qualitative similarity is seen in experimental results given in Baumgart et al. (2003); Yanagisawa

et al. (2007) and is shown in Figure 7.15(b). In the present numerical example, buds are formed mainly by driving phase b towards its natural curvature and by allowing the corresponding increase in the vesicle surface area. Buds can similarly be formed by mainly minimizing the line tension energy. This can be numerically simulated by ensuring that the line tension energy is significantly larger than the curvature energy of the vesicle.

7.5.2 Evolution from a partially phase-separated stage

The initial geometry of the vesicle is taken to be a prolate ellipsoid with a semi-major axis of 0.8 units and the semi-minor axes measuring 0.4 units. The distribution of domains on the ellipsoidal surface is constructed as described below.

A large domain of phase b occupies the left region of the ellipsoid accounting for 40% length along the major axis. This smoothly transitions to a region of random distribution of phases with the concentration ranging from $c = 0.1$ to $c = 0.5$ having a mean of $\bar{c} = 0.3$. The system is then driven by pure species transport for several increments up to a dimensionless time of $t = 1.25 \times 10^{-3}$. The distribution of phases a and b evolve as shown in Figure 7.16.

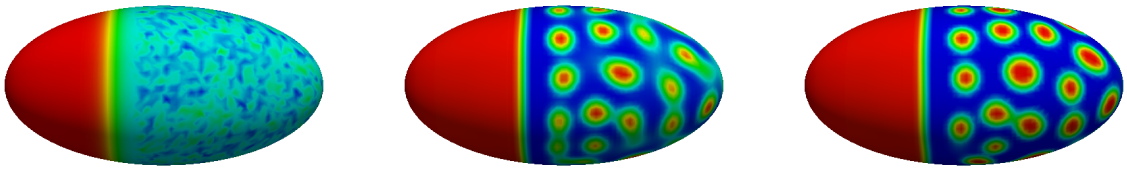

(a) (b) (c)

FIGURE 7.16: Stages of phase separation on an ellipsoidal vesicle at dimensionless times (a) $t = 0$, (b) $t = 6.5 \times 10^{-4}$ and (c) $t = 1.25 \times 10^{-3}$.

For shape evolution, the initial distribution of phases is given in Figure 7.16(c). The flexural rigidities of phase a and phase b are taken to be in the ratio $1 : 4$. The spontaneous curvature of phase a is taken to be $H_{\text{sp}}(c_a) = 10^{-16}$, while phase b is

assumed to have $H_{\text{sp}}(c_b) = 4$. As discussed in Section 7.4.3, the initial distribution of the phases and the dimensionless parameters are selected to render budding energetically favorable. The present example is intended to illustrate the effect of the difference in time scales associated with shape change and species transport.

The ellipsoid is embedded in a three-dimensional rectangular domain measuring $1.2 \times 0.8 \times 0.8$ units. This numerical example consists of $514,500$ three-dimensional cubic B-spline elements and 575532 degrees of freedom.

The progress to shape equilibrium is shown in Figure 7.17. A combination of

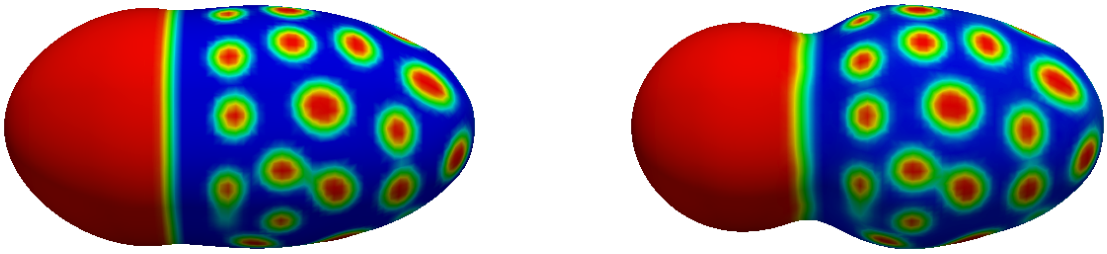

(a) (b)

FIGURE 7.17: Evolution of shape change of an ellipsoidal vesicle from an initial state depicted in Figure 7.16(c). For this example, $\kappa(c_a) = 1.0$, $\kappa(c_b) = 4.0$, $H_{\text{sp}}(c_a) = 1.0 \times 10^{-16}$ and $H_{\text{sp}}(c_b) = 4$. Regions in blue and red represent phases a and b, respectively.

minimizing curvature energy and line tension energy leads to the formation of a large bud of phase b. Figure 7.17(b) depicts a precursor to budding. Shape changes being instantaneous, excess line tension can lead to the fission of the large bud before species transport continues on the remaining regions of the mother vesicle.

8

Conclusions and Future Work

We summarize the conclusions and contributions of this work relating to the chemo-mechanical modeling of vesicles and the numerical strategies employed. We further list possible avenues of future research in both the categories.

8.1 Continuum Modeling of Vesicles

8.1.1 Conclusions

A continuum chemo-mechanical model is employed to numerically simulate the dynamics of microdomain evolution on the deforming surface of Giant Unilamellar Vesicles. The model focuses on the regime of vesicle dynamics where shape deformation occurs on a much faster time scale than species transport, as suggested by several experiments (Tsafrir et al., 2003; Yanagisawa et al., 2007). Shape changes are assumed to be instantaneous, simulating a condition in which the viscosity of the vesicle membrane and that of the host medium are negligible.

Several axisymmetric, two-dimensional and three-dimensional numerical examples indicate a good qualitative agreement with experimental observations on vesicles. We provide several benchmark examples showing stationary shapes of vesicles

driven purely by curvature elasticity, for different values of the control parameters viz. spontaneous curvature H_{sp} and reduced volume ν. We provide numerical examples to illustrate the two-way interaction of vesicle shape change and species transport resulting in experimentally observed effects that include curvature-dependent domain sorting and line tension dominated shape changes. In particular, the influence of the postulated difference in time scales between species transport and shape change is clearly exhibited using a two-dimensional example discussed in Section 7.4.3. The three-dimensional example discussed in Section 7.5.2 provides a snapshot in time of this phenomenon. Further, the effect of line tension and curvature elasticity on the kinetics of microdomain growth is presented.

8.1.2 Future work

As an initial effort towards modeling stationary vesicle shapes, the present work considers the effect of mean curvature. The role of Gaussian curvature is neglected. While the stationary shapes of single component vesicles are mainly determined by the mean curvature (Gaussian curvature energy is a constant), vesicles with multiple components and phase boundaries are known to be influenced by the energy associated with the Gaussian curvature. Difference in the Gaussian curvature moduli of the phases influence the position of the phase boundary relative to the neck (Baumgart et al., 2005). Inclusion of Gaussian energy can be important to model vesicle budding and fission accurately.

The present work focuses on modeling vesicles suspended in an aqueous medium at rest. The viscosities of both the vesicle membrane and the aqueous medium is assumed to be negligible. Generally, the flow field of vesicles in suspension is observed to be charaterized by low Reynold's number $O(10^{-5})$ (Yanagisawa et al., 2007; Saeki et al., 2005). The Stoke's equation can be used to model vesicles in such a flow field. Further, the hydrodynamics effects of the flow field on the phases distributed on the

vesicle surface can be modeled by employing a convective Cahn–Hilliard equation (Fan et al., 2010). Vesicle shape dynamics will then include a natural time scale governed by the viscosity of the membrane and the aqueous medium.

While the chemo-mechanical model used in this work demonstrates the capability to qualitatively model experimentally observed behavior, a quantitative comparison would be made possible by arriving at the non-dimensional parameters of the model using experimental characterization of the lipid-cholesterol bilayers.

8.2 Numerical Strategy

8.2.1 Conclusions

The chemo-mechanical model is cast in a phase-field framework. The variational form of the resulting fourth-order nonlinear equations are discretized using a spline-based finite-element method. When the equation governing species transport, which is originally defined on a surface, is cast in diffuse-interface form, the late-time numerical solution can suffer from variations in the concentration field c off the zero level-set of ϕ. To circumvent this difficulty, c is maintained constant in the direction of the surface normal by enforcing the zero normal-flux condition (4.31) pointwise in a neighborhood of the surface.

Ensuring shape equilibrium at every stage of species transport necessitates the band of concentration to follow the deforming vesicle. Within the Eulerian framework, this is approximately realized by using a modified version of a data-extension technique commonly employed in level-set techniques. The advection equation employed for data extension is stabilized using the SUPG method.

While the physics demonstrated by the chemo-mechanical coupling in vesicles is numerically demonstrated by two dimensional examples, extension of the model to three dimensions is relatively straightforward. A few simple numerical examples in 3D are also presented. However, the use of a uniform spline basis renders the

diffuse-interface method computationally very expensive.

8.2.2 Future work

The present work employs the phase-field framework which essentially embeds the vesicle surface in a higher dimensional Euclidean space. While this technique has many advantages, it increases the dimension of the problem, necessitating efficient techniques to minimize the cost of obtaining numerical solutions. Higher resolution of the basis is mainly required in a neighborhood of the surface. Unlike a Lagrangian basis, B-spline basis functions can be built only from rectangular grids. Local refinement of such grids inevitably extend to major portions of the computational domain. While hierarchical refinement of B-splines is still an active area of research, recent work (Schillinger and Rank, 2011) shows some promise in this direction.

The coupled equations of shape equilibrium and species transport are solved using a higher-order discretization in space (cubic B-splines) while only a first-order scheme is used in time. The unconditionally gradient-stable semi-implicit convexity-splitting scheme proposed by Eyre (1997) is essentially a first-order scheme. The possibility of deriving higher-order time-accurate schemes with similar properties for both the equations of shape equilibrium and species transport can be evaluated (Gomez and Hughes, 2011; Vollmayr-Lee and Rutenberg, 2003).

The convexity splitting scheme described in Section 6.4 employs the curvature energy to render the energy associated with geometric constraints as purely concave. This scheme works well for cases where the curvature energy dominates or when it is comparable to the chemical energy. However, it can be noted that the concavity of the functional $E_{\mathrm{gc}} - \gamma_1 E_m$ is not ensured in cases dominated by line tension. Unconditional stability is not guaranteed when the terms arising from a non-concave energy functional are treated explicitly. This currently requires a much lower time increment to maintain accuracy of the numerical solution such that the phase-field

structure remains unaltered during the process of shape change. A higher-order time-stepping scheme might help mitigate the issue and accelerate the evolution to shape equilibrium for line tension dominated problems.

Appendix A

Coercivity of Nitsche Forms and Stability Parameter Evaluation

In this section, conditions for coercivity of the Nitsche forms are derived for both second- and fourth-order boundary value problems discussed in Sections 5.3.1 and 5.3.2. We make use of the following definitions of the L_2 norm of a quantity over a domain (Ω) or along a Dirichlet boundary (Γ_d).

$$\| w \| = \left(\int_{\Omega} w^2 \, \mathrm{d}v \right)^{1/2} \tag{A.1a}$$

$$\| w \|_{\Gamma_d} = \left(\int_{\Gamma_d} w^2 \, \mathrm{d}a \right)^{1/2} \tag{A.1b}$$

A.1 Second-order problem

To examine coercivity of the discrete version of the Nitsche bilinear form, $a(w^h, u^h)$, we start by using $w^h \in \mathcal{V}^h$ in place of u^h. For the Poisson equation, the discrete form

of (5.6a) can then be written as,

$$a\left(w^h, w^h\right) = \int_{\Omega} \nabla w^h \cdot \nabla w^h \, \mathrm{d}v - 2 \int_{\Gamma_d} w^h \left(\nabla w^h \cdot \mathbf{n}\right) \, \mathrm{d}a + \alpha \int_{\Gamma_d} (w^h)^2 \, \mathrm{d}a \tag{A.2}$$

Applying definitions (A.1), the above equation can be written as,

$$a\left(w^h, w^h\right) = \| \nabla w^h \|^2 - 2 \int_{\Gamma_d} w^h \left(\nabla w^h \cdot \mathbf{n}\right) \, \mathrm{d}a + \alpha \| w^h \|^2_{\Gamma_d} \tag{A.3}$$

Employing Young's inequality with ϵ in (A.3), we get

$$a\left(w^h, w^h\right) \geqslant \| \nabla w^h \|^2 - \frac{1}{\epsilon} \| w^h \|^2_{\Gamma_d} - \epsilon \| \left(\nabla w^h \cdot \mathbf{n}\right) \|^2_{\Gamma_d} + \alpha \| w^h \|^2_{\Gamma_d} \tag{A.4}$$

where $\epsilon > 0$.

Assuming a mesh dependent constant C such that

$$\| \left(\nabla w^h \cdot \mathbf{n}\right) \|^2_{\Gamma_d} \leqslant C \| \nabla w^h \|^2 \tag{A.5}$$

the bilinear form can be rewritten as

$$a\left(w^h, w^h\right) \geqslant (1 - \epsilon C) \| \nabla w^h \|^2 + \left(\alpha - \frac{1}{\epsilon}\right) \| w^h \|^2_{\Gamma_d} \tag{A.6}$$

Taking $\epsilon = 1/\alpha$, coercivity of the bilinear form is ensured when $\alpha > C$. In the present study, a value of $\alpha = 2C$ is used.

A.2 Fourth-order problem

Using $w^h \in \mathcal{V}^h$ in place of u^h, the discrete version of the Nitsche's bilinear form (5.11a) can be written as,

$$\begin{aligned} a\left(w^h, w^h\right) = &\int_{\Omega} \left(\Delta w^h\right)^2 \, \mathrm{d}v + 2 \int_{\Gamma_d} w^h \left(\nabla \left(\Delta w^h\right) \cdot \mathbf{n}\right) \, \mathrm{d}a + \alpha_1 \int_{\Gamma_d} \left(w^h\right)^2 \, \mathrm{d}a \\ &- 2 \int_{\Gamma_d} \left(\nabla w^h \cdot \mathbf{n}\right) \Delta w^h \, \mathrm{d}a + \alpha_2 \int_{\Gamma_d} \left(\nabla w^h \cdot \mathbf{n}\right)^2 \, \mathrm{d}a \end{aligned} \tag{A.7}$$

Applying the L_2 norms defined in (A.1), equation (A.7) can be written as,

$$a\left(w^h, w^h\right) = \| \Delta w^h \|^2 + 2 \int_{\Gamma_d} w^h \left(\nabla \left(\Delta w^h\right) \cdot \mathbf{n}\right) \, \mathrm{d}a + \alpha_1 \| w^h \|^2_{\Gamma_d}$$

$$- 2 \int_{\Gamma_d} \left(\nabla w^h \cdot \mathbf{n}\right) \Delta w^h \, \mathrm{d}\Gamma + \alpha_2 \| \nabla w^h \cdot \mathbf{n} \|^2_{\Gamma_d} \tag{A.8}$$

Employing the Young's inequality with ϵ in (A.8), we obtain

$$a\left(w^h, w^h\right) \geqslant \| \Delta w^h \|^2 - \frac{1}{\epsilon_1} \| w^h \|^2_{\Gamma_d} - \epsilon_1 \| \left(\nabla \left(\Delta w^h\right) \cdot \mathbf{n}\right) \|^2_{\Gamma_d} + \alpha_1 \| w^h \|^2_{\Gamma_d}$$

$$- \frac{1}{\epsilon_2} \| \nabla w^h \cdot \mathbf{n} \|^2_{\Gamma_d} - \epsilon_2 \| \Delta w^h \|^2_{\Gamma_d} + \alpha_2 \| \nabla w^h \cdot \mathbf{n} \|^2_{\Gamma_d} \tag{A.9}$$

where $\epsilon_1 > 0$ and $\epsilon_2 > 0$. Assuming mesh dependent constants C_1 and C_2 such that

$$\| \left(\nabla \left(\Delta w^h\right) \cdot \mathbf{n}\right) \|^2_{\Gamma_d} \leqslant C_1 \| \Delta w^h \|^2 \tag{A.10a}$$

$$\| \Delta w^h \|^2_{\Gamma_d} \leqslant C_2 \| \Delta w^h \|^2 \tag{A.10b}$$

the bilinear form can be rewritten as

$$a\left(w^h, w^h\right) \geqslant \left(1 - \epsilon_1 C_1 - \epsilon_2 C_2\right) \| \Delta w^h \|^2$$

$$+ \left(\alpha_1 - \frac{1}{\epsilon_1}\right) \| w^h \|^2_{\Gamma_d} + \left(\alpha_2 - \frac{1}{\epsilon_2}\right) \| \nabla w^h \cdot \mathbf{n} \|^2_{\Gamma_d} \tag{A.11}$$

Taking $\epsilon_1 = 1/\alpha_1$ and $\epsilon_2 = 1/\alpha_2$, coercivity of $a\left(w^h, w^h\right)$ is ensured when the following condition is satisfied:

$$1 > \frac{C_1}{\alpha_1} + \frac{C_2}{\alpha_2} \tag{A.12}$$

A convenient choice for the stability parameters would be $\alpha_1 > 2C_1$ and $\alpha_2 > 2C_2$.

A.3 Stability parameter evaluation

The mesh dependent constant C in equation (A.5) and constants C_1 and C_2 in equations (A.10) can be determined by solving a generalized eigenvalue problem at the Dirichlet boundary. The eigenvalue problem can be posed as:

$$\mathbf{A}\mathbf{x} = \Lambda\mathbf{B}\mathbf{x} \tag{A.13}$$

where the elements of $\mathbf{A}$ and $\mathbf{B}$ follow directly from equations (A.5) and (A.10) as listed in the following subsections.

A.3.1 Poisson equation

Elements of the matrices $\mathbf{A}$ and $\mathbf{B}$ are given by

$$[\mathbf{A}]_{ij} = \int_{\Gamma_d} (\nabla N_i \cdot \mathbf{n}) (\nabla N_j \cdot \mathbf{n}) \, \mathrm{d}a \tag{A.14a}$$

$$[\mathbf{B}]_{ij} = \int_{\Omega} \nabla N_i \cdot \nabla N_j \, \mathrm{d}v \tag{A.14b}$$

The maximum eigenvalue obtained from a given discretization provides a good estimate for the parameter C. The stability parameter is then calculated as $\alpha = 2\max(\Lambda)$.

A.3.2 Biharmonic equation

For the fourth order problem, the inequalities (A.10) give rise to two separate eigenvalue problems.

For the parameter α_1

$$[\mathbf{A}]_{ij} = \int_{\Gamma_d} (\nabla (\Delta N_i) \cdot \mathbf{n}) \, (\nabla (\Delta N_j) \cdot \mathbf{n}) \, \mathrm{d}a \tag{A.15a}$$

$$[\mathbf{B}]_{ij} = \int_{\Omega} \Delta N_i \, \Delta N_j \, \mathrm{d}v \tag{A.15b}$$

For the parameter α_2

$$[\mathbf{A}]_{ij} = \int_{\Gamma_d} \Delta N_i \; \Delta N_j \, \mathrm{d}a \tag{A.16a}$$

$$[\mathbf{B}]_{ij} = \int_{\Omega} \Delta N_i \; \Delta N_j \, \mathrm{d}v \tag{A.16b}$$

Stability parameters are then estimated as, $\alpha_1 > 2 \max(\Lambda_1)$ and $\alpha_2 > 2 \max(\Lambda_2)$.

A.3.3 Global and local approaches to the eigenvalue problem

Stabilization parameters are chosen so as to ensure coercivity of the bilinear form. The evaluation can be performed globally, as proposed in Griebel and Schweitzer (2003). For a given discretization, the matrices $\mathbf{A}$ and $\mathbf{B}$ in the eigenvalue problem (A.13) are constructed once. Only those basis functions whose support intersects the Dirichlet boundary are considered in forming the matrices. The eigenvalue problem then yields stabilization parameters which remain constant along the entire Dirichlet boundary.

A more recent approach (Dolbow and Harari, 2009) is to determine the stabilization parameters locally. A series of much smaller eigenvalue problems are set up and solved during the assembly process. This gives rise to stabilization terms that are piecewise-constant along the boundary elements. It is worth noting here that since the eigenvalue problems are solved only at the Dirichlet boundary, both of the above approaches yield higher estimates of the constants in equations (A.5) and (A.10), than what would be strictly required to enforce the inequalities.

The present work uses the local approach for its efficiency and simplicity in implementation. However, slight modifications are employed in the process. These modifications cast the eigenvalue problem such that the estimates of the stabilization parameters are relaxed, avoiding acute increases in the magnitude of stabilization parameters for certain grid/boundary orientations. This numerical issue can occur

for problems with non-conforming grids when the physical domain intersects only a small fraction of the boundary element. In essence, the modifications aim at relaxing the magnitude of stability parameters to prevent ill-conditioning of the global stiffness matrix while maintaining the parameters large enough to ensure coercivity of the bilinear form. A brief description of the approach is given below. In order

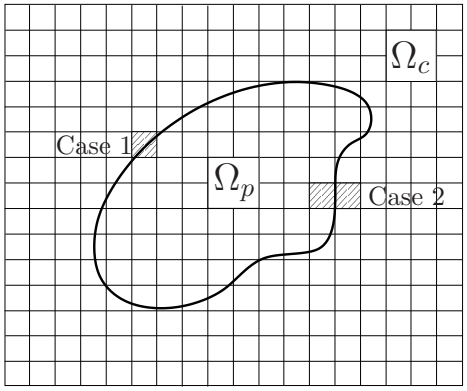

FIGURE A.1: Elements considered to form the local eigenvalue problems for different intersection scenarios of the Dirichlet boundary.

to set up the eigenvalue problem for each boundary element, the matrices $\mathbf{A}$ and $\mathbf{B}$ are evaluated and assembled over all elements that intersect the Dirichlet boundary. An illustration of this concept is shown in Figure A.1 for two intersection scenarios. For the case of a boundary element, where the Dirichlet boundary is embedded within (case 1), the matrices are evaluated over only that element. However, in the degenerate case when the edge of an element is part of the Dirichlet boundary (case 2), the matrices are assembled for both the interior and exterior elements that share the edge. Furthermore, the domain integral representing elements of matrix $\mathbf{B}$ is evaluated over an entire element irrespective of the location of the physical domain. It is to be noted here that these modifications can result in evaluation of integrals over elements that are not in the physical domain, where the spline basis need not be complete. However, we find it convenient to construct the spline functions so that a complete basis is obtained for at least one layer of exterior elements adjoining the

Dirichlet boundary.

Bibliography

Adalsteinsson, D. and Sethian, J. (2003), "Transport and diffusion of material quantities on propagating interfaces via level set methods," *Journal of Computational Physics*, 185, 271 – 288.

Akira, O. (1989), "Ginzburg–Landau Approach to Elastic Effects in the Phase Separation of Solids," 58, 3065–3068.

Bartkowiak, L. and Pawlow, I. (2005), "The Cahn–Hilliard–Gurtin system coupled with elasticity," 34, 1005–1043.

Baumgart, T., Hess, S. T., and Webb, W. W. (2003), "Imaging coexisting fluid domains in biomembrane models coupling curvature and line tension," *Nature*, 425, 821–824.

Baumgart, T., Das, S., Webb, W., and Jenkins, J. (2005), "Membrane Elasticity in Giant Vesicles with Fluid Phase Coexistence," *Biophysical Journal*, 89, 1067–1080.

Bazilevs, Y., Beirao da Veiga, L., Cottrell, J., Hughes, T., and Sangalli, G. (2006), "Isogeometric analysis: approximation, stability and error estimates for h-refined meshes," *Mathematical Models and Methods in Applied Sciences*, 16, 1031–1090.

Bertalmio, M., Cheng, L.-T., Osher, S., and Sapiro, G. (2001), "Variational Problems and Partial Differential Equations on Implicit Surfaces," *Journal of Computational Physics*, 174, 759 – 780.

Biben, T. and Misbah, C. (2003), "Tumbling of vesicles under shear flow within an advected-field approach," *Phys. Rev. E*, 67, 031908.

Biben, T., Kassner, K., and Misbah, C. (2005), "Phase-field approach to three-dimensional vesicle dynamics," *Phys. Rev. E*, 72, 041921.

Bloch, K. E. (1983), "Sterol, Structure and Membrane Functio," *Critical reviews in biochemistry and molecular biology*, 14, 47–92.

Bochev, P. B., Gunzburger, M. D., and Shadid, J. N. (2004), "Stability of the SUPG finite element method for transient advection-diffusion problems," *Computer methods in applied mechanics and engineering*, 193, 2301–2323.

Braess, D. (2007), *Finite Elements: Theory, Fast Solvers, and Applications in Solid Mechanics*, Cambridge University Press, 3 edn.

Brooks, A. N. and Hughes, T. J. (1982), "Streamline upwind/Petrov-Galerkin formulations for convection dominated flows with particular emphasis on the incompressible Navier-Stokes equations," *Computer Methods in Applied Mechanics and Engineering*, 32, 199 – 259.

Brown, D. and London, E. (1998), "Functions of lipid rafts in biological membranes," *Annual review of cell and developmental biology*, 14, 111–136.

Cahn, J. W. and Hilliard, J. E. (1958), "Free Energy of a Nonuniform System. I. Interfacial Free Energy," *The Journal of Chemical Physics*, 28, 258–267.

Campelo, F. and Hernández-Machado, A. (2006), "Dynamic model and stationary shapes of fluid vesicles," *The European Physical Journal E: Soft Matter and Biological Physics*, 20, 37–45.

Canham, P. B. (1970), "The minimum energy of bending as a possible explanation of the biconcave shape of the human red blood cell," *Journal of Theoretical Biology*, 26, 61–81.

Carbonetto, P. (2009)`http://www.cs.ubc.ca/~pcarbo/`.

Davis, T. A. (2004a), "Algorithm 832: UMFPACK V4.3—an unsymmetric-pattern multifrontal method," *ACM Trans. Math. Softw.*, 30, 196–199.

Davis, T. A. (2004b), "A column pre-ordering strategy for the unsymmetric-pattern multifrontal method," *ACM Trans. Math. Softw.*, 30, 165–195.

Davis, T. A. and Duff, I. S. (1997), "An Unsymmetric-Pattern Multifrontal Method for Sparse LU Factorization," *SIAM Journal on Matrix Analysis and Applications*, 18, 140–158.

Davis, T. A. and Duff, I. S. (1999), "A combined unifrontal/multifrontal method for unsymmetric sparse matrices," *ACM Trans. Math. Softw.*, 25, 1–20.

de la Serna, J. B. (2007)`http://www.microscopyu.com/staticgallery/smallworld/2007/circleexlarge11.html`.

Deamer, D. and Hazen, R. (2006)`https://nai.arc.nasa.gov/nai/library-of-resources/annual-reports/2006/ciw/projects/project-4-prebiotic-molecular-selection-and-organization/`.

Deseri, L., Piccioni, M. D., and Zurlo, G. (2008), "Derivation of a new free energy for biological membranes," *Continuum Mechanics and Thermodynamics*, 20, 255–273.

Döbereiner, H.-G., Selchow, O., and Lipowsky, R. (1999), "Spontaneous curvature of fluid vesicles induced by trans-bilayer sugar asymmetry," *European Biophysics Journal*, 28, 174–178.

Dolbow, J. and Harari, I. (2009), "An efficient finite element method for embedded interface problems," *International journal for numerical methods in engineering*, 78, 229–252.

Elliott, C. M. and French, D. A. (1987), "Numerical Studies of the Cahn–Hilliard equation for phase separation," *IMA J Appl Math*, 38, 97–128.

Elson, E. L., Fried, E., Dolbow, J. E., and Genin, G. M. (2010), "Phase Separation in Biological Membranes: Integration of Theory and Experiment," *Annu. Rev. Biophys*, 39, 207–226.

Embar, A., Dolbow, J., and Harari, I. (2010), "Imposing Dirichlet boundary conditions with Nitsche's method and spline-based finite elements," *International journal for numerical methods in engineering*, 83, 877–898.

Embar, A., Dolbow, J., and Fried, E. (2012), "Microdomain evolution on giant unilamellar vesicles," *Biomechanics and Modeling in Mechanobiology*, pp. 1–19.

Engel, G., Garikipati, K., Hughes, T., Larson, M., Mazzei, L., and Taylor, R. (2002), "Continuous/discontinuous finite element approximations of fourth-order elliptic problems in structural and continuum mechanics with applications to thin beams and plates, and strain gradient elasticity," *Computer Methods in Applied Mechanics and Engineering*, 191, 3669–3750.

Evans, E. (1974), "Bending Resistance and Chemically Induced Moments in Membrane Bilayers," *Biophysical Journal*, 14, 923–931.

Evans, E. and Skalak, R. (1980), *Mechanics and thermodynamics of biomembranes*, CRC Press.

Eyre, D. J. (1997), "An unconditionally stable one-step scheme for gradient systems," *Unpublished article*.

Fan, J., Han, T., and Haataja, M. (2010), "Hydrodynamic effects on spinodal decomposition kinetics in planar lipid bilayer membranes," *The Journal of chemical physics*, 133, 235101.

Fernández-Méndez, S. and Huerta, A. (2004), "Imposing essential boundary conditions in mesh-free methods," *Computer Methods in Applied Mechanics and Engineering*, 193, 1257–1275.

Flory, P. J. (1942), "Thermodynamics of High Polymer Solutions," *The Journal of Chemical Physics*, 10, 51–61.

Franca, L. P. and Frey, S. L. (1992), "Stabilized finite element methods: II. The incompressible Navier-Stokes equations," *Computer Methods in Applied Mechanics and Engineering*, 99, 209–233.

Fried, E. (2006), "On the Relationship between Supplemental Balances in Two Theories for Pure Interface Motion," *SIAM Journal on Applied Mathematics*, 66, 1130–1149.

Fried, E. and Gurtin, M. E. (1996), "A phase-field theory for solidification based on a general anisotropic sharp-interface theory with interfacial energy and entropy," *Physica D: Nonlinear Phenomena*, 91, 143 – 181.

Gallant, T. (2003)`http://kvhs.nbed.nb.ca/gallant/biology/Plasma_Membrane.jpg`.

García-Sáez, A. J., Chiantia, S., and Schwille, P. (2007), "Effect of line tension on the lateral organization of lipid membranes," *Journal of Biological Chemistry*, 282, 33537–33544.

Garcke, H. (2003), "On Cahn–Hilliard systems with elasticity," 133, 307–331.

Gary S. Ayton, J. Liam McWhirter, P. M. and Voth, G. A. (2005), "Coupling Field Theory with Continuum Mechanics: A Simulation of Domain Formation in Giant Unilamellar Vesicles," *Biophysical Journa*, 88, 3855–3869.

Gomez, H. and Hughes, T. J. (2011), "Provably unconditionally stable, second-order time-accurate, mixed variational methods for phase-field models," *Journal of Computational Physics*, 230, 5310–5327.

Gómez, H., Calo, V. M., Bazilevs, Y., and Hughes, T. J. (2008), "Isogeometric analysis of the Cahn-Hilliard phase-field model," *Computer Methods in Applied Mechanics and Engineering*, 197, 4333 – 4352.

Gonzalez Cinca, R., Folch, R., Benitez, R., Ramirez-Piscina, L., Casademunt, J., and Hernandez-Machado, A. (2003), "Phase-field models in interfacial pattern formation out of equilibrium," *ArXiv Condensed Matter e-prints*.

Greer, J. (2006), "An Improvement of a Recent Eulerian Method for Solving PDEs on General Geometries," *Journal of Scientific Computing*, 29, 321–352, 10.1007/s10915-005-9012-5.

Greer, J. B., Bertozzi, A. L., and Sapiro, G. (2006), "Fourth order partial differential equations on general geometries," *Journal of Computational Physics*, 216, 216 – 246.

Griebel, M. and Schweitzer, M. A. (2003), "A particle-partition of unity method part V: boundary conditions," in *Geometric Analysis and Nonlinear Partial Differential Equations*, pp. 519–542, Springer.

Hac, A. E., Seeger, H. M., Fidorra, M., and Heimburg, T. (2005), "Diffusion in two-component lipid membranes - a fluorescence correlation spectroscopy and Monte Carlo simulation study," *Biophysical journal*, 88, 317–333.

Hansbo, A. and Hansbo, P. (2002), "An unfitted finite element method, based on Nitsche's method, for elliptic interface problems," *Computer methods in applied mechanics and engineering*, 191, 5537–5552.

Helfrich, W. (1973), "Elastic properties of lipid bilayers: theory and possible experiments," *Z Naturforsch C*, 28, 693–703.

Henderson, A. (2007), *A Parallel Visualization Application*, Kitware Inc.

Hess, S. T., Kumar, M., Verma, A., Farrington, J., Kenworthy, A., and Zimmerberg, J. (2005), "Quantitative electron microscopy and fluorescence spectroscopy of the membrane distribution of influenza hemagglutinin," *The Journal of Cell Biology*, 169, 965–976.

Höllig, K. (2012), *Finite element methods with B-splines*, vol. 26, Society for Industrial and Applied Mathematics.

Huggins, M. L. (1942), "Theory of Solutions of High Polymers1," *Journal of the American Chemical Society*, 64, 1712–1719.

Hughes, T. J., Franca, L. P., and Hulbert, G. M. (1989), "A new finite element formulation for computational fluid dynamics: VIII. The Galerkin/least-squares method for advective-diffusive equations," *Computer Methods in Applied Mechanics and Engineering*, 73, 173–189.

Hughes, T. J., Cottrell, J. A., and Bazilevs, Y. (2005), "Isogeometric analysis: CAD, finite elements, NURBS, exact geometry and mesh refinement," *Computer methods in applied mechanics and engineering*, 194, 4135–4195.

Ivanyik (2007)`http://stonechurchclinic.ca/Rh-prevention-program/rbc/view`.

Jamet, D. and Misbah, C. (2007), "Towards a thermodynamically consistent picture of the phase-field model of vesicles: Local membrane incompressibility," *Phys. Rev. E*, 76, 051907(1–7).

Jenkins, J. T. (1977), "The equations of mechanical equilibrium of a model membrane," *SIAM Journal on Applied Mathematics*, 32, 755–764.

Jülicher, F. and Lipowsky, R. (1996), "Shape transformations of vesicles with intramembrane domains," *Physical Review E*, 53, 2670.

Kahya, N., Scherfeld, D., Bacia, K., Poolman, B., and Schwille, P. (2003), "Probing lipid mobility of raft-exhibiting model membranes by fluorescence correlation spectroscopy," *Journal of Biological Chemistry*, 278, 28109–28115.

Kim, I. (2006), "An algorithm for finding the distance between two ellipses," *Communications-Korean Mathematical Society*, 21, 559.

Komura, S., Shirotori, H., Olmsted, P., and Andelman, D. (2004), "Lateral phase separation in mixtures of lipids and cholesterol," *Europhysics Letters*, 67, 321–327.

Kuzmin, P. I., Akimov, S. A., Chizmadzhev, Y. A., Zimmerberg, J., and Cohen, F. S. (2005), "Line tension and interaction energies of membrane rafts calculated from lipid splay and tilt," *Biophysical journal*, 88, 1120–1133.

Lawrence, J. C., Saslowsky, D. E., Michael Edwardson, J., and Henderson, R. M. (2003), "Real-time analysis of the effects of cholesterol on lipid raft behavior using atomic force microscopy," *Biophysical journal*, 84, 1827–1832.

Lowengrub, J. S., Rätz, A., and Voigt, A. (2009), "Phase-field modeling of the dynamics of multicomponent vesicles: Spinodal decomposition, coarsening, budding, and fission," *Phys. Rev. E*, 79, 031926.

Marrink, S. J., Risselada, J., and Mark, A. E. (2005), "Simulation of gel phase formation and melting in lipid bilayers using a coarse grained model," *Chemistry and physics of lipids*, 135, 223–244.

McMahon, H. T. and Gallop, J. L. (2005), "Membrane curvature and mechanisms of dynamic cell membrane remodelling," *Nature*, 438, 590–596.

Murray, J. (2002), *Mathematical Biology*, no. v. 2 in Interdisciplinary applied mathematics, Springer.

Niemelä, P. S., Ollila, S., Hyvönen, M. T., Karttunen, M., and Vattulainen, I. (2007), "Assessing the nature of lipid raft membranes," *PLoS computational biology*, 3, e34.

Nitsche, J. (1971), "Über ein Variationsprinzip zur Lösung von Dirichlet-Problemen bei Verwendung von Teilräumen, die keinen Randbedingungen unterworfen sind," *Abhandlungen aus dem Mathematischen Seminar der Universität Hamburg*, 36, 9–15.

O' Neill, B. (2006), *Elementary Differential Geometry*, Academic Press, 2 edn.

Oldenhuis, R. (2010)https://www.mathworks.com/matlabcentral/fileexchange/26324-distance-between-points-and-ellipse.

Ono, A. and Freed, E. O. (2001), "Plasma membrane rafts play a critical role in HIV-1 assembly and release," *Proceedings of the National Academy of Sciences of the United States of America*, 98, 13925–13930.

Piegl, L. and Tiller, W. (1997), *The NURBS Book*, Springer, 2 edn.

Pike, L. J. (2006), "Rafts defined: a report on the Keystone symposium on lipid rafts and cell function," *J. Lipid Res.*, 47, 1597–1598.

Powers, T. R., Huber, G., and Goldstein, R. E. (2002), "Fluid-membrane tethers: minimal surfaces and elastic boundary layers," *Physical Review E*, 65, 041901.

Sackmann, E. (1995), "Chapter 5: Physical basis of self-organization and function of membranes: Physics of vesicles," in *Structure and Dynamics of Membranes - From Cells to Vesicles*, eds. R. Lipowsky and E. Sackmann, vol. 1, Part 1 of *Handbook of Biological Physics*, pp. 213 – 304, North-Holland.

Saeki, D., Hamada, T., and Yoshikawa, K. (2005), "Domain Growth Kinetics in a Cell-sized Liposome," *arXiv preprint cond-mat/0510171*.

Sagui, C., Somoza, A. M., and Desai, R. C. (1994), "Spinodal decomposition in an order-disorder phase transition with elastic fields," *PhyRevE*, 50, 4865–4879.

Schenk, O., Wächter, A., and Hagemann, M. (2007), "Matching-based Preprocessing Algorithms to the Solution of Saddle-Point Problems in Large-Scale Nonconvex Interior-Point Optimization," *Comput. Optim. Appl.*, 36, 321–341.

Schenk, O., Bollhöfer, M., and Römer, R. A. (2008), "On Large Scale Diagonalization Techniques For The Anderson Model Of Localization," *SIAM Review*, 50, 91–112, SIGEST Paper.

Schillinger, D. and Rank, E. (2011), "An unfitted¡ i¿ hp¡/i¿-adaptive finite element method based on hierarchical B-splines for interface problems of complex geometry," *Computer Methods in Applied Mechanics and Engineering*, 200, 3358–3380.

Seifert, U. (1997), "Configurations of fluid membranes and vesicles," *Advances in Physics*, 46, 13–137.

Seifert, U., Berndl, K., and Lipowsky, R. (1991), "Shape transformations of vesicles: Phase diagram for spontaneous-curvature and bilayer-coupling models," *Phys. Rev. A*, 44, 1182–1202.

Shi, Q. and Voth, G. A. (2005), "Multi-scale modeling of phase separation in mixed lipid bilayers," *Biophysical journal*, 89, 2385–2394.

Simons, K. and Ikonen, E. (1997), "Functional rafts in cell membranes," *Nature*, 387, 569–572.

Smereka, P. (2006), "The numerical approximation of a delta function with application to level set methods," *Journal of Computational Physics*, 211, 77 – 90.

Suo, Z. and Lu, W. (2000), "Composition modulation and nanophase separation in a binary epilayer," 48, 211–232.

Takeda, M., Leser, G. P., Russell, C. J., and Lamb, R. A. (2003), "Influenza virus hemagglutinin concentrates in lipid raft microdomains for efficient viral fusion," *Proceedings of the National Academy of Sciences of the United States of America*, 100, 14610–14617.

Tian, A., Johnson, C., Wang, W., and Baumgart, T. (2007), "Line tension at fluid membrane domain boundaries measured by micropipette aspiration," *Physical review letters*, 98, 208102.

Timoshenko, S., Woinowsky-Krieger, S., and Woinowsky, S. (1959), *Theory of plates and shells*, vol. 2, McGraw-hill New York.

Tsafrir, I., Caspi, Y., Guedeau-Boudeville, M.-A., Arzi, T., and Stavans, J. (2003), "Budding and Tubulation in Highly Oblate Vesicles by Anchored Amphiphilic Molecules," *Phys. Rev. Lett.*, 91, 138102.

Veatch, S., Polozov, I., Gawrisch, K., and Keller, S. (2004), "Liquid domains in vesicles investigated by NMR and fluorescence microscopy," *Biophysical journal*, 86, 2910–2922.

Veatch, S. L. and Keller, S. L. (2003), "Separation of liquid phases in giant vesicles of ternary mixtures of phospholipids and cholesterol," *Biophysical journal*, 85, 3074–3083.

Veatch, S. L. and Keller, S. L. (2005), "Seeing spots: complex phase behavior in simple membranes," *Biochimica et Biophysica Acta (BBA)-Molecular Cell Research*, 1746, 172–185.

Vollmayr-Lee, B. P. and Rutenberg, A. D. (2003), "Fast and accurate coarsening simulation with an unconditionally stable time step," *Physical Review E*, 68, 066703.

Wang, X. and Du, Q. (2008), "Modelling and simulations of multi-component lipid membranes and open membranes via diffuse interface approaches," *Journal of Mathematical Biology*, 56, 347–371.

Wissmann, P. (2006)`http://homepage.smc.edu/wissmann_paul/anatomy2textbook/phospholipids.html`.

Yanagisawa, M., Imai, M., Masui, T., Komura, S., and Ohta, T. (2007), "Growth Dynamics of Domains in Ternary Fluid Vesicles," *Biophysical Journal*, 92, 115 – 125.

Yanagisawa, M., Imai, M., and Taniguchi, T. (2008), "Shape Deformation of Ternary Vesicles Coupled with Phase Separation," *Phys. Rev. Lett.*, 100, 148102.

Yeon, D.-H., Cha, P.-R., Kim, J.-H., Grant, M., and Yoon, J.-K. (2005), "A phase field model for phase transformation in an elastically stressed binary alloy," *MSMSE*, 13, 299–319.

Zhang, Z., Bhide, S. Y., and Berkowitz, M. L. (2007), "Molecular dynamics simulations of bilayers containing mixtures of sphingomyelin with cholesterol and phosphatidylcholine with cholesterol," *The Journal of Physical Chemistry B*, 111, 12888–12897.

Biography

Anand Srinivasan Embar was born in the garden city of Bangalore in India on February 28th 1974. He received his Bachelors from the Civil Engineering Department at the University Visvesvaraya College of Engineering, Bangalore, Masters in Structural Engineering from the Indian Institute of Technology, Mumbai, and a Doctor of Philosophy in Civil and Environmental Engineering from Duke University.

Anand has co-authored several peer-reviewed journal articles, including "Imposing Dirichlet boundary conditions with Nitsche's method and spline-based finite elements", (Embar et al., 2010) and "Microdomain evolution on giant unilamellar vesicles", (Embar et al., 2012). Anand will be starting a position in the Structural Mechanics development division of Abaqus, currently part of Dassault Systemes Simulia Corp, in June 2013.